Investigation of bulk and surface properties of Si and Si-Ge systems using Monte Carlo simulations and classical potentials

by

Francesca M. Tavazza

(Under the direction of David P. Landau)

Abstract

In this dissertation the study of Si and Si-Ge systems is conducted to provide answers to both statistical mechanics and material science questions. The compressible Ising model provides a general framework for describing phase transitions in alloys where the ordering is accompanied by a displacive structural change. Its behavior in the case of ferromagnetic interactions and constant volume conditions is investigated here using a model of binary alloys driven by elastic interactions. Classical Monte Carlo simulations in the semi-grand-canonical ensemble are utilized, and the two species composing the alloy are modeled by Si and Ge interacting via the Stillinger-Weber potential. A volume much closer to pure Ge than to pure Si is chosen to introduce a significant difference between the two species. The phase diagram contains a closed first order line which divides a "phase-segregated" ("ordered") phase from a disordered one. In the "ordered" phase the most unfavorable species (Si in this case) congregates forming planes in-between which the other species is located. When interested in the study of technological important materials, few, if any, are more relevant than Si and Ge. In this work a classical, hybrid MC-MD algorithm is introduced for the study of surface phenomena (2D island stability or step-edge evolution) on (001) Si or Ge surfaces. This method is very general and can be easily expanded to other semiconductors and different surfaces. With respect to previously developed algorithms, this presents the advantage of working off-lattice and utilizing bulk-fitted potentials. It is based on the introduction of collective moves, such as dimer jumps, into the MC algorithm. MD-driven local relaxations are considered as trial moves for the MC. Results on early stages of island formation, island stability versus temperature and system size, and step-edge evolution are obtained in good qualitative agreement with experimental results.

Index words: Si, Ge, Monte Carlo, surface, Compressible Ising Model

Investigation of bulk and surface properties of Si and Si-Ge systems using Monte Carlo simulations and classical potentials

by

Francesca M. Tavazza

B.A., Università Statale degli Studi di Milano, 1993

M.D., Università Statale degli Studi di Milano, 1995

A Dissertation Submitted to the Graduate Faculty

of The University of Georgia in Partial Fulfillment

of the

Requirements for the Degree

Doctor of Philosophy

Athens, Georgia

2003

Investigation of bulk and surface properties of Si and Si-Ge systems using Monte Carlo simulations and classical potentials

by

Francesca M. Tavazza

Approved:

Major Professor: David P. Landau

Committee: Michael Geller
Uwe Happek
Steven P. Lewis
H.-Bernd Schüttler

Electronic Version Approved:

Maureen Grasso
Dean of the Graduate School
The University of Georgia
August 2003

"Considerate la vostra semenza:

nati non foste a viver come bruti,

ma per seguir virtute e conoscenza."

(Dante Alighieri, Inferno, Canto XXIV, 118)

"Consider ye the seed from which ye sprang:

ye were not made to live like brutes,

but for the pursuit of excellence and knowledge."

(Dante Alighieri, Inferno, Canto XXIV, 118)

Acknowledgments

My chief acknowledgment is to my advisor, Professor D.P. Landau, for his guidance, encouragement and insight during this research work. He taught me how important thoroughness is in research and how exciting this work can be. I would like to express special appreciation for his support and understanding during trying moments in my personal life.

I would like to thank all the members of my committee, Professors M. Geller, U. Happek, S.P. Lewis and Prof. H-B. Schüttler for their help along these years and their careful reading of this dissertation. A special thank to Mike Caplinger and Jeff Deroshia for being always so patient and willing to help.

I also wish to thank Dr. S. Tsai, Dr. B. Dünweg, Prof. K. Binder and Prof. A. Milchev for many stimulating suggestions and fruitful discussions. I would like to mention my visit to Dr. J. Adler at Technion, Haifa, as one of the most interesting and profitable moments of my Ph.D., and deeply thank her for such an opportunity. I'm also strongly indebted to Dr. J. Adler for the graphic package AViz developed by the Computational Physic Group at Technion, Israel, that enabled much of my data analysis.

A special thank to Laura Nurminen: working together has been not only very productive but also real fun!

I would like to thank CSC, Finland and NPACI for providing some of the computing time much needed in this research.

I also would like to thank faculty, staff members and my fellow graduate students in the department of Physics and Astronomy for their kindness and friendship.

It goes without saying that I owe a great deal to the interest and encouragement my family has shown at every stage of this work, in particular my brother Angelo who, from afar, always cared for me, my research and my personal life. Finally I would like to acknowledge, though in a very inadequate manner, the constant help and support furnished by my husband, Jay, without whose aid this dissertation probably never would have been written.

Table of Contents

Chapter 1

Introduction

Elastic interactions play a fundamental role in describing a wide variety of physical phenomena, as, for example, the evolution of semiconductor surfaces. They are also the key factor in determining the behavior of the compressible Ising model, an important part of Statistical Mechanics. In this dissertation we address both problems, the former in the particular case of the (001) surface of Si or Ge, the latter focused on the bulk under constant-volume conditions. We decided to investigate two phenomena that are significantly different in order to analyze a broader range of effects related to elastic interactions. A computational approach is followed in both investigations, and, more specifically, Monte Carlo (MC) simulations are utilized.

The compressible Ising model provides a general framework for describing phase transitions driven by elastic interactions and ordering effects related to lattice distortions. It is a long standing problem in Statistical Mechanics: because of its fundamental interest it has been addressed for several decades but up to now only incomplete or partial solutions have been found. In this model two sets of variables are considered: the spins $s_i = \pm 1$ and the displacements $\underline{u}_i$ which define the motion of the spins from their original lattice sites. The interactions among spins are elastic and generally well described by classical potentials. A simple linear transformation relates the "Ising representation" (each spin is either up or down) to the "binary alloy picture" (each atom is either of species A or B), and in this dissertation a Si-Ge alloy with variable composition ($Si_{1-x}Ge_x$) is used to perform the investigation. Ferromagnetic interactions and constant volume conditions are considered, because no

complete results are available in the literature for this case. On the contrary, several studies have been performed for ferromagnetic interactions under constant pressure conditions, so that comparisons will be made between the two cases. In our study the interatomic interactions are modeled via Stillinger-Weber potential [1], and a volume closer to that of pure Ge than to pure Si is chosen to induce different structural rearrangements for the two species. Because of the size difference between Si and Ge, this choice corresponds to the introduction of compressive or tensile stress on the system as the composition varies.

As far as technological important materials are concerned, few, if any, are more relevant that Si and Ge. The (001) surface of silicon, in particular, has a wide range of applications in the micro- and optoelectronic industries. Moreover, it also provides an ideal model for the study of semiconductor epitaxy as well as of a variety of surface structural modifications like reconstruction, island stabilization and step edge modification. Because of its relevance, a substantial amount of work has been done on this surface, yet several questions are still open. Among these is the determination of equilibrium shapes and thermal stability of 2D islands, or a precise description of substrate modification in the presence of a Ge or Si adsorbate. The scarcity of definitive answers to these queries is related to the difficulty of carrying out thorough theoretical investigations. Experimental results have shown that stable islands are constituted of at least several hundred atoms and that surface processes occur on a time scale of the order of seconds, so that large-scale long-time simulations are needed to correctly reproduce the physics of the system.

In this dissertation we develop a classical, hybrid Monte Carlo-Molecular Dynamics (MC-MD) algorithm to answer these problems. The particular version presented here is targeted to the study of the Si(001) surface with Si or Ge adatoms, but the idea behind it is rather general and can be easily expanded to the study of other semiconductor surfaces. The idea at the basis of this algorithm

is to add the possibility of collective moves to the standard MC single-atom moves. With MC the evolution of the system is definitely faster than it would be using standard Molecular Dynamics (MD); moreover, because of the collective moves, it is possible to overcome high potential barriers that otherwise would trap the system in metastable states. The identification of the collective moves to implement is the only point where knowledge of the particular physical system under consideration is necessary. As an example, in the case of the Si(001) surface, the existence of a (2×1) reconstruction, where adjacent atoms dimerize, leads us to introduce the possibility of moving each dimer as a whole.

This dissertation is organized as follow. Chapters 2 and 3 contain reviews of experimental (when available) and theoretical results on the Si(001) surface and the compressible Ising model, respectively. In Chapter 4 the method and simulation techniques are discussed. Because of the remarkable flexibility of the MC method, physical systems as different as bulk and surfaces can be explored using very similar methodologies, so that only one chapter is needed to review them. Chapter 5 contains results that we obtained studying the (001) surface with standard single-atom moves. Those findings show that the standard MC approach introduced in Chapter 4 is unsatisfactory when simulating phenomena involving simultaneous motion of several particles, as it is the case for surface reconstructions or island evolution. The rest of chapter 5 is therefore dedicated to the development of the MC-MD hybrid algorithm. In Chapter 6 we present the most significant results obtained using the combination of *single-atom* and collective moves described in Chapter 5. These findings are mostly qualitative, and are intended to prove the efficacy of the algorithm. Because of that, only qualitative comparisons with experimental data discussed in Chapter 3 are possible. An example of quantitative evaluation of physical quantities is presented in this chapter as well, to show that the algorithm is also suitable for quantitative applications. Finally, in Chapter 7 we discuss results obtained using Si-Ge alloys to

study the compressible Ising model under constant volume conditions. Particular attention is paid to the determination of the phase diagram and to the investigation of the phase-segregated phase that is found at lower temperatures.

Chapter 2

Experimental and theoretical characterization of the Si(001) surface

One of the topics of this dissertation is the study of surface phenomena, like formation and stability of 1D and 2D islands on the Si(001) surface. For this reason a brief introduction to the physics of such a surface is presented in this introductory chapter.

The wide variety of phenomena that take place on the (001) surface of Si can only be understood in terms of the surface reconstruction. A brief account of this phenomenon is given in the following, before reviewing the most important experimental and theoretical findings related to the physics of step edges, terraces and islands on this surface.

2.1 The Si(001) surface: the dimer model

In the presence of a surface the bulk periodicity either remains unchanged (relaxed surfaces) or shows novel features (reconstructed surfaces), in which case the surface primitive cell is different from the bulk one. For silicon surfaces, as is the case for most covalent semiconductors, reconstruction is what happens. Moreover, because of the presence of strongly directional bonds, the specific reconstruction occurring on each surface is determined by the following criteria. Firstly, the reconstruction should minimize the number of broken (dangling) bonds per surface atom in order to minimize the increase in cohesive energy. Secondly, the bulk bond lengths must be preserved as much as possible, and, lastly, in symmetric environments the most

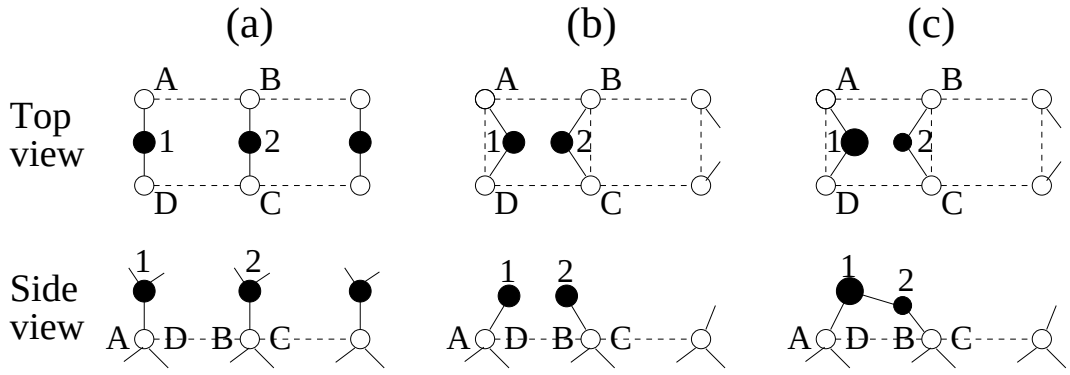

Figure 2.1: Si(001): a) ideal surface, b) symmetric dimer model and c) asymmetric dimer model. Solid circles represent atoms on the surface (larger circle in c) indicates the atom that protrudes out of the surface), open circles atoms in the plane just below the surface. Solid lines represent nn bonds, dashed lines nnn bonds.

favorable relaxation corresponds to an axial displacement of the trifold coordinated atom [2].

In the case of the (001) surface these criteria lead to the formation of dimers. When the bulk structure ends on a (100) surface two covalent bonds are broken for each surface atom. The easiest way to reduce the cost of such a surface is the creation of one new bond per surface atom. A new bond is indeed formed by moving two initially second nearest neighbors on the surface towards each other in such a way that all the distances between them and their nearest neighbors are kept as close as possible to their value in the bulk. The energy cost of forming such a new bond is low because of the small elastic energy associated with distortions in bond angles. The two atoms partecipating in this new bond are said to form a dimer. In the ideal case the length of the dimer bond is also close to the value that the nearest neighbors (nn) distance assumes in the bulk. All this is illustrated in Figure 2.1a) and b), where 1 and 2 are the surface atoms and A, B, C, D their nearest neighbors in the plane underneath the surface. The atomic rearrangement just described greatly stabilizes

the surface since it reduces the number of dangling bonds per surface atoms from two to one. Moreover, it also allows the two dangling bonds of a dimer to form a π-like bonding arrangement, which stabilizes the surface structure even further. Such a reconstruction, where pairs of surface atoms become covalently bonded, corresponds to the dimer model and is called a "symmetric reconstruction". To conclude, it must be mentioned that the dimers are formed so that they line up in rows, with the bonds parallel to each other [3]. The space between two adjacent rows is called a "trench" or "trough".

2.2 Other reconstructions

The symmetric dimer reconstruction is just the simplest kind of reconstruction possible for the Si(001) surface. A great number of experimental observations, mostly scanning tunneling microscopy (STM) measurements, have shown that in reality the ground state (GS) reconstruction is much more complicated than the simple dimer model suggests [4–9]. Much theoretical work has been done on the subject as well [10–15]. It is beyond the scope of this dissertation to review all these findings, and only a general description of such reconstructions will be provided here.

The origin of any surface reconstruction other then the symmetric one is in the buckling of the atoms composing the dimer. Experimental results have shown that dimers have a preference for a tilted geometry (buckling), with one dimer atom rising and the other lowering, relative to the surface plane [16] (Figure 2.1c)). The existence of buckling induces a charge transfer from the lower to the upper atom of the dimer. Since a tilted dimer has two possible orientations that are energetically equivalent, different reconstructions can be explained in terms of different arrangements of alternatively buckled dimers. When all the dimers are buckled in the same direction the reconstruction is called "(2x1)-asymmetric", instead, when the buck-

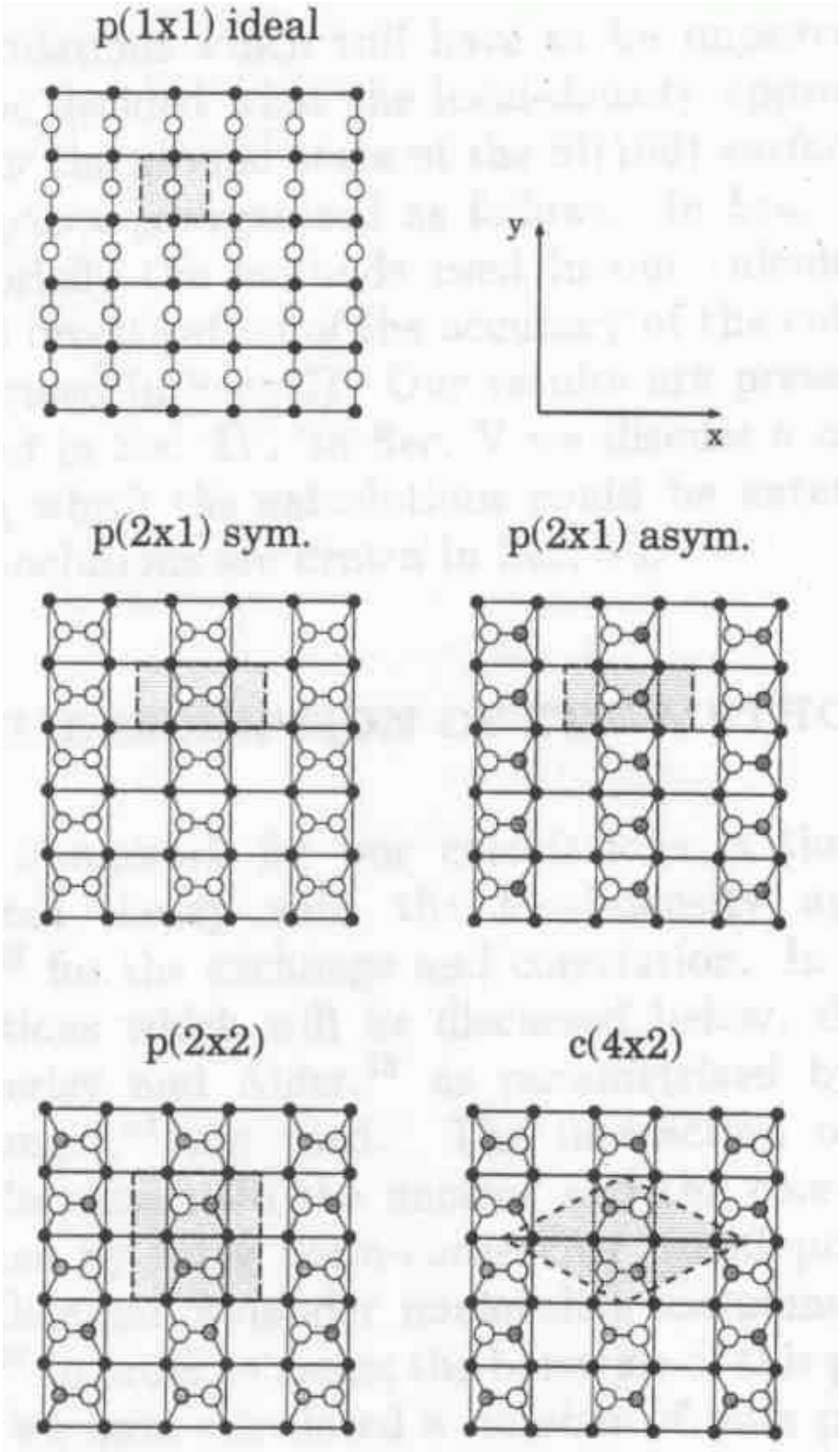

Figure 2.2: Top view of the (001) unreconstructed (ideal) and reconstructed surface. The black circles are 2^{nd} layer atoms and the larger gray and white circles are surface atoms. The large white circles protrude further out of the surface than the gray circles. (Ref. [14]).

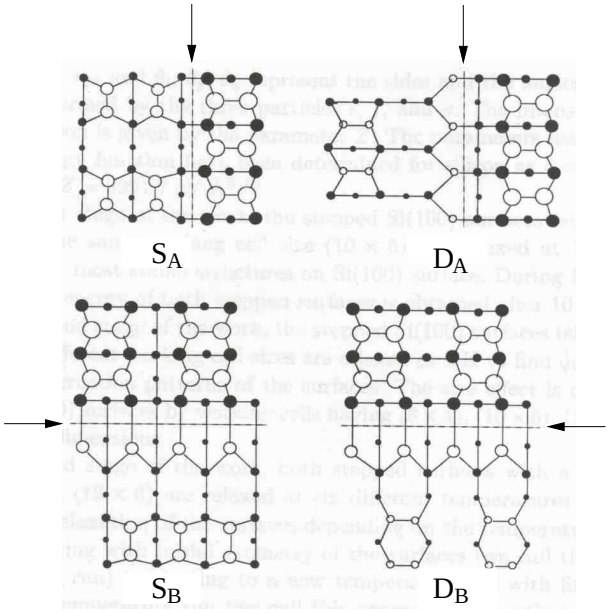

Figure 2.3: Top view of S_A, D_A, S_B and D_B types of steps on Si(001), respectively. The dashed lines indicate the step locations. Open circles denote atoms with dangling bonds. Larger circles are used for upper terrace atoms (Ref. [17]).

ling is alternated the reconstruction can either be p(2x2) or c(4x2) depending on the kind of alternation. All these different possible surface configurations are shown in Figure 2.2.

Lastly, it must be noted that every time dimers in a row are coupled in an anti-correlated manner, as in the c(4x2) case, they give rise to zigzag appearance along rows of buckled dimers. Experimental results show that such an anti-correlated pattern is never violated unless interrupted by an adsorbate or a defect.

2.3 Structure of terraces and step edges on Si(001)

Due to the crystal lattice structure dimer bonds on alternating layers are orthogonal to each other, which means that each monoatomic surface step separates two per-

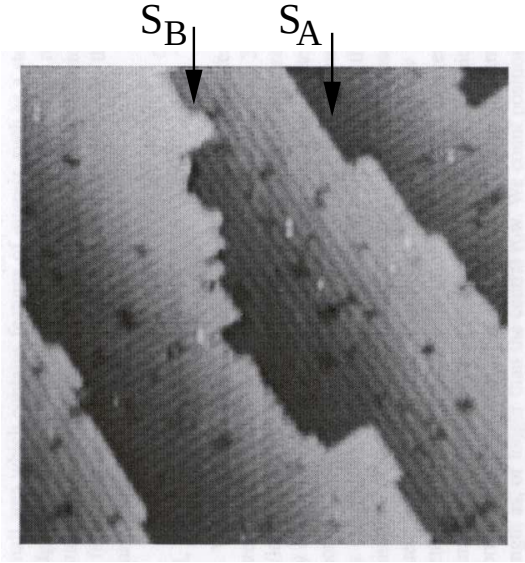

Figure 2.4: 300x300 $\AA^2$ STM image of the Si(001)-2x1 surface at 682 K. The type A (straight) and B (rough) step edges are clearly visible (Ref. [29]).

pendicular domains of (2x1) reconstruction. These are usually indicated as (2x1) and (1x2). As a consequence, two types of terraces exist on the surface: A-type terraces (T_A), having rows of dimerized atoms parallel to the edge of the down step (S_A step), and B-type terraces (T_B), with the dimer rows perpendicular to the down-step edge (S_B step). More complicated steps are also possible, as in the case of double-layer (D) heights, but those, too, are either of A or B type (D_A and D_B). All these different geometries are shown in Figure 2.3, and their formation mostly depends on the preparation method and the degree of misorientation of the (001) axis towards the [110] or [$1\bar{1}0$] direction.

In the case of T_B terraces, the S_B step has two different possible endings with respect to the substrate dimer rows. It can terminate either at the trough between the dimer rows (in which case the step is called nonbonded S_B) or on top of the dimer rows (re-bonded S_B). In the latter case, the edge atoms of the step rebond with those

in the last row of the lower terrace creating an energetically more favorable situation than the nonbonded one [18].

A very significant amount of theoretical and experimental work has been done studying monoatomic terraces, and the following conclusions have been reached [19–27]:

1) the diffusion on terraces is strongly anisotropic: adatoms and dimers diffuse much faster (of about a factor 10^3) in the direction of underlying dimer rows than in the perpendicular direction;

2) the S_B steps are much rougher (Figure 2.4) and advance faster during growth than S_A steps;

3) the most common defect on these terraces is missing dimers.

2.4 Intrinsic surface stress of Si(001)

The surface energy of a solid has, in general, two contributions: the formation energy and the deformation energy. The former reflects the breaking of bonds to make a solid surface; the latter reflects the tendency of a solid surface to distort because it is a quasi-2D system and hence would like to assume different atomic structure and bonding configuration from those of the bulk. The deformation energy gives rise to a nonvanishing surface stress.

For clean Si(100) the most important feature is the (2x1) reconstruction. Surface atoms form rows of dimers to reduce surface chemical energy by removing half of the dangling bonds, but at the expense of increasing surface strain energy because of the bond distortion. The surface stress introduced by the dimer reconstruction is highly anisotropic [30]. The stress $\sigma_{||}$ along the dimer bond is tensile (i.e. the surface atoms would like to be closer together along the bond direction than they

are), while the stress $\sigma_{\perp}$ along the dimer row is consequently compressive, or at least less tensile then $\sigma_{||}$. This stress anisotropy, F = $\sigma_{||}$ - $\sigma_{\perp}$, is predicted to cause morphological instabilities : a single-domain surface breaks up into a strip like structure with alternating domains. On a vicinal Si(100) surface the surface misorientation induces stress-domain structures consisting of alternating (2x1) and (1x2) domains separated by monoatomic steps [31].

2.5 Step edge evolution

In the study of step edge dynamics, both thermodynamics and kinetics considerations must be taken into account. Configurational free energies [40], i.e. thermodynamics, control the equilibrium surface step morphology while kinetics of mass transports regulates the kinetic stability of the surface. In other words, thermodynamics dictates, e.g., that steps will be rough if the kink formation energy is low. Kinetics, on the other side, regulates activation barriers for step-atom detachment, attachment, atomic or vacancy diffusion and so on, i.e. it determines at what temperature and on what time and length scale equilibrium configurations become frozen or metastable structures decay [38].

In the case of stepped Si(001), the most important kinetic processes responsible for the step evolution are: step-edge diffusion (SD), terrace diffusion (TD), and evaporation/condensation (EC), and their relative rates determine which one regulates the step edge shape. EC provides a source or sink of diffusing species; it is therefore the rate-limiting process if it is slow compared to either of the other two. In the limit of fast EC kinetics, on the other hand, TD determines the morphology if much faster than step-edge diffusion, and vice-versa.

In this dissertation the study of the surface behavior is conducted using simulations where the number of particles is always kept constant. The only mechanism

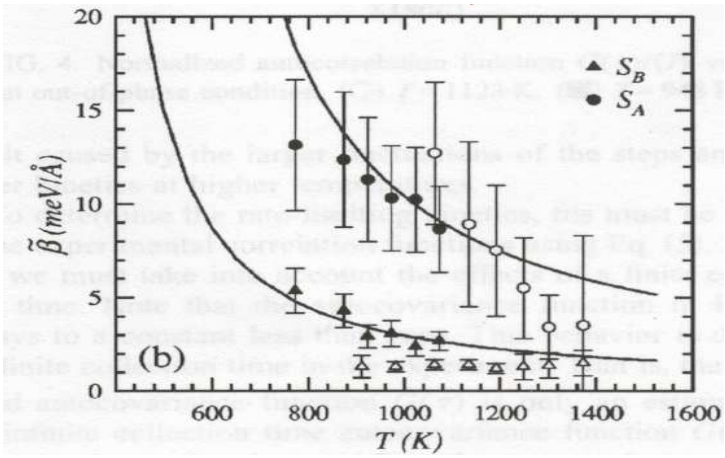

Figure 2.5: Step stiffness $\tilde{\beta}$ vs temperature for S_A and S_B steps. Solid symbols correspond to data measured in Ref. [34], open symbols to data measured in Ref. [41] (Ref. [34]).

regulating step evolution included in our calculations is therefore step-edge diffusion. Experimentally, though, the three processes are observed at the same time. It is important for us to briefly analyze some of these findings in order to identify the temperature range for which SD dominates the step evolution.

The determination of the rate-limiting process for step kinetics has been addressed in several experimental works [32, 34, 41, 42]. All the results agree in measuring a much higher step-edge stiffness for S_A steps than for S_B (Figure 2.5), which would explain the qualitative observation that S_B steps are rougher that S_A steps. For a precise definition of the step stiffness see Appendix A. On the contrary, some works [32, 41, 42] find SD to determine the step morphology for all temperatures between 913 and 1443 K, while others [34] restrict this range to 800-1000 K only. From the same measurements activation energies for step diffusion can be evaluated, and 0.8 ± 0.2 eV is what is found in Ref. [34]. It is beyond the scope of this dissertation to investigate the evolution of step growth as more and more atoms

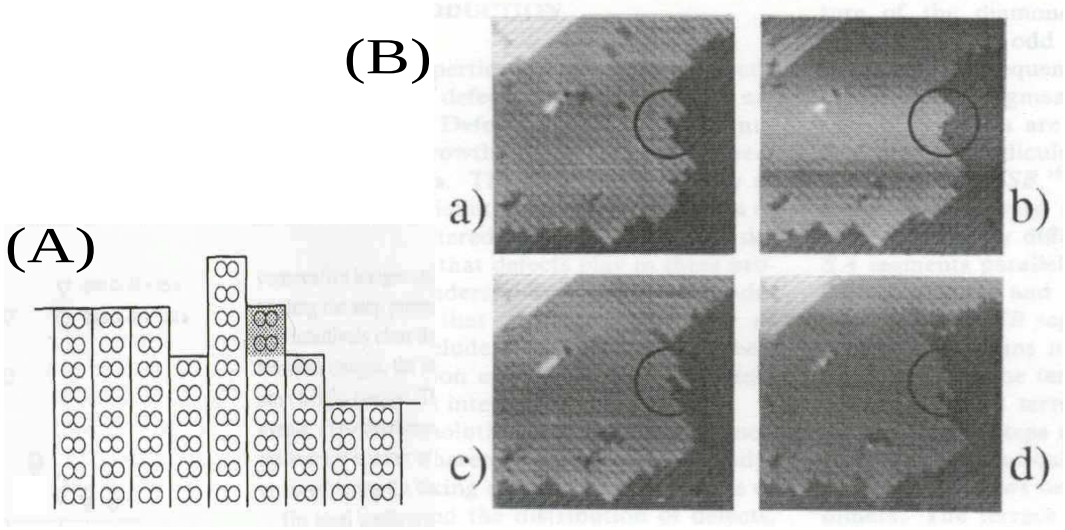

Figure 2.6: (A) Schematic model of the rough step. The shaded region is an example of the smallest unit that comprises observed changes at the step. (B) Four sequential 300x300 $\mathring{A}^2$ STM images of the Si(001) surface taken at 245 C showing step rearrangement events occurring between images. Each image was acquired in about 15 sec. (Ref. [38, 39]).

are deposited on the surface because it doesn't correspond to any of the physical processes that we analyzed, but a very accurate description of such a phenomenon can be found in Ref. [28].

In the following, the mechanism behind step diffusion is discussed on the atomic scale, i.e. kink evolution (diffusion, creation and annihilation) is analyzed. Looking at the geometry of the Si(001) surface it is easy to realize that no kinks smaller than two atoms can occur on this surface. The formation of a one-atom kink would in fact require the breaking of a dimer, and this is energetically very expensive. Experimentally it is found that kink events are always comprised of units of at least four atoms (two dimers) [33, 38, 39](Figure 2.6). The reason for this is that monoatomic-height terraces of type A and B are alternatively grown on the (001) surface, so that kinks steps S_A are comprised of segments of S_B steps, and vice-

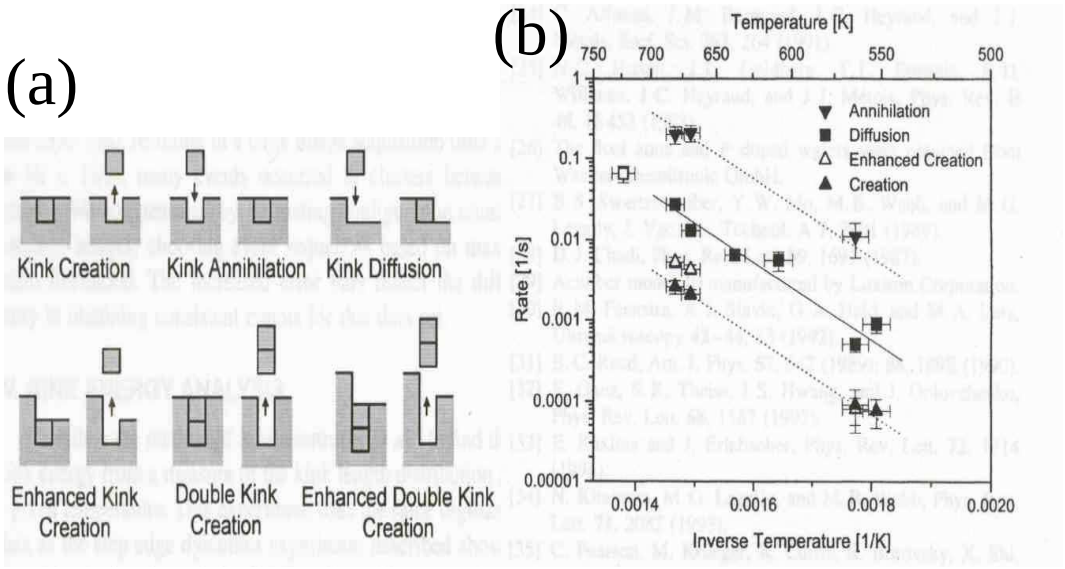

Figure 2.7: (a) Schematic diagram showing kink creation, annihilation, diffusion, enhanced creation, double creation and enhanced double creation events. (b) Arrhenius plot for four kink processes. The solid line corresponds to an activation energy of 0.97 eV. (Ref. [29, 33]).

versa. A four-atom kink is therefore energetically favorable because the lower surface [18, 36, 43] has a two-atom periodicity perpendicular to the step.

Using STM in a temperature range between 500 and 700 K, Pearson *et al.* [29,33] studied the rates at which events like kink creation, kink annihilation and kink diffusion occur (Figure 2.7a). From their data it appears that kink creation events are rare because the starting configuration (a flat segment of step edge) is quite a stable one. It is possible, however, that not all the creation events that occurred have been recorded during the experiment because a rapid annihilation may have healed the edge before the next STM image was taken. For an annihilation event to happen, a starting configuration with a kink-antikink pair is obviously needed. Very few events of those kinds are observed because the kinks creation rate is low and the annihilation rate is high. Finally, the kink diffusion is observed to be the dominant

process: as there is no change in the step length for a kink diffusion event, the energy difference between the initial and the final state is small, making this phenomenon very common. More generally, because it is the final state energy to determine the relative rates for all these processes, the following rules are found to hold:

- events that reduce the total step length, i.e. kink annihilation, occur at a faster rate;

- events that increase the total step length (kink creation) occur at a slower rate;

- corner-healing events occur at a much higher rate then ordinary diffusion events. This is interpreted to be due to the fact that the corner energy E_c is higher than kink energy ε_S (see Appendix A);

- local configurations can affect event rates: for example it is determined that the presence of a kink increases events rates up to a factor of two. This is shown in Figure 2.7b), where the creation rate is shown to have doubled in the case of enhanced creation.

Extensive studies of the dependence of the atomic arrangements of the steps on the local configuration were done by Swartzentruber *et al.* [36,38,39] using variable-temperature scanning tunneling microscopy. Temperatures between 490 and 620 K were investigated. This temperature range was chosen because the steps were found to be stable on the time scale of hours for temperature lower than 490 K, and to rearrange on a time scale much faster than the scanning time for T above 620 K. From these measurements it appeared that the four-atom unit detached from one dimer column doesn't reattach at one of the two neighboring columns. In fact, no identifiable correlation between detaching and attaching units was found within the area of the STM images except for detailed balance. Moreover, formation, diffusion and annihilation of surface vacancies were observed at the same time as the

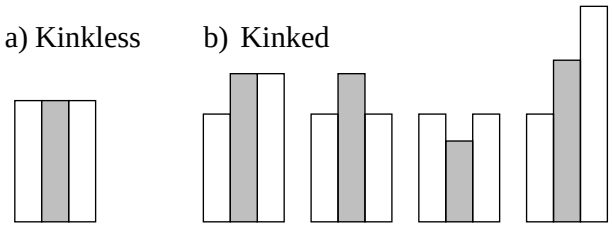

Figure 2.8: Schematic representation of *kinkless* vs *kinked* columns. (Ref. [39]).

kink events, especially at higher temperatures. Qualitatively, it was noticed that the average position of the steps remains constant during the observation time, i.e. the observed rearrangement events were equilibrium fluctuations. When considering how the event rate depends on the local step configuration, it is important to distinguish between *kinked* and *kinkless* columns. Columns are called *kinked* when the dimer row that terminates at the step has at least one neighboring kink, *kinkless* otherwise (Figure 2.8). Experimental data tell that, in the temperature window between 490 and 620 K, the relative probability that an event happens at a kinked column is 2.5-3 times higher than at a kinkless one. Assuming that the relative rate is given by the Boltzmann factor of the energy difference between the activation barriers at the two types of step configurations, the authors estimated an energy difference ΔE of 180±60 meV that is consistent with the configurational energy difference between kinked and kinkless regions of the step [36, 43].

2.6 **1D and 2D islands**

In the following, the main characteristics of mono- and bidimensional silicon islands on Si(001) are briefly reviewed. The early stages of nucleation are analyzed first, then the island stability as a function of temperature, shape and/or size is discussed. This

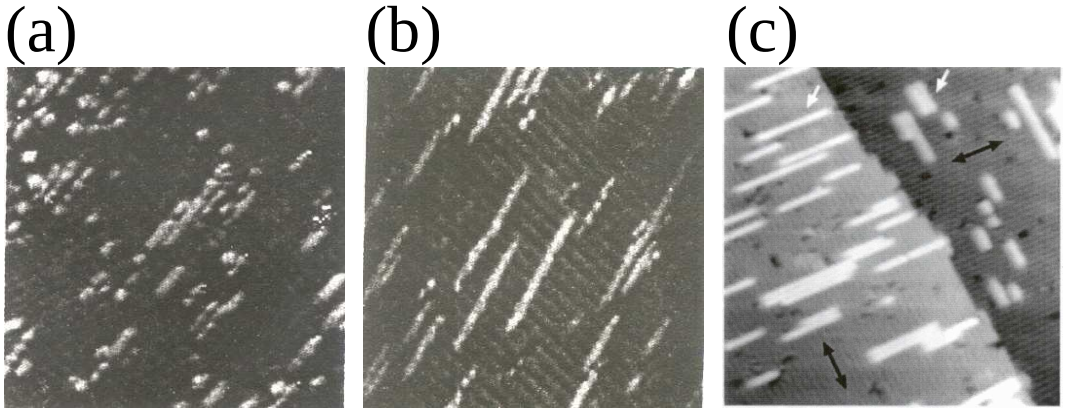

Figure 2.9: STM micrographs of islands shapes and distributions for growth at a rate of 1/200 ML (monolayer) per second to a coverage of 0.2 ML at (a) 300 K and (b) 475 K. Scale of the micrograph is 230x230 $\AA^2$. (c) 40 nm x 40 nm image of the Si(001) surface at 536 K showing many small Si islands. The direction of fast monomer diffusion is parallel to the dimer rows, indicated by the black arrows. Examples of 1D and 2D islands are indicated with white arrows. (Ref. [19, 45]).

review doesn't mean to be exhaustive; important phenomena like Oswald ripening [42] won't be discussed because they do not have a counterpart in our simulations.

2.6.1 **Early stages of nucleation**

Several STM studies [19, 45, 46] have shown that Si atoms form islands that are a single dimer row wide (1D islands) when deposited at a low rate, for temperatures between room temperature and 500 K and coverages of a fraction of a monolayer (Figure 2.9 a) and b). At slightly higher temperatures both 1D and 2D islands have been observed (Figure 2.9 c)). The long axis of these 1D islands is always aligned perpendicular to the substrate dimer rows, and typical aspect ratios are about 15:1. Two main models have been proposed to explain this strong anisotropy. One is a kinetic model based on sticking anisotropy [19], where an end-site is supposed to be roughly 50 times more likely to gain a block (i.e at least two dimers at one time) than

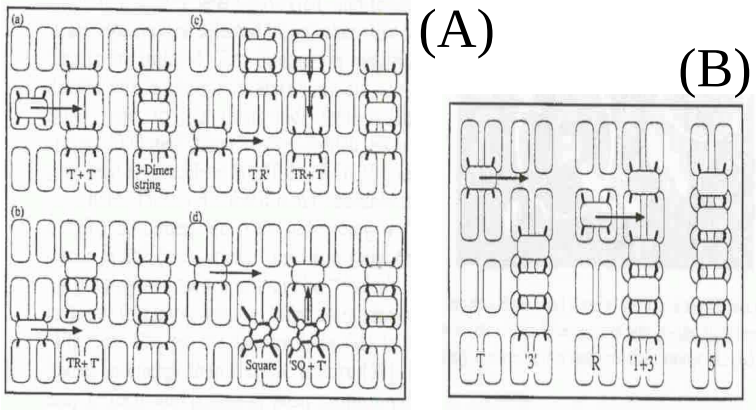

Figure 2.10: (A) A schematic diagram of possible nucleation pathways. The energetically favored one is (d), where a trench dimer can attach to either end, and then the "square" would break up into two dimers as a dimer string (see text). (B) A schematic picture of the growth process for a dimer string (Ref. [46]).

a side site. The second model is based on an exchange mechanism [47] between an adatom arriving on the side of the silicon island and an existing island atom on top of the island itself. The displaced atom diffuses rapidly along the top of the island (the direction of fast diffusion) until reaching an end, where it falls over the edge and sticks. Experimental evidence seems to support the former model more than the latter [45].

Owen *et al.* [46] identified dimers strings that are one dimer wide and three dimers long as the smallest immobile island on Si(001) at 570K. In their work they considered several possible nucleation pathways and growth processes for the dimer strings, all starting from nucleus structures given by structures composed of two dimers (Figure 2.10). They also established the lowest energy barrier for the formation of dimers strings to be about 1.5 eV.

As for theoretical models, solid-on-solid Kinetic Monte Carlo simulations have been successfully used to study island nucleation and island anisotropy on the Si(001)

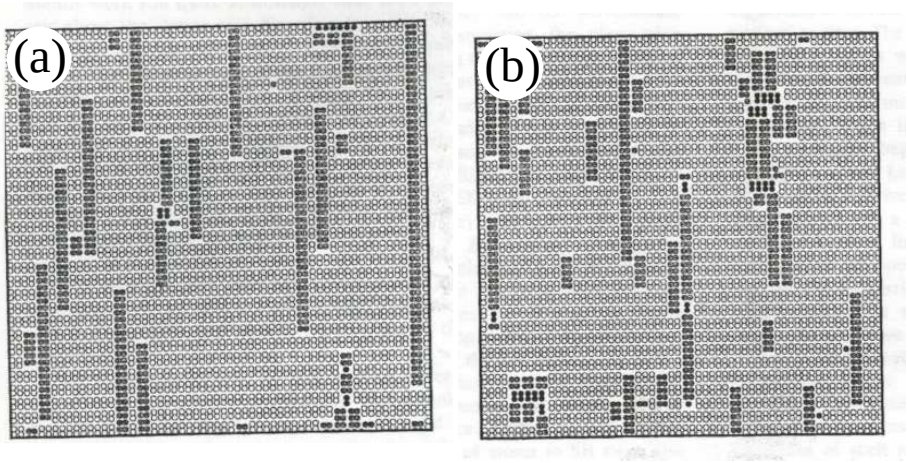

Figure 2.11: Calculated surface structures after 0.2 monolayers of growth at 300 C on initially flat surfaces for different values of the parameter E_A (E_A=-0.05 eV in (a) and 0.10 eV in (b)). E_B=0.05 eV for both. Open circles indicate the surface, gray circles the second level and black circles all the higher levels (Ref. [48]).

surface [48]. Example of results are shown in Figure 2.11. The main limitation of these models is the fact that they require a pre-knowledge of the possible diffusion mechanisms so that simulation results are dependent on how well a large number of parameters is fitted. Moreover, the solid-on-solid model utilizes rigid lattices, so that restrictions to the atomic motion are introduced.

Using the nucleation theory developed by Tersoff *et al.* [49], Theis *et al.* [50] estimated a critical nucleus size (R_c) of about 650 dimers for islands on Si(001) at 900K. They also found that R_c increases with temperature as a thermally activated quantity with an activation energy of about 0.6 eV.

2.6.2 **Growth and equilibrium island shapes**

The shapes of Si islands on Si(001) have been extensively investigated both during growth and at equilibrium [19, 41, 45, 51]. As a result, it was established that the

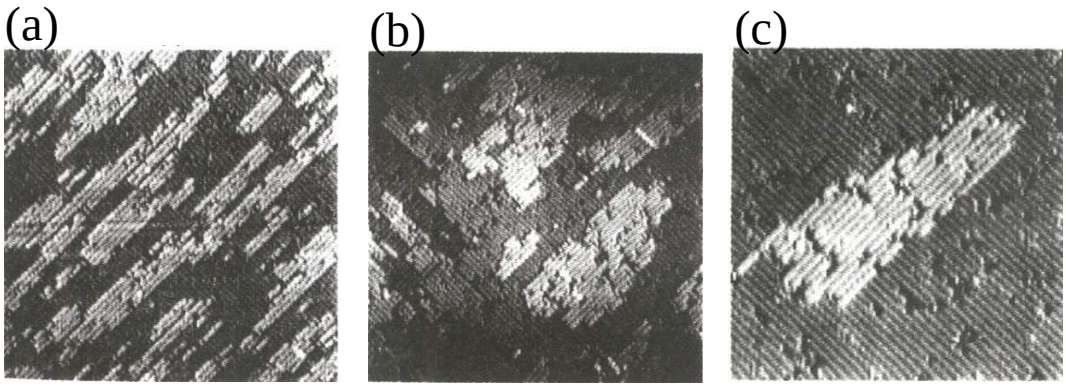

Figure 2.12: STM micrographs of island shapes: (a) as deposited, for deposition of 0.5 ML of Si at 1/20 ML/sec and 575K, (b) after annealing for 10 min at 575 K, (c) after annealing structures such as those in Figure 2.9 at about 600K for 2 min with the flux off. Scale for (a) and (b) is 500x500 $\mathring{A}^2$, for (c) is 320x320 $\mathring{A}^2$ (Ref. [19]).

anisotropic island shapes observed during growth are to a large degree a kinetic effect. As temperature rises, for example during annealing, the islands grow, become more widely dispersed and adopt a more rounded shape (Figure 2.12). The measured aspect ratio changes from about 0.685 at 1100 C to 0.39 at 700 C [41]. The equilibrium aspect ratio of 3:1 corresponds to the fact that the S_A steps are about three times more stable than S_B ones. As shown in Figure 2.12c) a typical equilibrium island shows a great number of missing dimers (dark spots on the island) and a shape still far from being circular. Moreover, the S_A steps, which are along the dimer rows of the island, have straight edges and the S_B steps, which are perpendicular to the dimer rows, include many kinks.

From the analysis of the thermal decay for islands on Si(001) [51] it was determined that stable islands decompose after kinks are created at the S_B step edges. Decay curves are approximately linear in most cases, although decay rates fluctuate during several stages of the decay. In general, decay rates for the Si(001) islands are about 100 times larger than those of the Si(111) ones at the substrate temperature

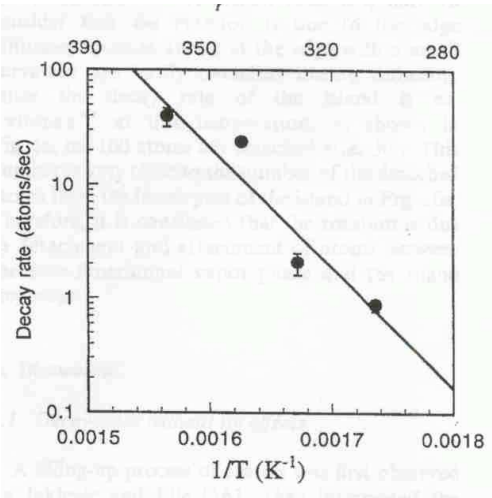

Figure 2.13: Arrhenius plots of the decay rates for Si(001) islands (Ref. [51]).

of about 400 C. The Arrhenius plot of the decay rates for Si(001) islands is shown in Figure 2.13, from which an activation energy of 2.1 eV and a pre-exponential factor of $10^{18\pm4}$ s^{-1} are determined.

Chapter 3

Characterization of the phase diagram for bulk $Si_{1-x}Ge_x$ alloys

The compressible Ising model has been widely utilized throughout the last few decades to simulate very different systems and physical phenomena [56–62]. It is particularly appropriate for describing phase transitions in alloys where the ordering is accompanied by lattice distortions. The role of elastic degrees of freedom in a system near criticality has also long been an object of debate [63–65]. Several studies have been conducted to characterize the behavior of the compressible Ising model under constant-pressure conditions using the language of binary alloys [64–69]. In these works a binary mixture of Si and Ge was simulated with the interatomic interactions modeled using different classical potentials (Tersoff [70], Stillinger-Weber [1], and Keating [71]). The analysis of the compressible Ising model under constant-volume conditions, on the contrary, has been mostly unaddressed [63, 72] and is the subject of part of this dissertation. Because of theoretical predictions [74], we expect results significantly different from those obtained in the constant-pressure case.

In a generic compressible Ising model two sets of variables are considered: the spins s_i=$\pm$1 and the displacements $\underline{u}_i$ which define the motion of the spin from the original lattice site i. Given an initial position $\underline{r}_i^0$, the actual position of the spin during the simulation is therefore $\underline{r}_i = \underline{r}_i^0 + \underline{u}_i$. The interactions between the spins depend on the distance between them, so that a general Hamiltonian for this system can be written as

$$\mathcal{H} = KS + hM = K\mathcal{H}_{pot} + hM \tag{3.1}$$

where K is the coupling constant, S=$\mathcal{H}_{pot}$ is the contribution due to the classical potential, where the dependence on the interatomic distances is included, h is the external field and M the magnetization. As an example, Equation 3.1 becomes

$$\mathcal{H} = -J \sum_{i,j} \sigma_i \sigma_j - h \sum_i \sigma_i \tag{3.2}$$

when applied to the Ising model.

To facilitate comparisons with constant pressure results, we decided to adopt the same binary alloy picture used in Ref. [64, 65], where bulk $Si_{1-x}Ge_x$ was simulated. Moreover, Si-Ge alloys are very good systems to study the effects of having a fixed volume when the relative concentration between species is changed, because Si and Ge are chemically very similar but differ in size. Ge is slightly bigger than Si (about 4%) so that a compressive or tensile stress acts on the system as the composition varies if the volume is kept constant. This global effect adds to the elastic forces in determining the system behavior, resulting in a different and wider variety of phenomena, sometimes very localized, than under constant-pressure conditions (Chapter 7).

In the following the most important results obtained for bulk $Si_{1-x}Ge_x$ phase diagram for fixed pressure are briefly reviewed, as are predictions for constant volume.

3.1 Phase diagram under constant pressure conditions

Very detailed studies of the phase diagram and related properties of bulk $Si_{1-x}Ge_x$ under constant pressure conditions (P=0) have been conducted by Kelires *et al.* [66], Dünweg *et al.* [64] and Laradji *et al.* [65] using Monte Carlo simulations in the grand-canonical ensemble (see Chapter 4). Classical potentials (Tersoff in Ref. [66], Keating in Ref. [64] and Stillinger-Weber in Ref. [65]) were utilized to model the inter-atomic elastic interactions. All the results presented below are gathered from such references. Each atom was given four degrees of freedom: one, discrete, given by the nature of

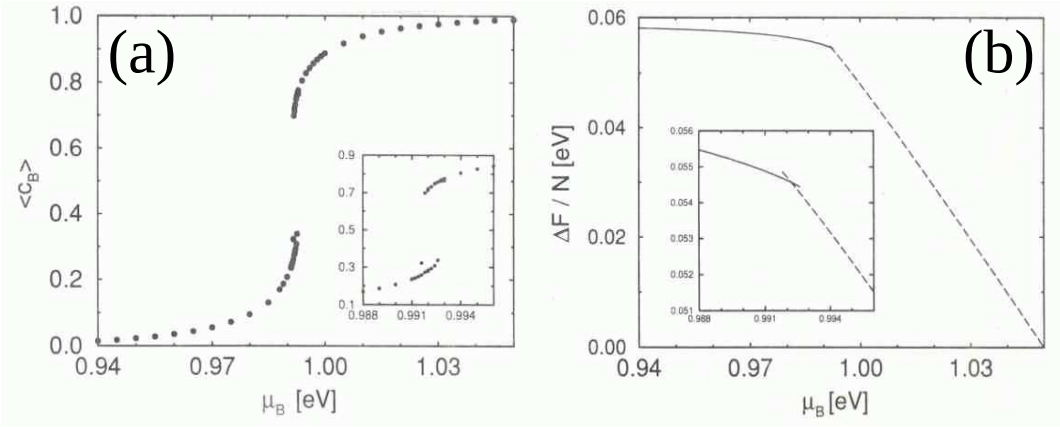

Figure 3.1: (a) Hysteresis loop of $\langle c_B \rangle$ versus μ_B at $k_B T$=0.026 eV (about 94% $k_B T_c$) calculated using Keating potential. (b) The branches of the free energy corresponding to (a). The insets show the transition regions on an expanded scale (Ref. [64]).

the atom (pseudospin) and the other three corresponding to its position, moreover, only nearest-neighbor interactions (nn) were considered. Such a model corresponds to a compressible Ising model, even if, as pointed out by Dünweg *et al.* [64], not necessarily to a standard one. This because the latter requires that the displacement field couples to the square of the spin field [63], while our coupling is linear.

Independent of the potential utilized in the simulations, at low temperatures hysteresis is found in Ge concentration (x) when sweeping through the chemical potential difference $\Delta=(\mu_{Si}-\mu_{Ge})/2$ at fixed temperature. As a consequence, a two-phase coexistence region is found, corresponding to a first order line in the grand-canonical ensemble. One example of such hysteresis loops is shown in Figure 3.1a) for T about 94% T_c. Note that the jump in concentration between the two branches at the transition μ_B (B=Ge) covers a significant interval of concentration (roughly from 0.3 to 0.75). As it will be discussed in Chapter 7, a very different situation is encountered in the constant volume case. For each analyzed temperature, the value of μ_B correspondent to the transition (μ_B^t) is evaluated from the crossing of the free

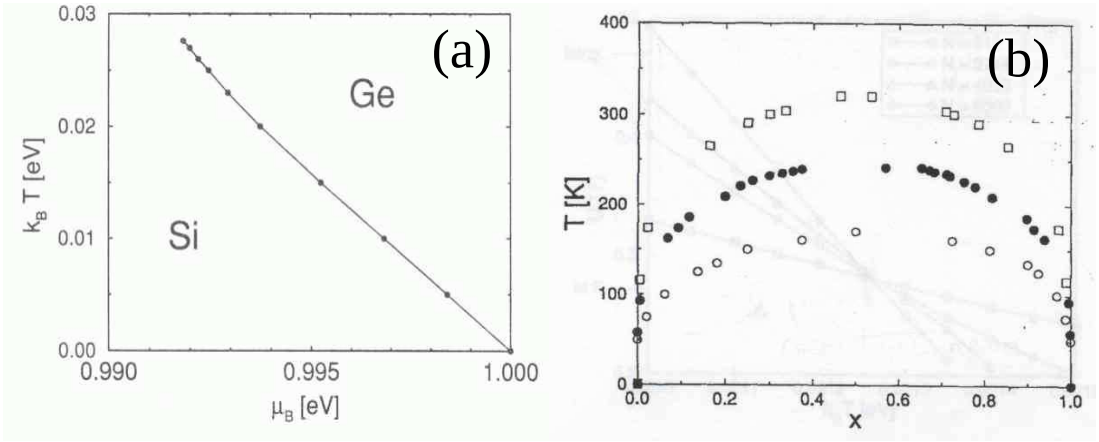

Figure 3.2: Phase diagram in the grand-canonical (a) (Ref. [64]) and canonical (b) (Ref. [65]) ensembles. Data in (a) are obtained using Keating potential, while in (b) open squares correspond to Keating, solid circles to Stillinger-Weber and open circles to Tersoff potential.

energy branches (Figure 3.1b)). Once that μ_B^t is known, the coexisting values of x are determined from the hysteresis loops. A similar method is used in this dissertation as well (Chapter 4), so that the behavior shown in Figure 3.1b) will be compared to the one found at constant volume.

The final determinations of the phase diagram in the canonical and grand-canonical ensembles are shown in Figure 3.2. The overall shape of the curve is independent of the choice of the potential, only the values of T_c differ. The slight asymmetry is due to the lack of any spin-up/spin-down symmetry resulting from inequivalency of Si and Ge. From a detailed finite size analysis of the critical behavior it was determined that the first order line ends in a critical point belonging to the mean-field universality class (again, for both the Keating and the Stillinger-Weber potentials). The same analysis provided more accurate estimates of the critical temperature: $k_B T_c$=0.02762 eV (320.5 K) when using the Keating potential and 0.02125 eV (246.6 K) when using the Stillinger-Weber one. Lower values (T_c about 170K)

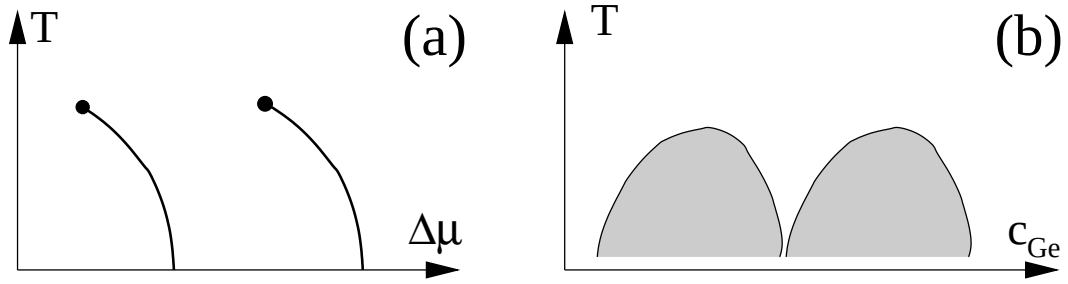

Figure 3.3: Schematic phase diagrams as predicted under constant volume conditions in the ($\Delta\mu$,T) plane (a) and in the ($\Delta\mu$,c_{Ge}) plane. In (a) the two curved lines indicate two first order transitions, each ending in a critical point. The shaded areas indicate coexistence regions.

were found by Kelires and Tersoff [66] and de Gironcoli *et al.* [73]. At higher temperatures a disordered phase was found.

An evaluation of the effect of the elastic part of the Hamiltonian was performed by comparing the estimated valued of T_c to the one obtained when the elastic contribution is turned off, i.e. using a rigid lattice. This latter model is the well known ferromagnetic nearest-neighbor Ising model on the diamond lattice and for both the Keating and the Stillinger-Weber potential T_c so determined is roughly half of what found including the elastic interactions.

3.2 Phase diagram under constant volume conditions

A few theoretical studies have been performed on the compressible Ising model under constant volume conditions, starting from the work of Bergman and Halperin [63], but very little consistency is found in the results mostly because of the differences in the models used. Up to now, no simulations have been conducted under constant volume conditions on a binary system with mismatch between the two species, as it is the case here. A theoretical treatment of the problem has been conducted by

Dünweg [74] in terms of a Landau-Ginzburg-Wilson Hamiltonian. As a result, two first order lines are predicted in the grand-canonical ensemble, each ending in a critical point of mean-field character (Figure 3.3). The first order transitions are determined to be field driven and, at low temperatures, not only a "mostly Si" and a "mostly Ge" phase are expected, as in the constant pressure case, but also a "50-50" (equal number of Si and Ge) one. No details on the nature of this new phase are given. This analysis was conducted under the condition of linear coupling between the displacement field and the spins and with the assumption of negligible elastic energy of the phase boundary.

Chapter 4

Model and standard simulation techniques

The topic of this dissertation is the study of the Si(001) surface in the presence of Si or Ge adatoms and of the compressible Ising model at constant volume using the binary alloys representation. Both studies are performed using Monte Carlo methods. Because of the remarkable flexibility of this simulation technique, physical systems as different as bulk and surfaces can be explored using very similar methodologies. In the following the model adopted for studying both bulk and surface is presented first, then simulation details for each case are given. In the second part of the chapter the most important techniques used in our simulations (bulk or surface) are briefly reviewed. Here no distinction is made between the two cases because several of the techniques were employed in both studies.

4.1 Model

In our bulk simulations we considered a binary alloy where each atom is given four degrees of freedom: three describing the position (vector $\mathbf{r}_i$) and one, discrete, describing the atomic species (pseudospin). This model is completely equivalent to a compressible Ising model which was described in Chapter 3. When simulating surfaces, the possibility of changing atomic species was usually turned off because our primary interest was to develop an efficient algorithm to simulate the surface evolution. Most of the simulations were, therefore, done to test the algorithm more than to evaluate physical quantities, and only one atomic species was considered (Si

on Si(001)) to simplify the problem as much as possible. However, the program was written allowing the possibility of two species and at the end of Chapter 6 a few results obtained for Ge/Si(001) are presented.

For bulk studies the interatomic interactions are modeled using the classical Stillinger-Weber potential [1] (SW) and only nn interactions are considered. When studying the surface, we are interested in a representation of materials as close to reality as possible, so that the choice of the potential was quite critical. Together with the SW we originally tried the Tersoff potential (T) [70, 75] as well, but our results showed that for surface applications SW is also the best choice (Chapter 6, [76]). Because of that, most of the results presented in Chapter 6 have been obtained using SW (it will be indicated when otherwise). In the following both potentials are briefly reviewed.

In the Stillinger-Weber potential the atomic energies are given by the combination of a two-body term ($\mathcal{H}_2$) dependent on the interatomic distances and a three body term ($\mathcal{H}_3$) function of the nn angles. Its explicit form is the following:

$$\mathcal{H}_{\mathcal{SW}} = \mathcal{H}_2 + \mathcal{H}_3 \tag{4.1}$$

$$\mathcal{H}_2 = \sum_{<i,j>} \varepsilon(S_i, S_j) F_2[r_{ij}/\sigma(S_i, S_j)] \tag{4.2}$$

$$\mathcal{H}_3 = \sum_{<i,j,k>} [\varepsilon(S_i, S_j) * \varepsilon(S_j, S_k)]^{1/2} * [\lambda(S_i)\lambda(S_j)^2\lambda(S_k)]^{1/4} * F_3[r_{ij}/\sigma(S_i, S_j)] * (cos\theta_{i,j,k} + 1/3)^2 \tag{4.3}$$

$$F_2(y) = \begin{cases} A(\frac{B}{y^p} - \frac{1}{y^p})e^{\delta/(y-b)} & \text{for } y < b \\ 0 & \text{for } y \geq b \end{cases} \tag{4.4}$$

$$F_3(y_1, y_2) = \begin{cases} e^{\gamma/(y_1-b)+\gamma/(y_2-b)} & \text{for } y_1 < b,\ y_2 < b \\ 0 & \text{otherwise} \end{cases} \tag{4.5}$$

The Tersoff potential includes only nn distances and angles as well, but acquires a many-body character because it weights the contribution of each interaction with factors depending on the local environment. This can be seen more clearly by looking at the explicit form of such a potential:

$$\mathcal{H}_T = \sum_i E_i = \frac{1}{2} \sum_{<i,j>} V_{ij} \tag{4.6}$$

$$V_{ij} = f_c(r_{ij}) * [f_R(r_{ij}) + b_{ij}\, f_A(r_{ij})] \tag{4.7}$$

$$f_R(r_{ij}) = A_{ij}\, \exp(-\lambda_{ij} * r_{ij}) \qquad f_A(r_{ij}) = -B_{ij}\, \exp(-\mu_{ij} * r_{ij}) \tag{4.8}$$

$$b_{ij} = \chi_{ij}\, (1 + \beta_i^{n_i}\, \zeta_{ij}^{n_i})^{-1/(2n_i)} \qquad \zeta_{ij} = \sum_k f_c(r_{ik})\, g(\theta_{jik}) \tag{4.9}$$

$$g(\theta_{jik}) = 1 + \frac{c_i^2}{d_i^2} - \frac{c_i^2}{d_i^2 + (h_i - cos\theta_{jik})^2} \tag{4.10}$$

For each atom i, each attractive interaction $f_A(r_{ij})$ is weighted by the factor b_{ij} containing the quantity ζ_{ij} which depends on all the angles centered on i and involving j, i.e. on the local environment of atom i. This potential is computationally more demanding than SW, and, for example, V_{ij} is different from V_{ji}. $f_c(r_{ij})$ is a standard cutoff function. The value of the parameters are given in Ref. [65] for SW, Ref. [75] for Tersoff.

When we are interested in the possibility of changing the relative concentration of the two atomic species, i.e. when studying the bulk Si-Ge phase diagram under constant volume conditions, we add a one-body term to the Hamiltonian:

$$\mathcal{H} = \mathcal{H}_1 + \mathcal{H}_{pot}; \qquad pot = SW, T \tag{4.11}$$

$$\mathcal{H}_1 = -\mu_A N_A - \mu_B N_B \tag{4.12}$$

where A(B) indicates the atomic species (Si or Ge in our case), μ and N the chemical potential and the number of atoms of each species, respectively. Obviously, this term is just a constant if the number of atoms of each species is kept constant during the

simulation, while it becomes meaningful otherwise. All our bulk simulations are performed in the semi-grand-canonical ensemble, i.e. keeping the total number of atoms in the system ($N = N_A + N_B$) constant, but changing the number of atoms of each species ($N_A, N_B \neq$ const). Under these conditions $\mathcal{H}_1$ becomes:

$$\mathcal{H}_1 = -(\mu_{Ge} - \mu_{Si})N_{Ge} + const = -\Delta\mu N_{Ge} + C; \qquad C = -\mu_{Si}N \tag{4.13}$$

Lastly, it is necessary to remark that a consequence of using this model for surface simulations is the impossibility of correctly reproducing the dimer buckling (Chapter 2). The tilting effect is created in the dimer because of charge transfer from one atom to the other and can not be reproduced by classical potentials, at least SW and T are equally incapable of doing it. This limitation precludes the usage of this method to investigate which reconstructions correspond to the GS, but it does not represent a problem in this study because all the analyzed phenomena are driven by the coarse geometry of the system, in particular by the presence of dimer rows, and this is well described in the model.

4.2 Simulation methodology

The simulation method employed in this dissertation is importance sampling Monte Carlo (MC). The physics of bulk and surfaces is significantly different, so that different simulation methodologies have to be considered. Each case is therefore discussed individually in the following.

4.2.1 Bulk investigation

For the determination of bulk properties at constant volume our simulation cell consists of a cubic LxLxL cell constructed along the (100), (010) and (001) directions (L being the number of diamond conventional cells used along the x, y or z direction). Such a cell contains N=8×L^3 atoms. The conventional cell for the diamond lattice is

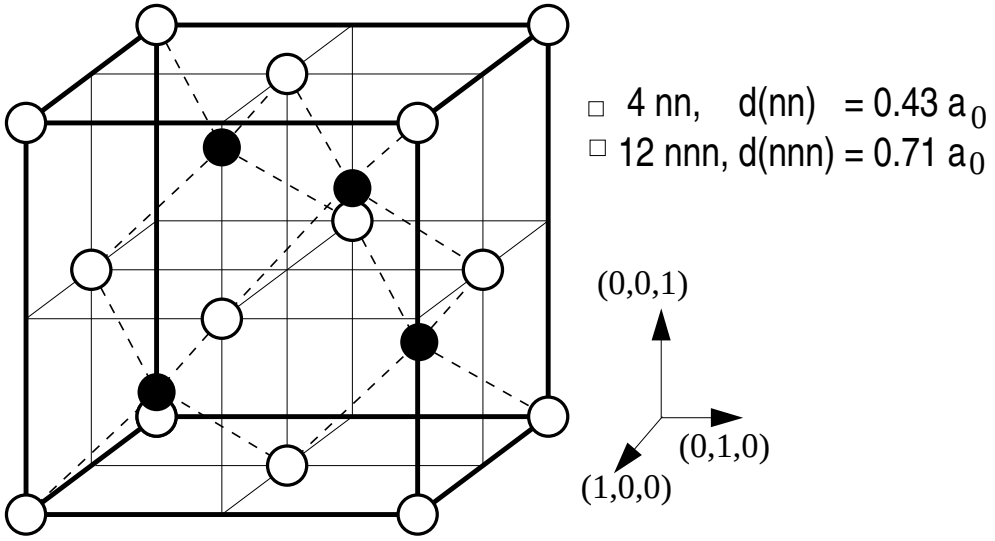

Figure 4.1: Conventional cell for diamond lattice. The open and solid circles indicate the atomic position for species A and B, respectively; a_0 indicates the lattice constant. nn bonds are indicated by dashed lines.

shown in Figure 4.1. We considered 3D periodic boundary conditions (PBC) because we wanted to eliminate surfaces and allow extrapolation to bulk behavior.

We decided to use a volume V corresponding to a lattice constant a_0 (lattice constant for the diamond conventional cell) of 5.5929 $\mathring{A}$, i.e. 1.03 times a_0 in pure silicon ($V=L^3 \times a_0^3$). Remembering that $a_0(Ge) = 1.04\ a_0(Si)$, it is easy to see that this choice is closer to the Ge equilibrium volume than to the Si one, and that a 75-25 mixture (75% Ge concentration) corresponds to the ideal, i.e. unstrained, composition. This choice of volume is motivated by the desire to enhance the difference between Si and Ge and results in having significant compressive or tensile stress acting on the system as the composition varies.

As mentioned earlier, all our simulations were conducted in the semi-grand-canonical ensemble so that the phase diagram was determined in the (c_{Ge},T) plane (c_{Ge}=Ge concentration). As is obvious from Equation 4.13, only the chemical poten-

tial difference ($\Delta\mu = \mu_{Ge} - \mu_{Si}$) has physical meaning, not the individual values of each chemical potential. Moreover, from Equation 4.13 it can be seen that it is the value of $\Delta\mu$ to determine c_{Ge} so that the $\mathcal{H}_1$ term in Equation 4.12 can be interpreted as an external field acting on the system.

Lastly, it is important to remark that our simulations were performed "semi-on-lattice". This means that the atoms were allowed to move from their equilibrium positions on the nodes of a diamond network, but the lattice coordination could not change. This means that the atoms nn of a given atoms i remain nn of such an atom for the whole duration of the simulation, but that the value of their distance from i (d_{ij}) could change every Monte Carlo step (MCs). This assumption was introduced because it significantly speeds up the calculations allowing us to compute the list of neighbors (Verlet list) only once at the beginning of the simulation, rather than every n steps. It is justified by the fact that we consider temperatures well below melting, and in a bulk system the 4-fold coordination is retained.

4.2.2 **Surface investigation**

When interested in exploring surface properties we consider a slab geometry with periodic boundary conditions (PBC) parallel to the surface (Figure 4.2). As a consequence, each sample provides two surfaces to be studied at one time. This geometry has the advantage of not arbitrarily forcing any atom into bulk positions, while a concern is that the two surfaces may not be completely independent if the sample is not thick enough to have bulk-like behavior towards the center. Because it is convenient to consider systems that are as small as possible, preparatory work was done to determine the minimum usable thickness for such a slab. 24 atomic layers were found to be sufficient for our purposes (L_z=6) (details on these calculations are discussed in Chapter 5). 22x22, 28x28 and 34x34 are typical surface sizes for which results are presented in this dissertation. Our interest here is mainly on the

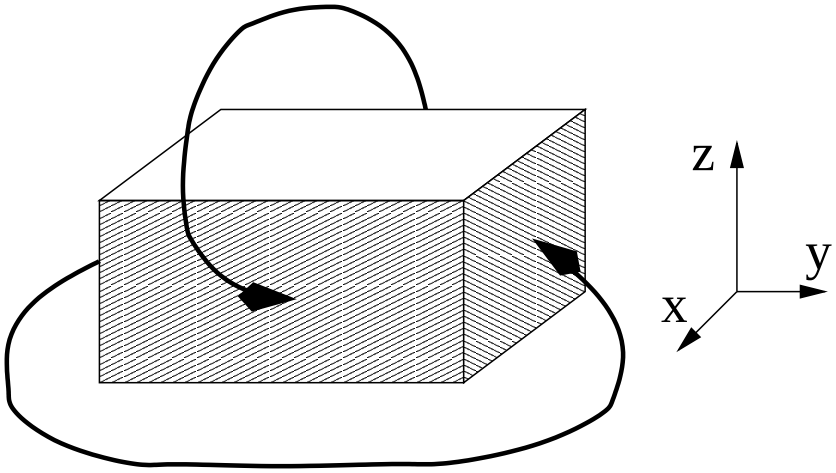

Figure 4.2: Slab geometry. The arrows indicate the directions along which PBC are applied.

development of the algorithm, more than on the accurate determination of physical properties, so that the system sizes used during these simulations do not represent the largest ones treatable with this method but only those that can be studied in a relatively short amount of time.

As seen in Chapter 2, the main feature of the Si(001) surface is the dimer reconstruction. In order to respect the intrinsic geometry of the problem as much as possible, our simulation cell is constructed along the [110][1$\bar{1}$0] and [001] directions and consists of a $L_x \times L_y \times L_z$ repetition of the cell shown in Figure 4.3, both for the reconstructed and unreconstructed case. Both cases have been used as starting point in our simulations. Such a cell contains $N=4 \times L_x \times L_y \times L_z$ atoms; we always considered $L_x = L_y$.

All our simulations concerning surface studies have been performed in the canonical ensemble, i.e. keeping temperature and number of particles constant. Moreover, in these simulations the pressure, and not the volume, was kept constant (P=0)

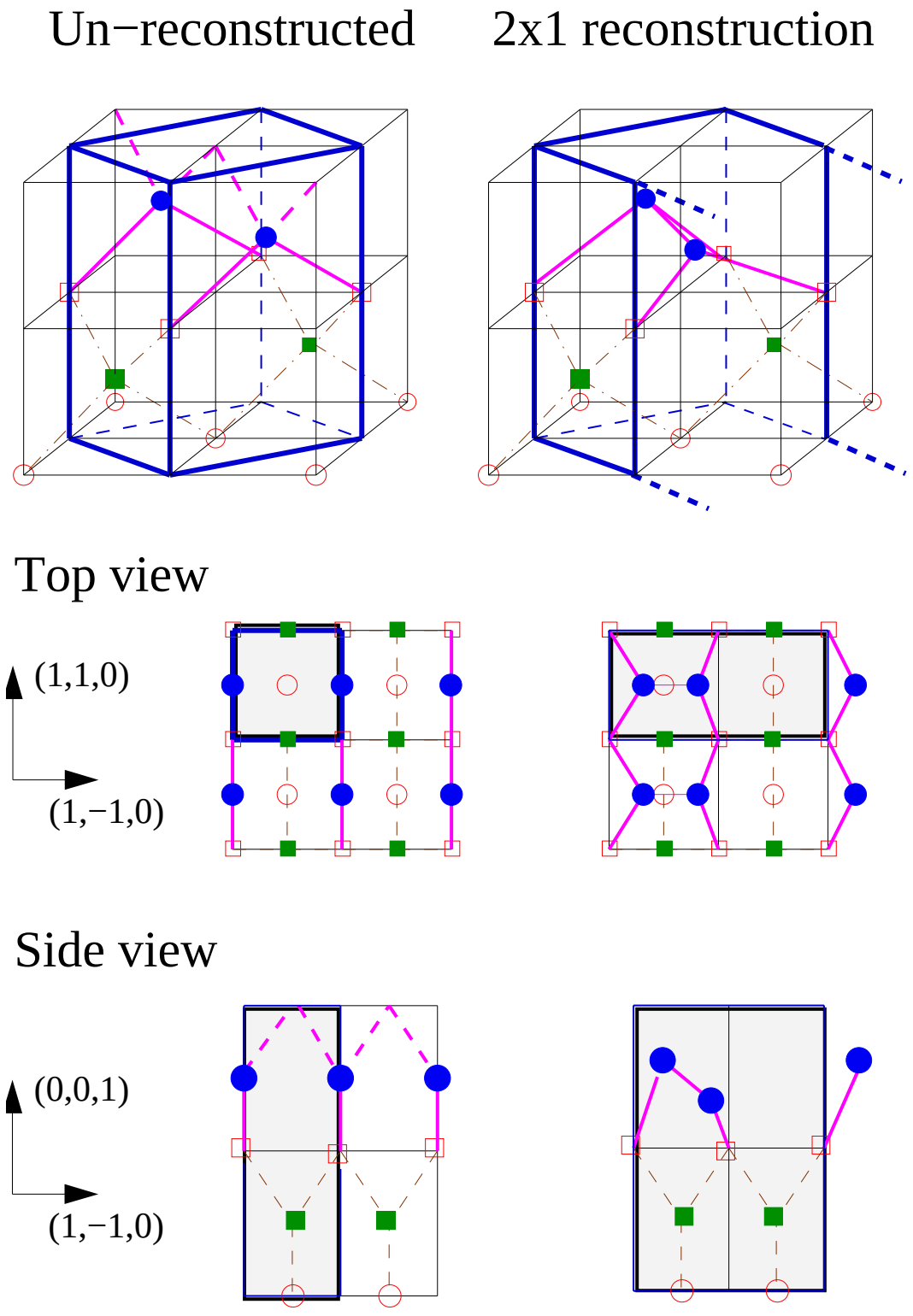

Figure 4.3: Simulation cell for surface problems. The atoms are shaped-coded versus depth. The cell indicated be thicker lines inside the standard diamond conventional cell and is shaded gray in the top and side view. nn bonds are indicated (the line is dashed for dangling bonds).

because this is the most common experimental condition. In order to maintain constant pressure, the volume was varied during the simulation by randomly changing each cell side independently by a small amount. Lastly, all these simulations were performed off-lattice, i.e. each atom could move everywhere in space and the diamond structure wasn't necessarily preserved. This flexibility, for example, allowed us to test the efficacy of the potentials by starting from unreconstructed configurations and checking what kind of reconstruction was obtained at the end of the simulation (Chapter 5). An unfortunate consequence of this flexibility is that the Verlet list must be recalculated quite often, especially if the physics suggests that the lattice structure is easily changed (as in the case of initial un-reconstructed surfaces). More about this is discussed in Section 4.7.1.

Summarizing, in these standard Monte Carlo simulations at first the atoms attempt to move, one by one. This kind of trial move is referred to as *single-atom* move in the rest of this dissertation, to distinguish it from more involved ones that will be introduced in the next chapter. Once that all the atoms have tried to move and the volume variation is attempted, we say that one MC step (MCs) has passed.

4.3 Metropolis algorithm

The way that we chose to perform importance sampling MC is to use the Metropolis algorithm [77]. In this case we generate configurations from a previous state using a transition rate W_{mn} which depends only on the energy difference between initial and final state ($\Delta E = E_{fin} - E_{in}$). The sequence of states that are produced using this algorithm follows a time ordered path, but this "time" is not-deterministic. It is usually referred to as "MC time".

The explicit form of the Metropolis transition rate is the following:

$$W_{mn}^{Metr} = \begin{cases} \tau_0 \exp(-\Delta E/KT) & \text{if } \Delta E > 0 \\ \tau_0 & \text{if } \Delta E < 0 \end{cases} \tag{4.14}$$

where τ_0 is the time required to attempt a move. Often this "time unit" is set equal to unity and hence suppressed in the equations. Remembering that the Boltzmann probability distribution P_{eq} for the state S_n has the form:

$$P_{eq}(S_n) = \frac{\exp(-E_s/KT)}{Z} \qquad Z\text{=partition function} \tag{4.15}$$

it is immediate to see that W_{mn}^{Metr} satisfies detailed balance

$$W_{mn} P_{eq}(S_m) = W_{nm} P_{eq}(S_n) \tag{4.16}$$

In the Metropolis algorithm every time a move is attempted, the transition probability between the old and the new state is given by Eq. 4.14 and the move is accepted if W_{mn}^{Metr} is bigger that a random number generated uniformly between 0 and 1 [78].

In those simulations where the volume is allowed to change, the energy change $\Delta\mathcal{H}$ associated with the global distortion of the system is not the only quantity entering the Metropolis acceptance criterion. In addition, the term

$$\Delta\mathcal{H}_{eff} = \Delta\mathcal{H} - N k_B T \ln\left(\frac{Ł'_x Ł'_y Ł'_z}{Ł_x Ł_y Ł_z}\right) \tag{4.17}$$

has to be considered as well, representing the change in translational entropy when the volume changes. $Ł_i, Ł'_i$, i=x,y,z are the old and new cell sides along the x, y and z directions.

4.4 Hysteresis calculations and thermodynamical integration

To determine the phase diagram in the ($\Delta\mu$,T) plane different techniques were used, depending on the values of T under consideration. In the low temperature regime

hysteresis calculations and free energy integrations were performed to determine the transition $\Delta\mu$ and the corresponding coexistence values of c_{Ge} (details below), while the high T regime was analyzed using parallel-tempering (PT) [84–86] simulations (Section 4.6) together with histogram reweighting [80, 81] (Section 4.5).

Hysteresis loops in the Si and Ge equilibrium concentrations were obtained by sweeping through the chemical potential difference $\Delta\mu = (\mu_{Ge} - \mu_{Si})$ in both directions at fixed temperature. In each case we started in the complete Si (or Ge) regime and first increased (or decreased) $\Delta\mu$, then swept it back to its initial value. During these runs each simulation started from the end of the previous one and was 10^5 MC steps long. Examples of hysteresis loops are presented in Chapter 7.

When studying hysteresis loops obtained at low $\Delta\mu$ and low T, we determined the coexistence values of c_{Ge} and the transition $\Delta\mu$ from direct inspection of the hysteresis loops itself, because of its small width and symmetry. On the contrary, for high $\Delta\mu$ and low T the loop is strongly asymmetric so that we considered necessary to evaluated the same quantities more carefully. To do so we used the "free energy crossing" method.

In this technique [64, 78] the branches of the free energy (F) are obtained integrating the relation

$$\frac{\partial F}{\partial \mu_B} = -\langle N_B \rangle \tag{4.18}$$

in both phases (B indicates one of the two atomic species under consideration). Naturally, this intersection method requires the knowledge of the difference in free energy $\Delta F = F_B - F_A$ between the end points deep in each phase. Such a difference can be estimated using thermodynamic integration, i.e. integrating Equation 4.18 and Equation

$$\frac{\partial}{\partial T}\left(\frac{F}{T}\right) = -\frac{U}{T^2} \tag{4.19}$$

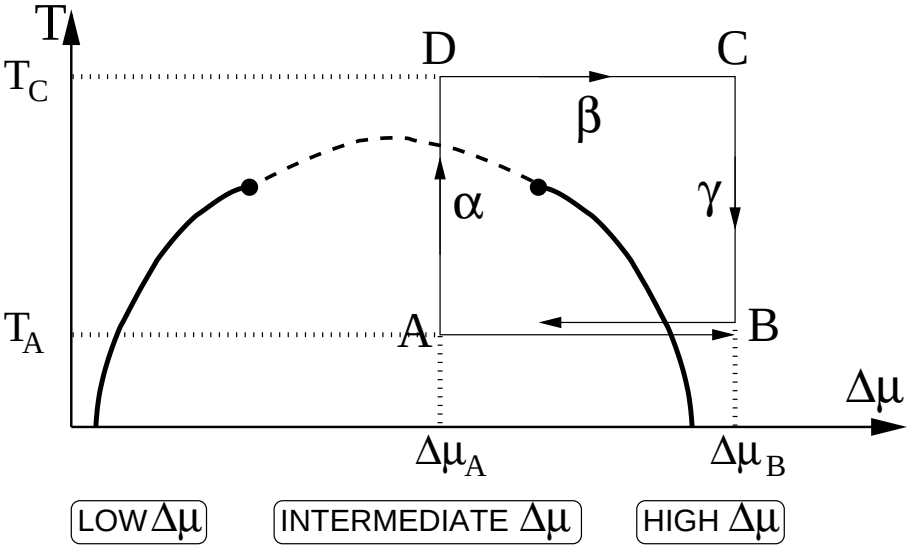

Figure 4.4: Loop ABCD: example of loop for thermodynamic integration. The thick solid lines represent first order lines ending in critical points (solid circle at the end of each line). The dashed line represents a region where properties might change rapidly but there is no hysteresis. In our case the dashed line represents a weak 1^{st} order transition and the solid and dashed lines together schematically represent our finding for the phase diagram.

(U=$\langle\mathcal{H}\rangle$ being the internal energy) over such a loop as shown in Figure 4.4 using the fact that each side of the loop is deep enough in one phase or sufficiently high in temperature that integration along paths AD, DC and CB encounters no discontinuities. This method is therefore effective independently of what is at the end of the first order line (i.e. along the dashed line in Figure 4.4) as long as the integral along AD is continuous. More specifically Equations 4.19 and 4.18 are rewritten as

$$\frac{F(T_1)}{NT_1} - \frac{F(T_0)}{NT_0} = -\int_{T_0}^{T_1} \frac{U/N}{T^2}\, dT \qquad \text{for } \Delta\mu\text{=const} \tag{4.20}$$

$$\frac{F(\Delta\mu_2)}{N} - \frac{F(\Delta\mu_1)}{N} = -\int_{\Delta\mu_1}^{\Delta\mu_2} c_{Ge}\, d\Delta\mu \qquad \text{for T=const} \tag{4.21}$$

where $c_{Ge} = \langle N_B \rangle$/N, the "B" species in Equation 4.18 is assumed to be Ge and N=total number of particles. Because of Equation 4.13, it is identical to sweep in $\Delta\mu$ or in μ_{Ge}, if μ_{Si} is kept fixed. Next, these equations are applied to the branches α, β and γ of the loop ABCD and ΔF is finally determined as

$$\begin{aligned} \frac{(F(B) - F(A))}{N} &= \frac{\Delta F}{N} = \\ &= -T_A \int_{T_A}^{T_C} \frac{U(\Delta\mu_A, T)/N}{T^2}\, dT - \frac{T_A}{T_C} \int_{\Delta\mu_A}^{\Delta\mu_B} c_{Ge}\, d\Delta\mu \\ &\quad -T_A \int_{T_C}^{T_A} \frac{U(\Delta\mu_B, T)/N}{T^2}\, dT \end{aligned} \tag{4.22}$$

All the integrals in Equation 4.22 can be easily calculated once that data are taken on the appropriate loop branch.

As discussed more thoroughly in Chapter 7, our final finding for the phase diagram consists in one single first order line in the (μ,T) plane (as schematically shown in Figure 4.4 considering the solid and dashed lines together). Therefore, any choice of point A in the intermediate c_{Ge} regime necessarily corresponds to a crossing of the first order line (dashed line in Figure 4.4). This, though, was not a problem in our calculations because it was found that the first order transition weakens going toward higher T and we encountered no observable discontinuity when integrating Equation 4.19 along the AD path for a choice of μ_A=1.45 eV (i.e. $\Delta\mu$=0.45 eV) and a 6x6x6 system.

4.5 **Histogram reweighting**

The basic idea of the histogram reweighting technique is to use data collected at one point in the parameter space to estimate physical quantities at different point in the same parameter space [79–82]. This method was first developed to study the Ising model in a magnetic field [79]. In that case the Hamiltonian can be written as

$$-\beta\mathcal{H} = K \sum_{i,j} \sigma_i \sigma_j + h \sum_i \sigma_i = KS + hM \tag{4.23}$$

where K is the dimensionless coupling constant (J/k_BT), h the dimensionless external magnetic field, M the magnetization and σ_i the value of the spin at site i. In the same formalism the probability distribution of S and M at a point in the parameter space (K,h) is given by

$$P_{(K,h)}(S,M) = \frac{1}{Z(K,h)} W(S,M) \exp(KS + hM) \tag{4.24}$$

where W(S,M) is the density of states (DOS) at the point (S,M) in the phase space and $Z(K,h)$ the canonical partition function

$$Z(K,h) = \sum_{S,M} W(S,M) \exp(KS + hM) \tag{4.25}$$

Using the fact that the DOS is independent of (K,h), it is easy to show that probability distributions at different values of (K,h) are related by

$$P_{(K',h')}(S,M) = \frac{P_{(k,h)}(S,M) \exp[(K'-K)S + (h'-h)M]}{\sum_{S,M} P_{(k,h)}(S,M) \exp[(K'-K)S + (h'-h)M]} \tag{4.26}$$

where $P_{(K,h)}(S,M)$ is given by Equation 4.24. Remembering that the histogram of values of (S,M) ($H_{(k,h)}$(S,M)) generated by a MC simulation is proportional to $P_{(K,h)}(S,M)$, Equation 4.26 means that $P_{(K',h')}(S,M)$ can be estimated from $H_{(k,h)}$(S,M) without additional computations.

To apply this technique to the study of the Si-Ge phase diagram under constant volume conditions, we re-expressed our Hamiltonian (Equation 4.12) as

$$-\beta\mathcal{H} = \beta\Delta\mu N_{Ge} - \beta\mathcal{H}_{pot} = KS + hM \tag{4.27}$$

so that in our case the S,M,K and h in Equation 4.23 are given by

$$\begin{aligned} h &= \beta\Delta\mu \qquad M = N_{Ge} \\ K &= \beta \qquad S = -\mathcal{H}_{pot} = -\Delta\mu N_{Ge} - \mathcal{H} \end{aligned} \tag{4.28}$$

The energy of our system is therefore given by

$$E = -\frac{h}{K} M - S \tag{4.29}$$

To be precise, M as defined in Equation 4.28 is not exactly the magnetization of the system, but it is related to it by

$$\text{magnetization } \mathcal{M} = N - 2N_{Ge} = N - 2M \tag{4.30}$$

However, it is easy to see that $P_{(K,h)}(S, M) = P_{(K,h)}(S, \mathcal{M})$, so that in the following we'll indicate the quantity defined in Equation 4.28 as magnetization, for simplicity and because it has a more immediate physical interpretation.

In our study we utilized this method together with parallel tempering, which will be discussed in Section 4.6, to accurately determine the location of the phase transition. Once that good histograms of S, M and E were collected (see Section 4.6), we used reweighting to compute quantities such as the specific heat (c_v), the susceptibility (χ) and the fourth order cumulant in energy (E4) or magnetization (M4) whose maximum indicates the location of the transition. Note that in these calculation we used the complete form of the fourth order cumulant

$$U_4 = 1 - \frac{\langle (A - \langle A \rangle)^4 \rangle}{3 \langle (A - \langle A \rangle)^2 \rangle^2} \qquad A = E, M \tag{4.31}$$

instead of the reduced form, because $\langle A \rangle \neq 0$.

As an example, in the following we show how to calculate the specific heat using histogram reweighting. From fluctuation theory the specific heat can be expressed as

$$\frac{c_v}{k_B N} = \frac{N}{(k_B T)^2} \left[\langle \left(\frac{E}{N} \right)^2 \rangle - \langle \frac{E}{N} \rangle^2 \right] \tag{4.32}$$

Defining the reduced quantities $c_v^* = c_v / k_B N$, $T^* = k_B T$, $E^* = E/N$, $M^* = M/N$ and $S^* = S/N$ as used in the simulations, and remembering that

$$\langle A \rangle = \sum_A P(A)\, A \tag{4.33}$$

we can rewrite the specific heat as

$$c_v(K, h) \;=\; NK^2 \left\{ \left[\sum_{S,M} P_{(K,h)}(S, M) \left(-\frac{h}{K} M^* - S^* \right)^2 \right] - \right.$$

$$\left[\sum_{S,M} P_{(K,h)}(S,M)\left(-\frac{h}{K}M^* - S^*\right)\right]^2\Bigg\} \tag{4.34}$$

Having taken data at (K,h), we can therefore obtain c_v at any point (K′,h′) of the phase space simply using Equation 4.34 and expressing $P_{(K',h')}(S,M)$ in terms of $P_{(K,h)}(S,M)$ using Equation 4.26.

When using reweighting, it is crucial to guarantee that the "initial" (i.e. measured) histogram corresponds to the correct distribution of the analyzed quantity. In order to collect good statistics very long runs (on the order of 10^6 MCs) must be performed, but sometimes this is not enough. As it will be discussed more in detail in Chapter 7, in our case, it was rarely possible to sample both states across the transition line during a single run, even when running simulations with more that 5 $\times 10^6$ MCS. Parallel tempering had therefore to be used to collect good initial histograms.

A limitation of reweighting is that it is effective only for points (K′,h′) not too far from the point (K,h) where data are collected. This restriction is a consequence of the fact that MC runs are finite: not many data are collected toward the "wings" of the measured histogram, and if (K′,h′) is too far from (K,h), the peak of its distribution ends up in the part of the spectrum where the statistical error is high. The maximum distance between (K′,h′) and (K,h) depends on the problem under examination and on the system size used in the calculations. An example of reweighting in temperature is shown in Figure 4.5 for our problem and a test-system of 512 atoms. The ($\Delta\mu$,T) used are above the transition line, so that collecting a good initial histogram was straightforward. The measured histogram is collected at T_0=0.0043 eV, and $\Delta\mu$ is 0.472 eV in all runs. It is easy to notice how much the quality of the histograms generated by reweighting decreases as the temperature moves away from T_0.

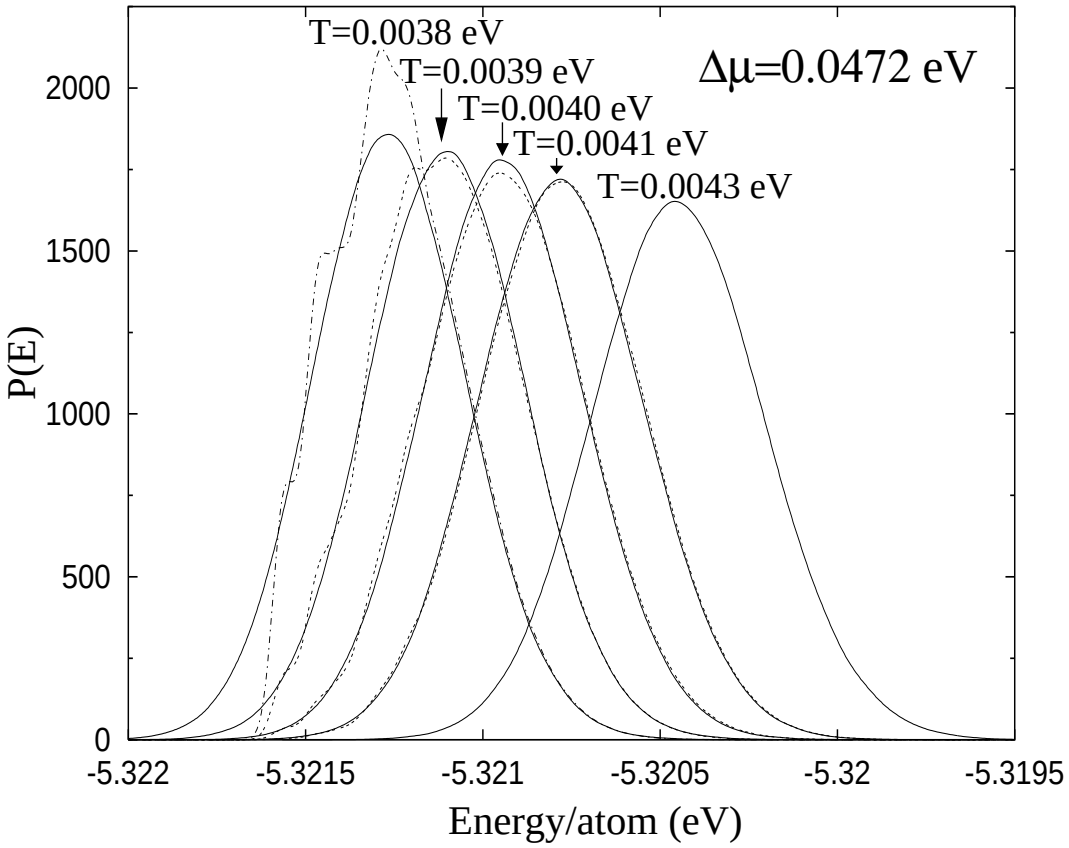

Figure 4.5: Histogram reweighting in temperature for energy (E): solid lines correspond to the measured histograms (i.e. to simulations ran at the temperatures shown above the curves and 2×10^6 MCs long), dashed lines to histograms obtained by reweighting data taken at k_BT=0.0043 eV to different T. $\Delta\mu$=0.472 eV in all cases.

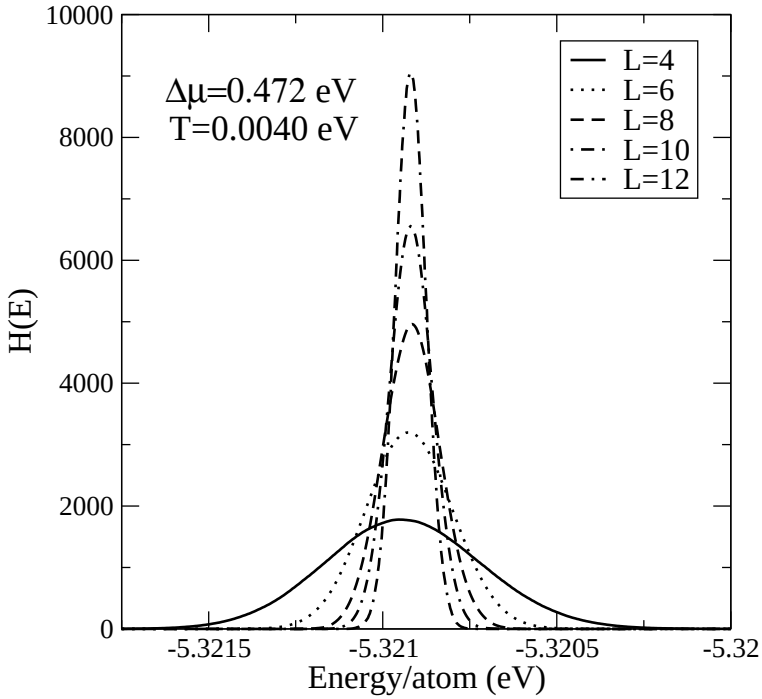

Figure 4.6: Histograms collected at $\Delta\mu$=0.472 eV, k_BT=0.0040 eV for different system sizes.

Lastly, note that the width of the histograms decreases as the size of the system used in the simulation increases (Figure 4.6). This obviously means that the larger the system used, the closer (K′,h′) must be the initial (K,h).

4.6 **Parallel tempering**

One of the problems that most frequently occurs in MC simulations is becoming trapped in some metastable state. If such a state is very stable, as it is the case for metastable states that require collective changes in the atomic configuration to be eliminated, the trapping may last several millions MCs. A technique developed to help free the system is the Replica Monte Carlo, or Parallel Tempering. The idea is to simulate *simultaneously* and *independently* several replicas of the same system, each

at a different temperature, but every so often configurations between neighboring replicas are exchanged [83–86].

Let's consider M non-interacting replicas of the system under investigation. The m-th replica, described by a usual Hamiltonian $\mathcal{H}$ is associated with a temperature T_m (β_m). For convenience let's consider $\beta_m < \beta_{m+1}$. In constructing a Markov process we introduce a transition matrix $W(X, \beta_m | X', \beta_n)$ which gives the probability of exchanging configurations between the n-th and the m-th replicas (X indicate a state in the extended ensemble: $\{\mathrm{X}\}=\{\mathrm{X}_1,\mathrm{X}_2, \ldots \mathrm{X}_m\}$). For the system to remain in equilibrium, it is sufficient to impose that detailed balance (DB) is satisfied by the transition matrix:

$$\begin{aligned} P(...;X,\beta_m;.....;X',\beta_n;....)\ \ W(X,\beta_m|X',\beta_n) \\ = P(...;X',\beta_m;.....;X,\beta_n;....)\ \ W(X',\beta_m|X,\beta_n) \end{aligned} \tag{4.35}$$

Adopting the Metropolis algorithm, the transition rate W that we used to decide if we accept the configuration exchange is simply

$$W(X,\beta_m|X',\beta_n) = \begin{cases} \exp(-\Delta) & \text{if } \Delta > 0 \\ 1 & \text{if } \Delta < 0 \end{cases} \tag{4.36}$$

where

$$\Delta = (\beta_n - \beta_m)(\mathcal{H}(X) - \mathcal{H}(X')) \tag{4.37}$$

It has been proven [83,84] that the acceptance rate for the configuration exchange decreases exponentially with the difference $\beta_m - \beta_n$, so that it is usually convenient to restrict the replica-exchange to the case n=m+1 (nearest *neighbor* replicas). We adopted this restriction in all our simulations.

As seen in Section 4.5, the width of the histograms depends on the system size used in the simulations. In terms of parallel tempering, this means that temperatures closer to each other must be considered as the size of the system under investigation is increased, because the overlap between energy-histograms is reduced.

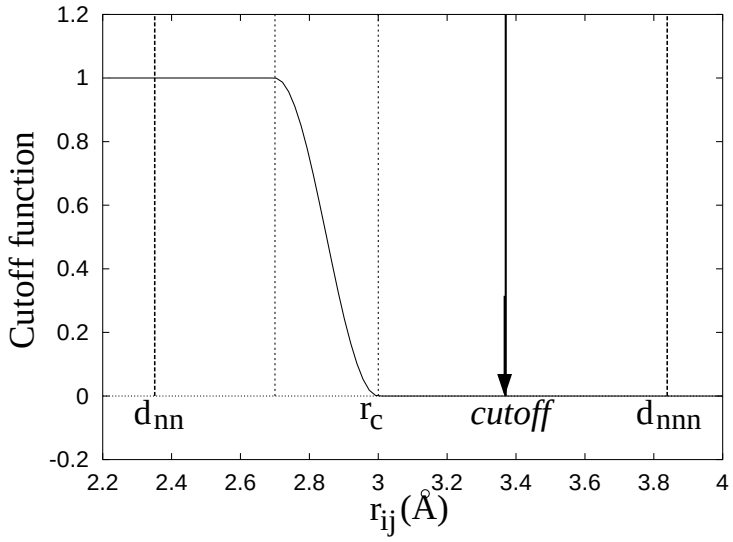

Figure 4.7: Cutoff function for the potential and skin distance for Si on a diamond lattice at T=0 K.

4.7 Techniques to speed up the simulations

One important difference between the simulations performed when studying the bulk phase diagram and those performed to analyze surface properties is that the former are conducted *semi-on-lattice* while the latter are not. As discussed in Section 4.2, this implies that the nearest-neighbor list (Verlet list) must be often recalculated in the latter case and this, for a large system, is rather expensive computationally. As a result, computing 1 MCs when studying the surface takes a much longer time that in the bulk, for similar system sizes. It was therefore important to find ways to accelerate the simulations when dealing with surface calculations.

In Section 4.7.1 two standard techniques used to speed up calculations are reviewed: the introduction of a *skin distance* and the performance of non-uniform sampling on the system. In Section 4.7.2 a different approach is discussed: the

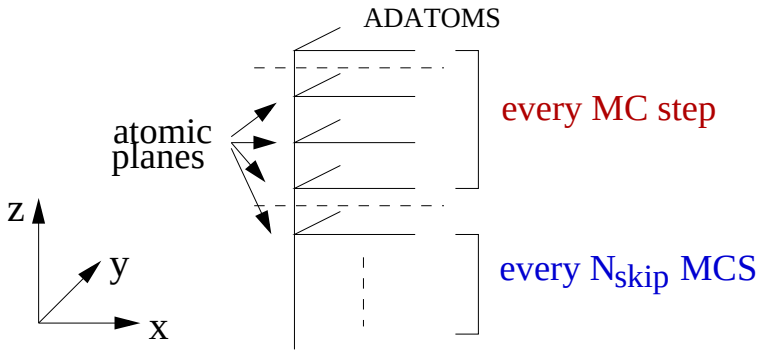

Figure 4.8: Non-uniform sampling: the atomic planes closer to the surface are sampled more often than those toward the center of the slab.

parallelization of the code. As long as only *single-atom* moves were utilized, these approaches were implemented together in the simulation code.

4.7.1 Preferential sampling and "skin" distance

The idea at the basis of the use of a *skin distance* is depicted in Figure 4.7. Classical potentials are designed such that the interatomic interactions go to zero smoothly at a certain distance r_c in order to include only a limited number of interactions in the calculations. The potentials that we utilize only consider "nn" interactions, so $d_{nn} < r_c < d_{nnn}$, where d_{nn}=nn and d_{nnn}= next-nearest neighbor (nnn) distances in the perfect lattice at zero temperature. At finite temperature we have a distribution of nn and nnn distances and each MC step atoms whose distance before was just above r_c may now be close enough to contribute to the potential, and vice-versa. If we record in our "neighbor" list only those atoms that do contribute to the potential, then we necessarily must recompile such a list after every step. If, on the other side, we include in the list all the atoms whose distance is less that $r_c + 2 \times n \times displ_{max}$, where $displ_{max}$ is the maximum displacement allowed to each atom in one MC step, then

we can safely recompute the Verlet list every n steps. The distance $2 \times n \times displ_{max}$ is referred to as *skin distance* and must be determined balancing the advantage of reducing the frequency of recalculation of the nn list with the increase in memory and computational time due to having a larger number of interactions to compute and store.

An even simpler idea stands behind the non-uniform (preferential) sampling. We expect that the great majority of the events will take place on the surface and that deeper inside the sample fewer atomic rearrangement will occur with respect to the initial diamond structure. Because of that, we attempt to move atoms within k layers from the surface every MCs, and atoms deeper in the bulk only every N_{skip} MCs (Figure 4.8). The actual values of k and N_{skip} must be determined case by case making sure that results obtained using the preferential sampling are identical to those obtained without it. In our case, for example, k=5 and N_{skip} can be as big as 10.

4.7.2 **Code parallelization**

In the following we describe the parallelization scheme employed for the surface study when only *single-atom* moves and volume variations are utilized. Parallelization doesn't reduce the total CPU time needed to perform a simulation, but shortens the waiting time for the results very effectively by dividing the work load among several processes. In general, multiple processes can be run on one processor, but the most efficient way to use parallelization is to run each process to a different processor. This is how we did it, and in the following the terms *process* and *processor* will be used interchangeably. The efficiency of this method increases dramatically with the size of the system under investigation, to the point that parallelization becomes the only possible approach when very large systems are analyzed. Compared to simulations performed on single processes the usage of parallelization increases the total

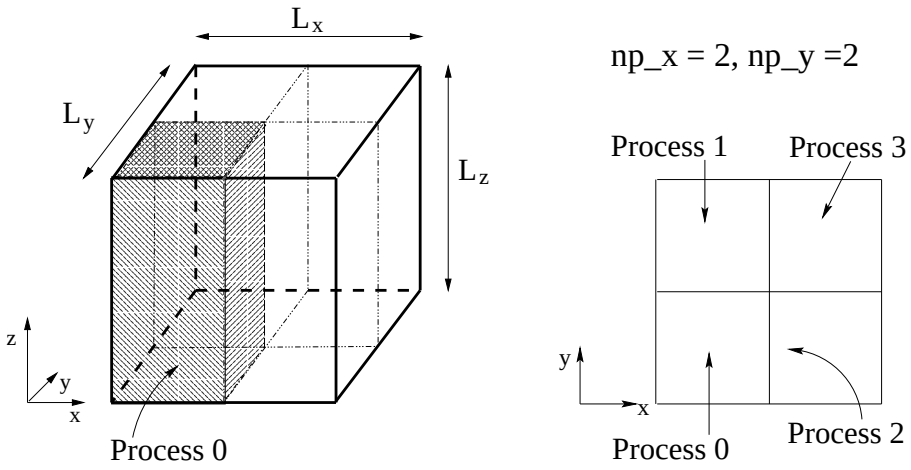

Figure 4.9: Example of 2D decomposition with 4 processes.

amount of computations because the processes need to communicate with each other. To increase the efficiency of a code it is extremely important to minimize communications, and in the following we discuss how communications are organized in our code.

The initial step in writing a parallel program is deciding what kind of decomposition to use. In Section 4.2.2 we pointed out our interest in simulating surfaces that are as large as possible, and we proved that a slab 6 cells thick is sufficient to guarantee independent evolution of the surfaces. Because of all of this we decided to use a 2D decomposition (Figure 4.9) even if our system is tridimensional. Given a L_x x L_y x L_z system, each process is therefore assigned a $\frac{L_x}{np\_x}$ x $\frac{L_y}{np\_y}$ x L_z subsystem to deal with, where np_x(y) = number of precesses along x (y).

Identification of neighbor processes

Each process needs to send and receive data from its neighbors. The first step in doing so is to identify them. This is accomplished in the function *startMPI* through

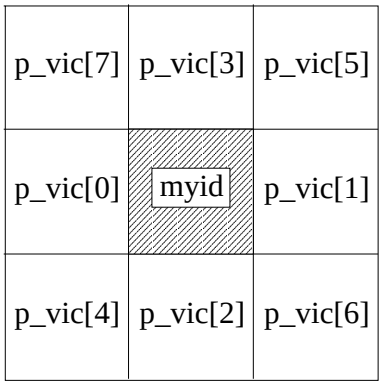

Figure 4.10: Neighbor processes for process "myid".

the vector *p_vic*. For each process, p_vic[0] contains the name of the neighbor process on the left, p_vic[1] of that on the right, p_vic[2] of that below, p_vic[3] of that above, and so on, as shown in Figure 4.10.

The 2D decomposition considered in the program has periodic boundary conditions (PBC), so that every process has the same number of neighbors. As a consequence, this code requires at least 4 processes to run, two along x and two along y, otherwise each process tries to communicate with itself.

Regions

To parallelize calculations, all the processes must be allowed to attempt to move their particles at the same time. To decide if a particle moves, it is necessary to calculate the energy change corresponding to such a move, and the upgraded positions of all the particles nearest and next-nearest neighbors to the one under examination are needed.

If the processes move all their particles before communicating with each other, problems occur for those particles that are in one process but have neighbors in

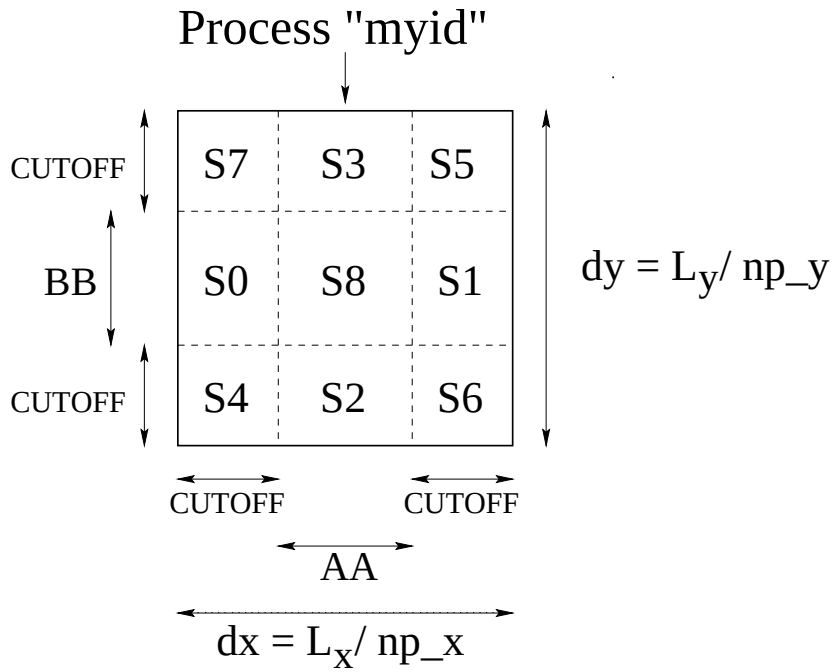

Figure 4.11: Regions inside process "myid" (AA, BB $\geq$ *CUTOFF*).

other processes, because once that such a particle i has been moved, its position is automatically upgraded in its own process but not in all the others. This means that, when one of its neighbors is moved in a different process, the old position of the particle i is used in the calculation instead of the new one.

Then, on one side we want all the processes to work contemporaneously, in order to get good parallelization, on the other it's not possible to simultaneously move particles that are in different processes but closer than a certain distance. Because both nearest and next-nearest neighbors are needed to calculate the energy, this distance, labeled *CUTOFF* in the code, is taken to be twice the distance that identifies nearest neighbors. This last distance is called "cutoff distance for the Verlet list" and is labeled *CUTOFF_V* in the code.

To solve this problem, the part of the system assigned to each process is divided into rectangular regions, as shown in Figure 4.11. These areas are numbered from 0 to 8, and are designed such that particles in one of them have no nearest or next-nearest neighbors in regions with the same name in other processes. This allows the simultaneous movement of particles inside areas with the same name. The code is therefore written such that all the processes move the atoms inside a region *S_k* at one time, then communicate with each other, then pass to region *S_k+1* and so on, until all the areas have been done.

Dividing each process into such regions not only results in good parallelization of the calculations, but also allows the identification of those particles with nearest and next-nearest neighbors belonging to their own process. All the atoms in region S8 have this property and it is advantageous to identify them because they can be excluded from any communication.

Particles contained in a process

Because of the need to use both nearest and next-nearest neighbors to calculate the energy with any of the potentials utilized, each process contains the particles that are in its part of the system (group A), plus all the particles contained in the neighbor processes within a distance *CUTOFF* from its border (shaded area in Figure 4.12, group B). The first second group of particles is known to the process since the beginning, while the second group is communicated to it in the function *scambio*.

Numbering of the particles

At the beginning of each run the positions of all the particles in the system are read from an outside file or are calculated in the function *diam*. At the same time a name

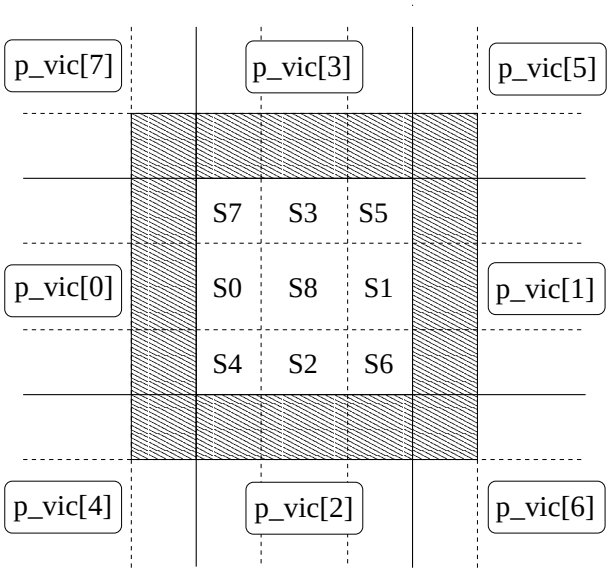

Figure 4.12: Particles contained in a process.

is assigned to each particle, and such a name is never changed during the simulation and is memorized in the vector *name*.

In order to greatly reduce the memory needed, each process also assigns a local name to its own particles, numbering them from 0 to *n_inproc*. Because of this, vectors used only inside a process have a much smaller size, the loops are much faster and so on. Obviously, a particle that is contained in more than one process has a different local name in each process.

When numbering the particles, the first ones to be counted are those of group A, then the others. The naming procedure for particles A takes place in the function *lista*, obeying the following rules:

- first those contained in region S8,
- then those in region S0,
- then those in region S1,

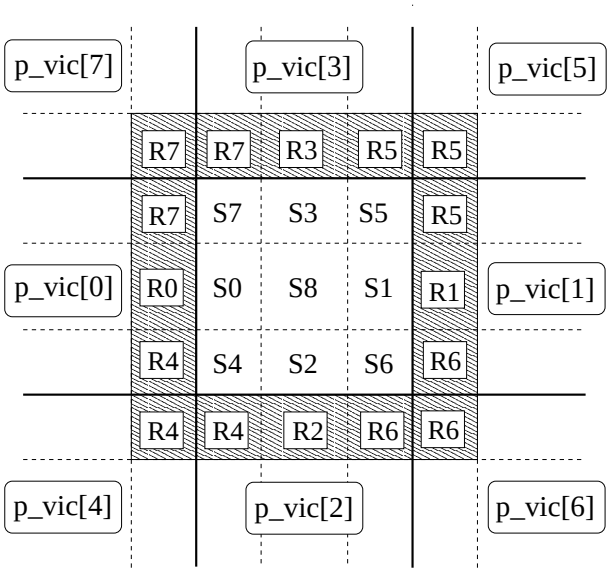

Figure 4.13: Strips and areas from which a process receives particles.

- .....
- finally those in region S7.

The total number of particles of group A is *npp* (number [of] particles [in the] process), and the number of particles in each region is *nump*[k], k=number of the region.

The particles of group B are added into the process in the function *scambio* and immediately given a name. Their total number is *nadd* (number [of particles] added), and their naming procedure obeys the following rules:

- first those received from area R0 (R0 = S1 in process p_vic[0]),
- then those received from area R1 (R1 = S0 in process p_vic[1]),
- .....
- finally those received from area R7.

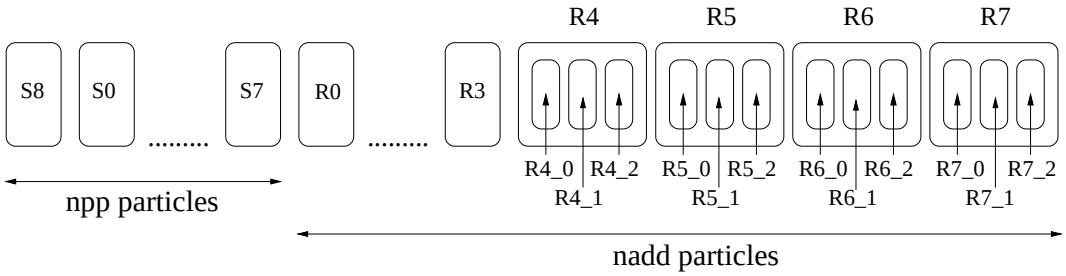

Figure 4.14: Numeration of the particles inside a process.

These areas Rs, together with the regions Ss are shown, for one process, in Figure 4.13. In Figure 4.14 we display how the particles are organized inside each process.

All of this can appear awfully complicated, but numbering the particles inside each process in this way is very important because it allows a quick updating of the positions. As seen before, the particles attempt to move region by region, and when all the atoms in an area have attempted a jump, their new positions are communicated from their process to the neighbor processes. The upgrading procedure in the neighbor processes becomes very fast if it is easy to identify the particles to modify, and this is what is accomplished through such a numbering.

Communications

Now that all the notations have been introduced, we summarize how communication processes are organized in the code. Simple broadcasts of data occur many times during the execution of the program, but massive processes of sending and receiving data take place only in four different moments:

1) at the very beginning, before the Monte Carlo cycle is started, when each process receives the particles of kind B to add to its own (function *scambio*);

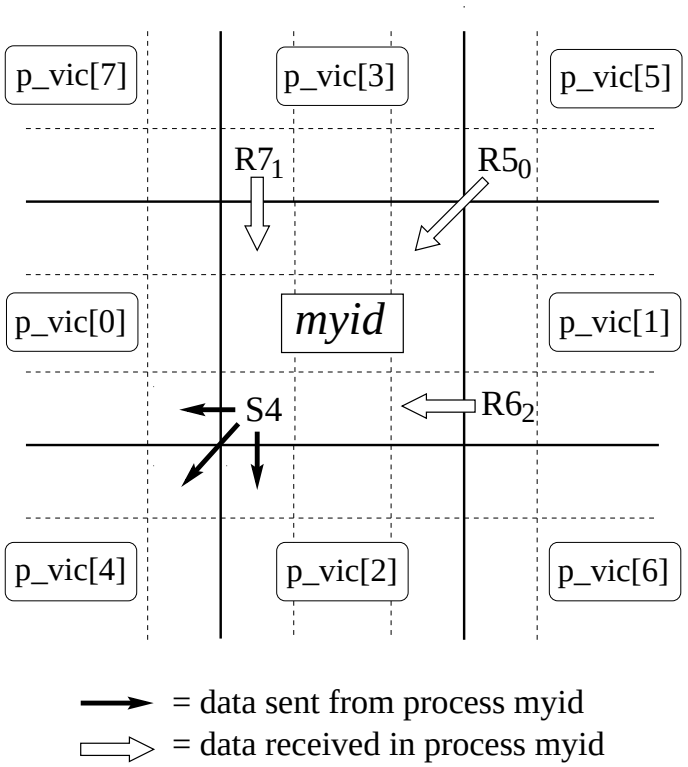

Figure 4.15: Communications after that all the particles in region k=4 have been moved.

2) during the Monte Carlo cycle, every time that all the particles in a region have attempted to move. In this case not only the positions of the particles are communicated, but also other quantities related to the calculation of the energy. These quantities are prepared to be sent in the function *prepara* and are communicated in the functions *comunica* and *aggiorna*;

3) at the end of one or more Monte Carlo steps, when we check if the particles have moved so much that they don't belong anymore to the process they are in. If this is the case, they are sent to the new process (function *scambio_in*);

4) after the execution of the function *scambio_in* each process contains different particles than before; the situation is therefore as it was at the beginning of the run and the function *scambio* has to be executed again.

To understand how these communication processes take place, let's consider a process (*myid*) that, having moved all the particles in a region *k*, communicates the new data to other processes. The same exact pattern is followed in the communications executed in *scambio* or *scambio_in*. As we know, all the processes move their particles in region k at the same time, so, while a process *myid* sends its data, it also receives data from another process, as shown in Figure 4.15 for the case of k=4. In Table 4.1 the way in which this send/receive data works for each region k is summarized. For areas S4, S5, S6 and S7, the names of the processes to send data to (column two in the table) or to receive data from (column four) are contained in the vectors *s_vic, r_vic*, respectively. These vectors are defined in the function *startMPI*. In the same function the list of storing addresses for the received data is also defined, and is called *r_ind* (column five in the table).

Strip moved (in myid)	Data sent		Data received	
	Process the data are sent to (with respect to myid)	Strip sent (in myid)	Process the data are received from (with respect to myid)	Storing place for the data (in myid)
S0	p_vic[0]	S0	p_vic[1]	R1
S1	p_vic[1]	S1	p_vic[0]	R0
S2	p_vic[2]	S2	p_vic[3]	R3
S3	p_vic[3]	S3	p_vic[2]	R2
S4	p_vic[4]	S4	p_vic[5]	$R5_0$
	p_vic[2]	S4	p_vic[3]	$R7_1$
	p_vic[0]	S4	p_vic[1]	$R6_2$
S5	p_vic[5]	S5	p_vic[4]	$R4_0$
	p_vic[3]	S5	p_vic[2]	$R6_1$
	p_vic[1]	S5	p_vic[0]	$R7_2$
S6	p_vic[6]	S6	p_vic[7]	$R7_0$
	p_vic[2]	S6	p_vic[3]	$R5_1$
	p_vic[1]	S6	p_vic[0]	$R4_2$
S7	p_vic[7]	S7	p_vic[6]	$R6_0$
	p_vic[3]	S7	p_vic[2]	$R4_1$
	p_vic[0]	S7	p_vic[1]	$R5_2$

Table 4.1: Communications scheme.

Chapter 5

A new algorithm for studying semiconductor surfaces

In this and in the following chapter we present results obtained when studying the Si(001) surface. We first show that the use of the standard MC approach introduced in Chapter 4 is unsatisfactory when simulating phenomena involving simultaneous motion of several particles, as it is the case for surface reconstructions or island evolution. The need for a more involved algorithm that contains the possibility of collective moves is therefore introduced. The development of such an algorithm is the subject of the second part of this chapter. Finally, results obtained using this original algorithm are presented in Chapter 6.

5.1 Single-atom moves only: results

Before starting the actual study of the Si(001) surface evolution, it was important to perform preparatory calculations to determine simulation parameters like the minimum slab thickness (Section 4.2.2) or the depth and frequency for the non-uniform sampling (Section 4.7.1). Moreover, whenever simulations are performed using empirical potentials, it is a safe habit to evaluate their capability by reproducing already known quantities before applying them to the study of unknown phenomena. This is particularly true when, as in our case, potentials whose parameters have been fitted only on bulk properties are used to reproduce surface behavior. Several comparative studies of potentials for Si and Si-Ge systems are present in the literature [89–91],

but none of them is exhaustive on the topic of surface studies. In the following these preparatory results are presented.

5.1.1 Determination of slab minimum thickness

The most important parameter to determine before starting the "real" simulations is the minimum thickness necessary to insure independent evolution of the surfaces in the simulational cell. This evaluation is performed by simulating slabs of different thickness and comparing results. In all these simulations the atoms initially sit on the nodes of a perfect diamond network everywhere but on the surfaces where, on the contrary, (2x1) symmetric reconstruction is present. The system relaxes for about 2×10^4 MCs, then data are taken for about 8×10^4 MCs.

In Figure 5.1 results are shown for nn distances, nn angles and atomic plane energies. This quantities are plotted versus the atomic plane number for three slab thickness (L_z=4, 6 and 8), so that one can immediately see that results for L_z=6 and 8 coincide within the errorbars, while L_z=4 is too thin. From these and other similar data we decided that 24 atomic planes (i.e. L_z=6) is enough to insure independent surface evolution. Such a conclusion is correct only in the limits of being interested in identifying general trends of surface behavior (as it is our case), not when evaluating physical quantities with great accuracy. If, for example, we were interested in calculating energy differences between reconstructions with different numbers of vacancy lines (as done in [87]), much thicker slabs would be required. From the analysis of data like those in Figure 5.1 it appears that the presence of the surface significantly affects the structural quantities only within 5 atomic planes from the surface itself. Because of that, we decided to sample the first 5 layers from the surface every MCs, the others only every N_{skip} MCs (commonly used values of N_{skip} are 5 or 10). In Figure 5.2 an example of test results obtained when checking

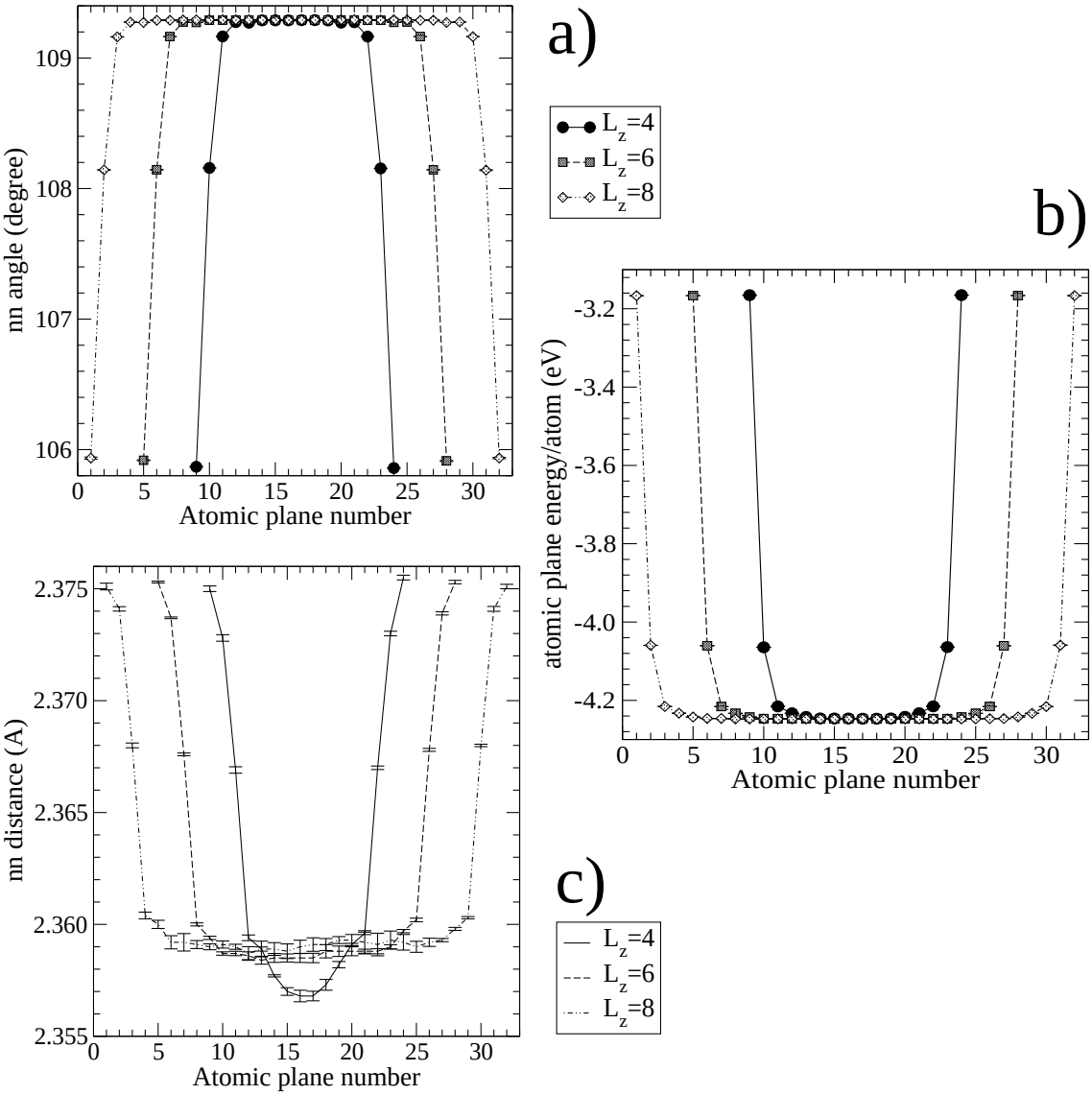

Figure 5.1: nn angles (a), atomic plane energies (b) and nn distances (excluding dimer bonds) (c) versus atomic plane (i.e. position inside the slab) for three slab thickness (L_z=4,6 and 8). Any time error bars are not shown, they are smaller than the symbols. T=0.06 eV, surface size 16x16, SW potential.

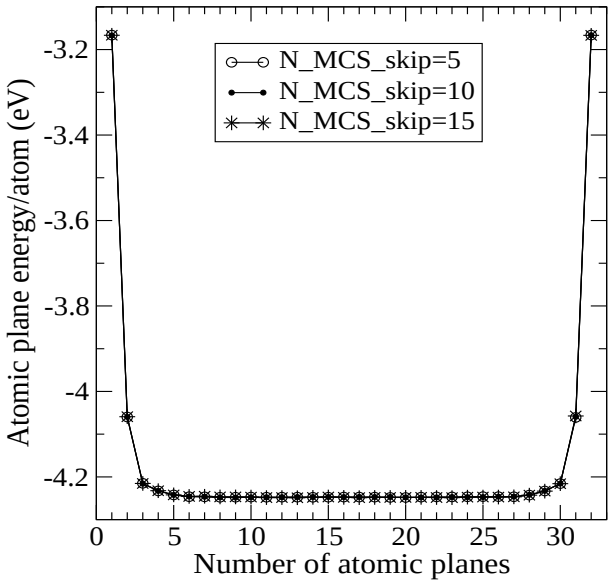

Figure 5.2: Atomic plane energy versus plane number for different values of N_{skip} (5, 10, and 15). The simulations were run using a 16x16x8 system and T=0.06 eV. Error bars are smaller that symbol size. SW potential.

this assumption are displayed. As can be seen, no noticeable difference is found when N_{skip} MCs is changed from 5 to 10 to 15.

Data such as those shown in Figure 5.1 allow some comparisons with experimental and *ab-initio* results, from which a first insight can be obtained on how accurate our potentials are in reproducing surface properties. In Figure 5.3 our findings using both SW and Tersoff potentials are compared to some experimental and theoretical results. No significant difference is found between the values estimated with SW and Tersoff: both potentials reproduce the correct trends for the quantities under examination (like having a smaller distance between the surface and the first atomic plane underneath it than between the first and the second plane). All our values are slightly larger than their experimental or *ab_initio* counterpart, which is consistent with having considered a much higher temperature in our simulations.

Dimer properties

Inter−atomic distances

Distance (Å)	(1)	(2)	(3)	SW	Tersoff
A−A	2.25	2.24	2.30	2.407	2.385
A−B	2.33			2.375	2.361

Distances between atomic planes

Distance (Å)	(4)	(5)	(6)	SW	Tersoff
sup−I plane	1.09	1.105	1.075	1.230	1.129
I−II plane	1.385	1.41	1.395	1.385	1.400
II−III plane	1.39	1.36	1.36	1.357	1.354

NN angles centered on a surface atom

Angle (deg)	(4)	(5)	(6)	SW	Tersoff
A−A−B	105.6	103.6	106.9	104.6	106.80
B−A−B				108.6	110.9

where: A = surface atom, B = bulk atom;
(1) = PRB 60, p. 1488, 1999: ab_initio, T=0;
(2) = PRB 51, p. 14504, 1995: ab_inito,T=0;
(3) = PRB 59, p. 7293, 1999: EXP, T=0.025 eV;
(4) = PRB 55, p. 4731, 1997: EXP, T=0.010 eV;
(5) = PRB 55, p. 4731, 1997: EXP, T=0.016 eV;
(6) = Appl. Surf. Sci. 56−58, p.15, 1992: ab_inito;
SW, Tersoff = our results, T=0.06 eV.

Figure 5.3: Surface properties estimated using *single-atom* moves and SW or Tersoff potentials. As a comparison results from the literature are shown as well. Error bars are on the first digit that is not shown.

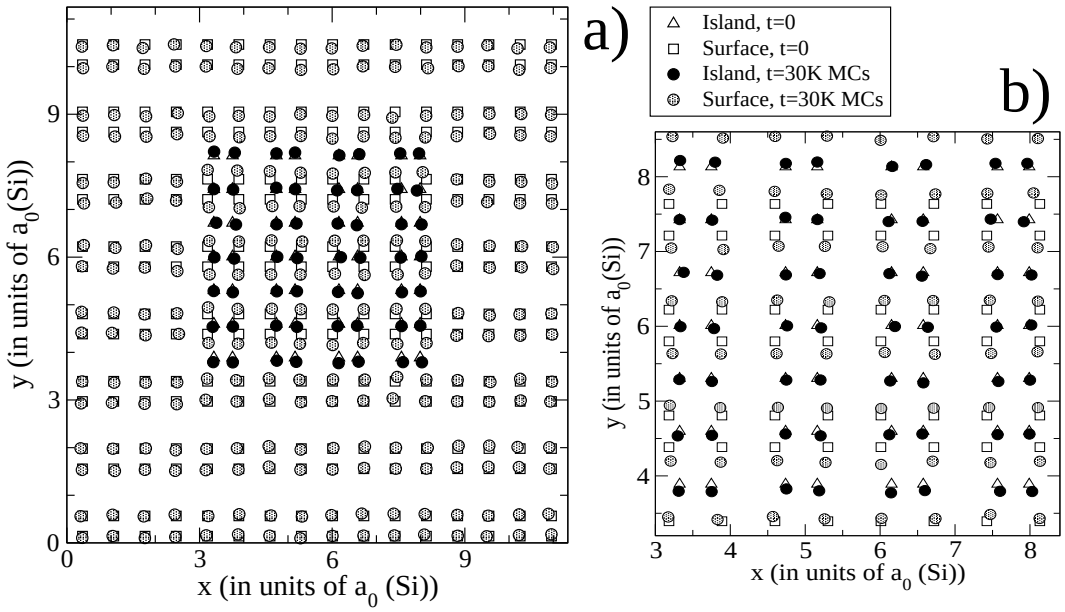

Figure 5.4: (a) Example of initial (open symbols) and final (solid and gray circles) configurations obtained when investigating what happens to a reconstructed surface when adatoms are deposited on top of it. The simulation temperature is T=0.06 eV, the final snapshot is taken after 3×10^4 MCs. The surface size is 16x16. (b) enlargement of the central part of (a).

5.1.2 **Reproduction of dimerization**

The details of the (2x1) dimerization on the Si(001) surface are well-known, so we can test the capability of the potential and method together to reproduce the correct physics. Such an analysis is done utilizing two sets of simulations: one to test if the dimerization disappears when adatoms are adsorbed on top of the surface, the other to verify if dimerization occurs when a clean surface is created.

To investigate what happens to a reconstructed surface when adatoms are deposited on it, we consider a silicon slab with (2x1)-reconstructed surfaces on top of which we deposit square islands. The islands present a (2x1) reconstruction as well, but in the direction perpendicular to that of the reconstruction on the

surface. Such a configuration is shown in Figure 5.4 by the open symbols (t=MC time=0). The system then evolves for some time at finite temperature (T=0.06 eV, for example). It usually only takes 1 or 2 $\times 10^4$ MCs for the dimers under the island to open up, as they should. Moreover, the atoms originally forming those dimers correctly move toward the ideal positions of a diamond lattice. This behavior is displayed in Figure 5.4, where the solid and gray circles indicate the positions of island and surface atoms, respectively, in a snapshot configuration taken after 3 $\times 10^4$ MCs. As expected, the atoms in the island or on the surface away from the island moved very little (they already were in energetically "convenient" positions), while those on the surface underneath the island moved significantly. To conclude, all the simulations run to test surface behavior in the presence of newly deposited adatoms were successful, i.e. produced results in agreement with experimental findings.

To determine if the method and the potential together are capable of generating the correct surface reconstruction, we ran simulations starting from a Si slab with perfect diamond lattice structure, i.e. with unreconstructed (001) surfaces, hoping to recover the expected (2x1) reconstruction. Temperatures typically used in these calculations are anywhere from 500 K to 1100 K. Contrary to what was found in the previously described series of tests, in this case all our simulations were unsuccessful, no matter how long they lasted or how high the temperature was.

Figure 5.5 shows a snapshot configuration obtained after 10^6 MCS at T=580 K as an example of what typically happens when we use only *single-atom* moves to perform these simulations. The open squares in the picture are the initial positions, corresponding to a perfect diamond lattice, and the solid circles are the positions after 10^6 MCS. As expected, many dimers have formed, but the number of undimerized atoms greatly exceeds what is experimentally measured at similar temperatures. Moreover, unphysical anti-phase domains have formed between the different islands (shown in Figure 5.5 by dashed lines). It is important to specify that all these fea-

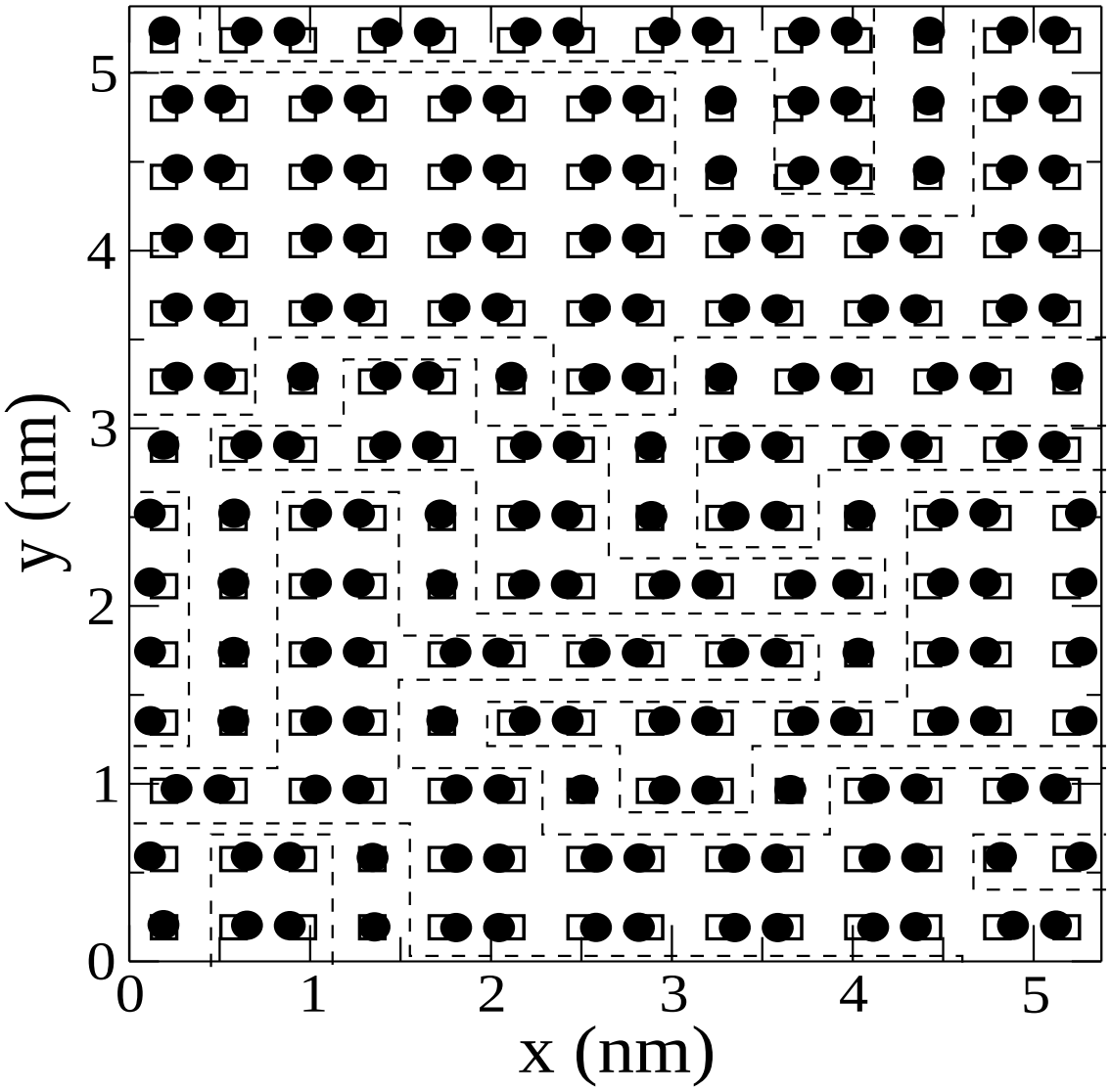

Figure 5.5: Snapshot of a Si(001) surface at T=580K. Open squares represent the initial positions, solid circles the positions after 10^6 MCS. Dashed lines indicate anti-phase domains.

tures do not improve with MC time: after a quick reorganization of the atoms at the beginning of the simulation, the configuration becomes almost frozen and only small oscillations of the atoms around their positions are observed. Both the excessive number of undimerized atoms and anti-phase domains are problems found in every simulation. They are, therefore, due to the method itself, and an immense number of MCS would be required to see further changes.

It is known from *ab initio* calculations [14], and our results agree, that when two atoms with two dangling bonds each form a dimer, they lower their energy of about 2 eV/dimer. On the contrary, the energy gained when two or more dimers line up to form a dimer row is at least one order of magnitude smaller. This gain is actually so small that some classical potentials, e.g. Tersoff [76], find misaligned dimers to be energetically lower than dimer rows. In light of all this, the excessive number of undimerized atoms seen in our simulations can be easily explained. When the simulation begins, the surface energy is significantly lowered every time a dimer is formed, independently from the resulting dimer alignment. This means that each atom randomly tries to form a dimer with any of its i neighbors, and such a process obviously leads to a disordered surface as in Figure 5.5. Once that this surface reorganization has taken place, the only way to eliminate "defects" (i.e. atoms that have been left undimerized) is to break some of the dimers already formed. It is important to remember that when performing standard MC simulations the maximum displacement that each atom is allowed to move in a single step is small compared to the inter-atomic distances, so that appreciable acceptance can be achieved. Because of that, if only single-atom moves are allowed, the removal of a defect requires the following two-step process, at best. At first, one of the atoms that is already part of a dimer must move towards the defect, i.e. away from its neighbor. Later, the defect itself has to move close enough to its new neighbor to form a bond. During the first part of this process the original dimer is broken, while the new dimer hasn't

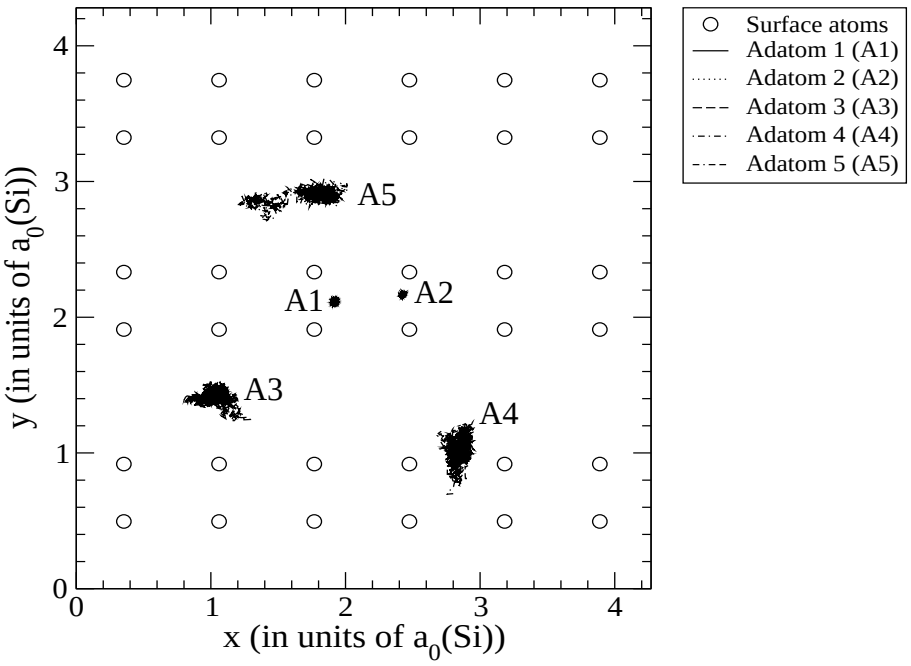

Figure 5.6: Example of results obtained for adatom diffusion: the solid lines indicate the positions that each adatom went through during the simulation. Open circles indicate surface atoms. The simulation was 8.5 $\times 10^5$ MCs long, T=0.16 eV.

.

formed yet. The energy cost of breaking a dimer makes the first step in this process extremely inconvenient energetically. This corresponds to having an excessively low acceptance in a Metropolis MC, since the acceptance probability depends exponentially on the energy difference between the initial and the final state. The reason for the formation of anti-phase domains is very similar: once dimers have formed randomly on the surface, their rearrangement in organized rows can only happen via a series of intermediate configurations where one atom per dimer has moved away from its neighbor in order to align with a different dimer row. A state like this has high energy and is, therefore, extremely unlikely to be accepted.

Similarly unsatisfactory results were obtained when we tried to simulate the evolution of an island on top of the surface or adatom diffusion. In both cases we always obtained final configurations that are practically identical to the initial ones, independently from the length of the simulation itself. As an example, the MC diffusion paths obtained for five adatoms are shown in Figure 5.6 after a 8.5 $\times 10^5$ MCs long simulation at T=0.16 eV (i.e. extremely high temperature). The adatoms initially deposited far from surface atoms moved a bit in the course of the simulation, while those starting close to surface atoms barely moved at all.

As mentioned before, this can be explained in terms of the energy cost of bond breaking. If only small displacements are allowed for each trial move, then it is extremely unlikely that an atom succeeds in moving away from a step edge, in the case of an island, or from a nn surface atom, when considering adatom diffusion. The reason for this is that the atom is forced to go through a series of energetically unfavorable configurations, because of the inconvenient placing of its other neighbors, while moving away from its original nn and before reaching a new, energetically convenient location. On the other hand, if long jumps are allowed, we still obtain very low acceptance because atoms already forming dimers attempt to move so far from their neighbor that they break the dimer bond. This, too, corresponds to a high-energy situation, i.e. to low acceptance.

5.2 The need for a collective MC algorithm

The results presented in Section 5.1.2 clearly show that standard MC, i.e. MC where only *single-atom* moves are utilized, doesn't represent an efficient way to simulate complex phenomena such as those occurring on the Si(001) surface. It is also clear that the reason for such a failure is in the impossibility of including collective processes in the MC move.

Traditionally Molecular Dynamics (MD) has been used when collective processes play a key role in determining the physics of a system. Unfortunately it has been established that phenomena like step edge modification or island thermal decay occur on a time scale of the order of seconds [29, 32, 33, 39, 50]. This means that extended periods of time have to be simulated if these problems are to be addressed. In MD the need to integrate the equations of motion demands the use of time-steps of the order of femtosec at best, so that it is just not possible to cover a time span of a few seconds. This makes MD unsuitable for our investigation. A different possible approach is the use of Kinetic Monte Carlo or of standard MC with a solid-on-solid model (some results obtained with this method are shown in Chapter 2). These techniques though require a pre-knowledge of the possible diffusion mechanisms and simulation results are strongly dependent on how well a large number of parameters is fitted. Moreover, the use of a solid-on-solid model forces discretization on the system, so that restrictions to the atomic motion are introduced.

Because it is our desire to investigate surface behavior with as few restrictions as possible, we decided to develop a new Monte Carlo algorithm instead of simply utilizing any of the above listed techniques. The particular version presented in this dissertation is targeted to the study of the Si(001) surface with Si or Ge adatoms, but the idea behind it is rather general and can be easily expanded to the study of other semiconductor surfaces. The main idea that this algorithm is based upon is to add the possibility of collective moves to the standard MC *single-atom* moves. With MC the evolution of the system is definitely faster than it would be using standard Molecular Dynamics; moreover, because of the collective moves, it is possible to overcome high potential barriers that otherwise would trap the system in metastable states. The identification of the collective moves to implement is the only point where some knowledge of the particular physical system under consideration is necessary. As an

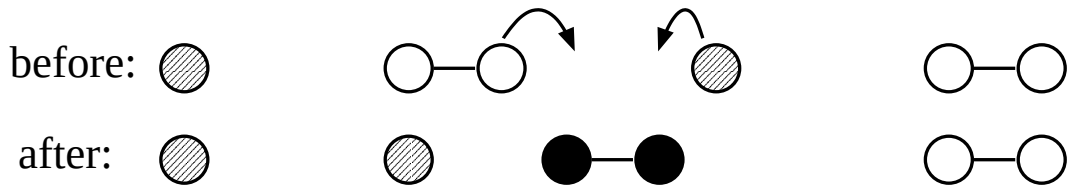

Figure 5.7: Coupled jumps: dashed circles represent undimerized atoms, open circles are dimerized atoms and solid circles indicate the new dimer that formed after the *coupled jump* took place.

example, in the case of the Si(001) surface, the existence of a (2x1) reconstruction leads us to introduce the possibility of moving each dimer as a whole.

5.3 Implementation of "coupled jumps" and "row shifts"

The simplest kind of collective move that we considered is designed to aid the production of the (2x1) reconstruction when starting from an unreconstructed surface. This was useful for a complete testing of the potentials [76].

When reviewing results obtained using single-atom moves only, we determined that the reason for the extremely low acceptance obtained once the dimers have formed was the high-energy cost of the intermediate configurations. A natural solution to this problem is to introduce the possibility of moving two atoms at the same time ("coupled-jumps"). This is accomplished choosing an atom on the surface and randomly selecting its left or right neighbor along the direction perpendicular to the dimer rows. The two atoms are then randomly moved towards or apart from each other of a random amount, as shown in Figure 5.7. In this way we rarely end up comparing a configuration with two dimerized atoms and an undimerized one to a configuration with three undimerized particles, as always happens in the *single-atom* move case. Now, mostly, if a dimer is broken, another one is formed, so that

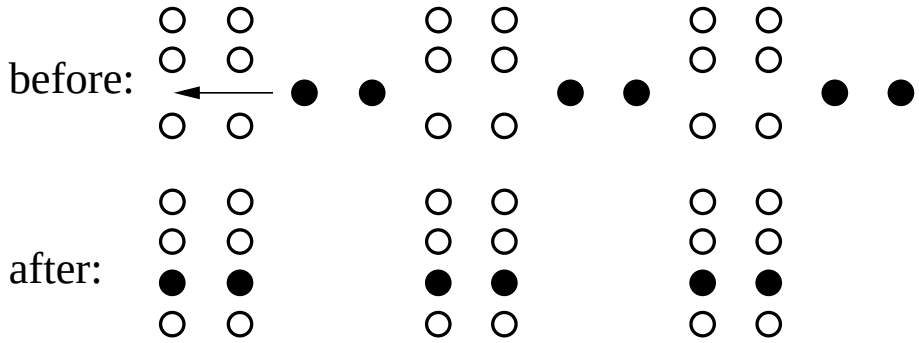

Figure 5.8: Row shifts: open circles represent dimers already aligned in rows, solid circles represent dimers out of alignment before the collective move.

the energy difference between the initial and final configuration is rather small, and consequently the acceptance is relatively high. This move is rather straightforward to implement, only requiring a larger cutoff for the Verlet list (list of neighbors) than that usually utilized for single-atom moves, because of the need for long jumps. Detailed balance is perfectly obeyed in this case.

Similarly, we can speed up the elimination of the anti-phase domains by introducing the possibility to shift a dimer column as a whole. This is shown in Figure 5.8. As it will be discussed more in detail in Chapter 6, all the simulations starting from unreconstructed surfaces ended up with the expected (2x1) reconstruction when using collective moves and SW potential.

5.4 **Implementation of "dimer jumps"**

The aim of our surface investigation is the analysis of phenomena like step edge evolution or island stability as a function of temperature or size. From the simulations done to reproduce the (2x1) dimerization we have learned how important it is, from a computational point of view, not to break a dimer bond without forming another

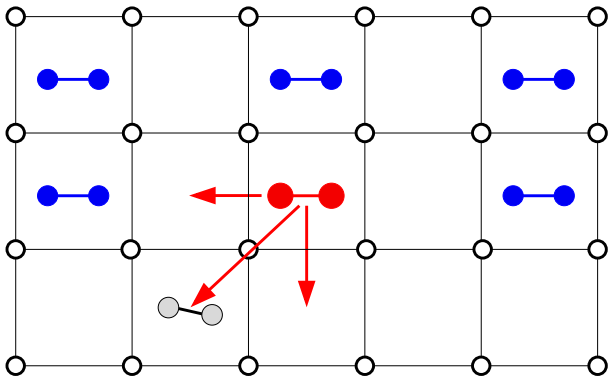

Figure 5.9: Schematic representation of an island edge: the island atoms are dimerized (solid circles) while those on the surface (open circles) sit on a perfect diamond lattice (for simplicity sake). The dimer attempting to move is represented by larger solid circles, and the arrows show some of the possible directions of motion. An example of final position for such a dimer is shown by the gray shaded circles.

at the same time. Therefore, in order to efficiently simulate edge fluctuations, we need to introduce a way to move each dimer as a whole. This is the key point in the *dimer jumps* algorithm, whose multiple implementations are described below. Each implementation is algorithmically correct but not as efficient in reproducing the physics of the (001) surface as the one that follows it.

5.4.1 **First implementation**

Our first attempt to introduce the possibility of dimer jumps was pretty straightforward: once that two atoms are identified as belonging to the same dimer, they are translated by the same random amount at the same time. A small rotation of the dimer ($\theta_{max} = 5$ or 10 degrees) is attempted as well (Figure 5.9), before comparing the energy of the final configuration to that of the configuration before the jump. The move is then accepted or rejected using the standard Metropolis criterion. The possibility of deciding how often to perform such a collective move is also intro-

duced in the code: the parameter *N_skip_coupl* indicates how often the dimer jumps are attempted.

An important observation related to the introduction of this kind of move is that a fast evolution of the system is attained only if a rather long maximum displacement (*maximum jump*) is considered. Because of geometric considerations, the central area of each square formed by surface atoms, as shown in Figure 5.9, is an energetically favorable location for the dimers. On the contrary, high energy corresponds to a dimer located across one of the lines in Figure 5.9. If one of the dimers in Figure 5.9 tries to move to a significantly different location by a series of small steps, then it has to battle the high potential barriers due to a whole series of energetically inconvenient positions. This problem is completely avoided if the possibility of very long jumps is introduced. Specifically, a maximum jump of $0.9 \times a_0(\mathrm{Si})$ was usually considered in the program along the x and y directions, to compare to a maximum displacement of $0.010 \times a_0(\mathrm{Si})$ used in the case of *single-atom* moves. Along z the maximum jump was usually about $0.075 \times a_0(\mathrm{Si})$ because no particular barriers are expected in this direction.

The computational cost of this "shortcut" is the need to consider a much larger *skin distance* than before (Section 4.7.1): the *cutoff* distance that we considered for dimer jumps is $2.60 \times a_0(\mathrm{Si})$ instead of $0.8 \times a_0(\mathrm{Si})$, as in the case of *single-atom* moves. In order to minimize the computational and memory cost of such moves, we considered separate nn lists for the "bulk" (i.e. *single-atom*) moves and the surface dimer jumps. Moreover, given the long range of the dimer jumps, the parallelization scheme described in Section 4.7.2 becomes unsuitable for surface moves because the surface cutoff is now different and much bigger than the "bulk" cutoff. We therefore added to the previously described parallelization a second one, active only when the code is performing dimer jumps, in which each surface is assigned to a processor. Considering the system sizes that we worked with, and the size of the surface cutoff,

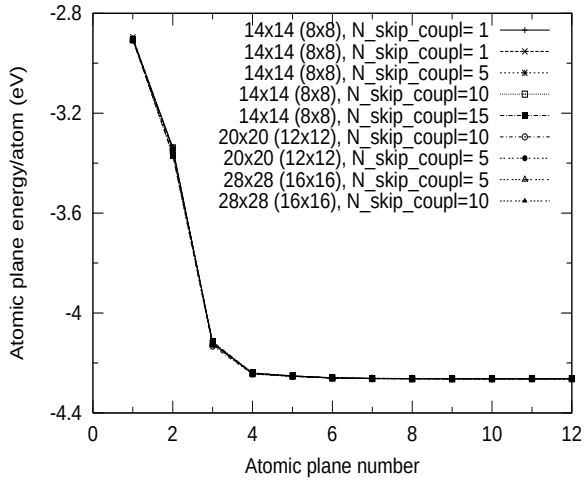

Figure 5.10: Atomic plane energy per atom as a function of depth inside the slab: atomic plane 1=surface, atomic plane 12=in the middle of the slab. The first two numbers in each legend indicate the surface size, the numbers between brackets indicate the island size and *N_skip_coupl* tells how often the dimer jumps are attempted. Results obtained using SW potential, T=0.05 eV, Ge on the island and Si on the surface.

it was not convenient at this point to use more than one processor per surface. In the case of future calculations, when the algorithm is in its definitive formulation, all the testing is done and "really" large surfaces are considered, using more that one processor per surface will be efficient.

The outcome of all the simulations where the *dimer jumps* were implemented as just described was highly disappointing. If the initial configuration consisted in a (2x1) dimerized island on a (2x1) dimerized surface everywhere but under the island, then no acceptance was found for the collective move. Little acceptance was obtained if, unphysically, we considered as initial configuration a dimerized island on an undimerized surface, so that the atoms on the surface aren't in their minimum energy positions to begin with. Results obtained under these conditions are shown in Figures 5.10 and 5.11 for Ge islands on Si surfaces and SW potential. In Figure 5.10

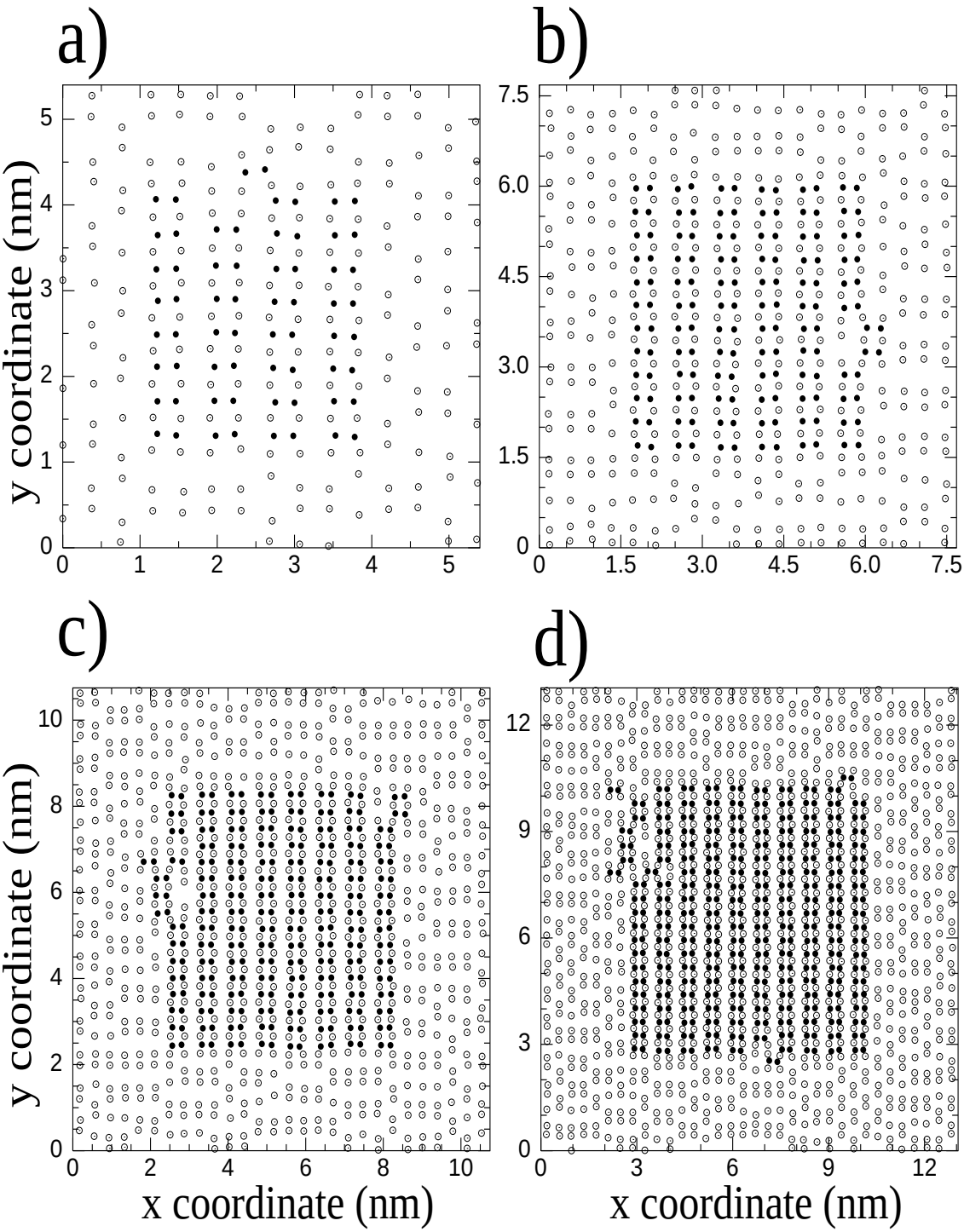

Figure 5.11: Ge island (solid circles) on Si surface (open circles) for different system sizes: (a) 14x14 surface, 8x8 island after 8 10^4 MCs, (b) 20x20 surface, 12x12 island after 4 10^4 MCs, (c) 28x28 surface, 16x16 island after 6 10^4 MCs, (d) 34x34 surface, 20x20 island after 4 10^4 MCs. In all cases SW potential and T=0.05 eV.

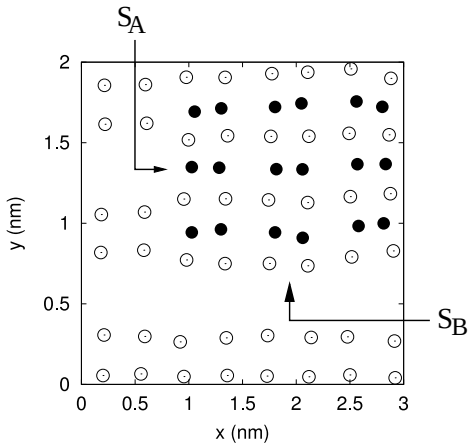

Figure 5.12: Snapshot of part of an island after 5,000 MC steps of relaxation at T= 700 K (i.e. before dimer-jumps are allowed). Open and solid circles are surface and island atoms, respectively. Parts of S_A and S_B steps are shown.

the energy of each atomic plane is plotted as a function of the plane number, i.e. as a function of distance from the surface (plane 1 corresponds to the surface and plane 12 to the the middle of the slab). Results corresponding to different system sizes and values of *N_skip_coupl* are compared, from which can be established that the choice of *N_skip_coupl* is not critical in the simulations and that no significant size effect can be detected at this point. Figure 5.11 shows examples of configurations obtained after $n \times 10^4$ MCs at T=0.05 eV (n between 4 and 8). Not only very few dimer jumps have been accepted, but unphysical reconstruction of the surface has occurred as well (as in Section 5.1.2), because the *coupled-jump* algorithm wasn't activated in these calculations for reasons of computational cost. It can therefore be easily speculated that those few moves that were accepted, had been accepted because of the unphysically high energy corresponding to some local configurations on the surface.

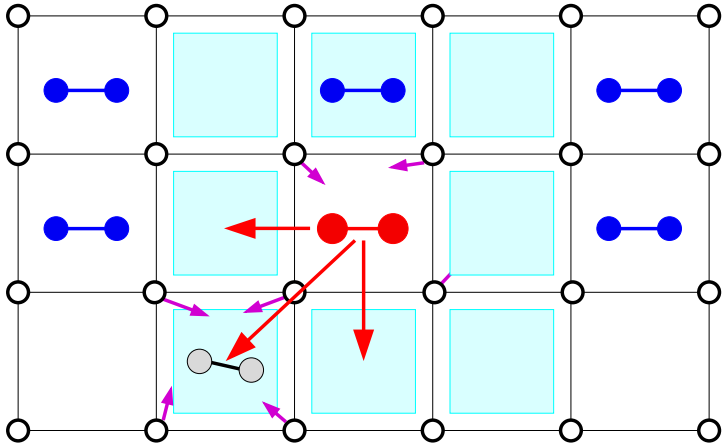

Figure 5.13: Schematic representation of an island edge: the island atoms are dimerized (solid circles) while those on the surface (open circles) sit on a perfect diamond lattice (for simplicity sake). The dimer attempting to move is represented by larger solid circles, and the arrows show some of the possible directions of motion. An example of final position for such a dimer is shown by the gray shaded circles. The small arrows indicate a possible displacement direction for the atoms that are allowed to move during the local relaxation.

5.4.2 **Second implementation**

The reason behind such a low acceptance for dimer jumps implemented as described above is in the difference between the geometry of a reconstructed and of an unreconstructed atomic environment. In Figure 5.12 one example of atomic arrangement in the neighborhood of S_A and non-bonded S_B edges is shown. The open circles are the dimerized atoms on the surface, while the solid circles are the atoms in the island. Let's consider the S_B step: when any of the dimers from the island is moved along the negative y direction by any amount between 0.25 and 0.6 nm, it ends up in a position such that at least two of his nearest neighbors are too distant to effectively act as nn. A similar problem is encountered at S_A and at rebonded S_B steps, with the difference that in this last case the nn distances end up being too short.

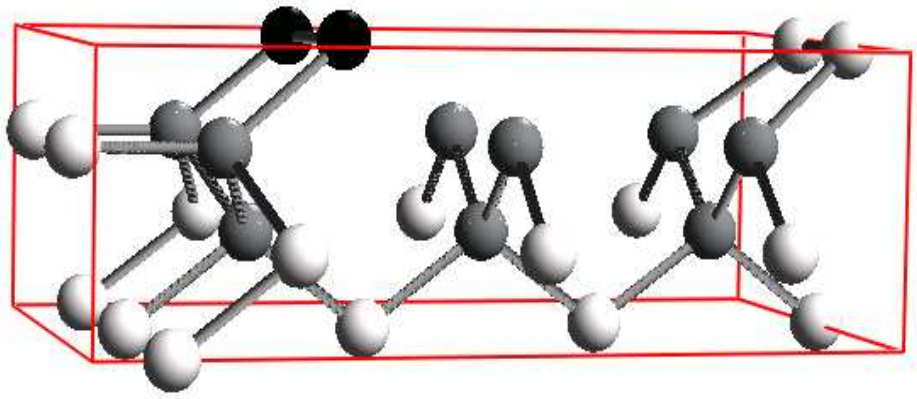

Figure 5.14: Dark gray spheres represent atoms that are moved during the local relaxation, light gray spheres represent some of their neighbors (for clarity not all of neighbors in the lowest layer are shown). The bonds are drawn for distances equal or less than 2.715 $\mathring{A}$. The dimer (black spheres) is shown just after it jumped and, at this time, only has 2 nn.

Summarizing, when considering a dimerized surface and a dimer-jump as described above, the acceptance rate is really low because most of the times the post-jump configuration ends up being extremely inconvenient energetically.

In order to achieve a much higher acceptance, once that a dimer is displaced as described in Section 5.4.1, we introduced the possibility of relaxing the local environment around it before deciding to accept or reject the move via the Metropolis algorithm. As *local environment* we consider all the dimer's neighbors before and after the move within a cutoff distance of 0.81 a_0(Si) and two layers from the surface. The dimer itself is included in such an assemblage as well. A schematic picture of such a collective move is given in Figure 5.13, where small arrows indicate a possible displacement direction for each of the atoms that are allowed to move during the local relaxation. In Figure 5.14 an example of local environment for one particular

dimer is shown. The dimer (black spheres) is shown just after it jumped, and at that time it only has two nearest neighbors.

The simplest way to introduce the possibility of such a local relaxation into the code is to insert a secondary MC loop (*mini-loop*) inside the loop over the dimers: for each dimer, once that the jump has been attempted, each of the atoms belonging to the *local environment* list attempts to move as well, and its new position is accepted or rejected via Metropolis. Every time each of the atoms in the list has tried to move once, one *mini*MC step is completed. At the end of the *mini-loop* the energy of the final configuration is compared to the energy of the configuration before the dimer jump, and the final configuration is accepted or rejected via Metropolis. Usually, a relatively high number of *mini*MCs (60 to 80) are necessary to attain significant acceptance for the global move.

The addition of local relaxation to the dimer jump was definitely successful: enough acceptance is now obtained at reasonable temperatures (T=0.08 eV) to enable some study of step edge evolution and island modification. In Figures 5.15 and 5.16 some qualitative results are displayed as examples of the algorithm capabilities. In all cases the initial configuration consisted of a (2x1) reconstructed island on top of a surface (1x2) reconstructed everywhere but under the island, as seen experimentally. In Figure 5.15 a) and b) systems of almost identical size are shown after evolving at two different temperatures for the same amount of MC time. No significative change in atomic positions has occurred in the lowest temperature case (a), with respect to the initial configuration. On the contrary, in (b) the island has altered its initial squared shape to a certain degree. An increase in the step edge modification with temperature is certainly to be expected, but we interpreted the lack of modification at T=0.05 eV as mostly due to having quite low acceptance of *dimer jumps*. Apart from such indications that the algorithm efficiency still has to be improved, these preliminary results showed very encouraging features, like the fact

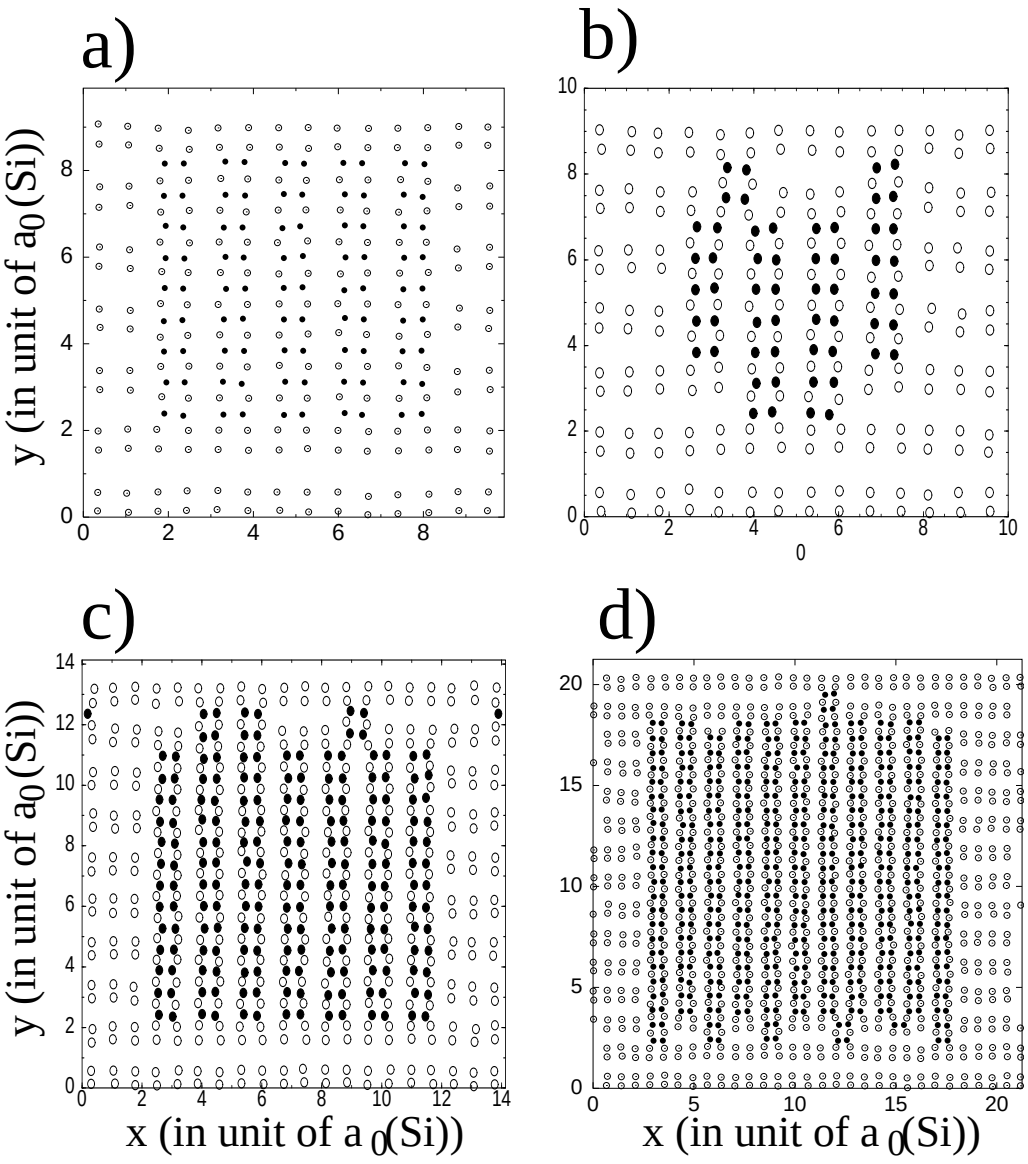

Figure 5.15: Configuration snapshots: a) 14x14 surface, 10x9 island, T=0.05 eV, 40K MCs, b) 14x14 surface, 8x7 island, T=0.08 eV, 40K MCs, c) 20x20 surface, 14x14 island, T=0.08 eV, 20K MCs, d) 30x30 surface, 22x22 island, T=0.08 eV, 25K MCs. Solid circles represent Si atoms on the island, open circles Si atoms on the surface.

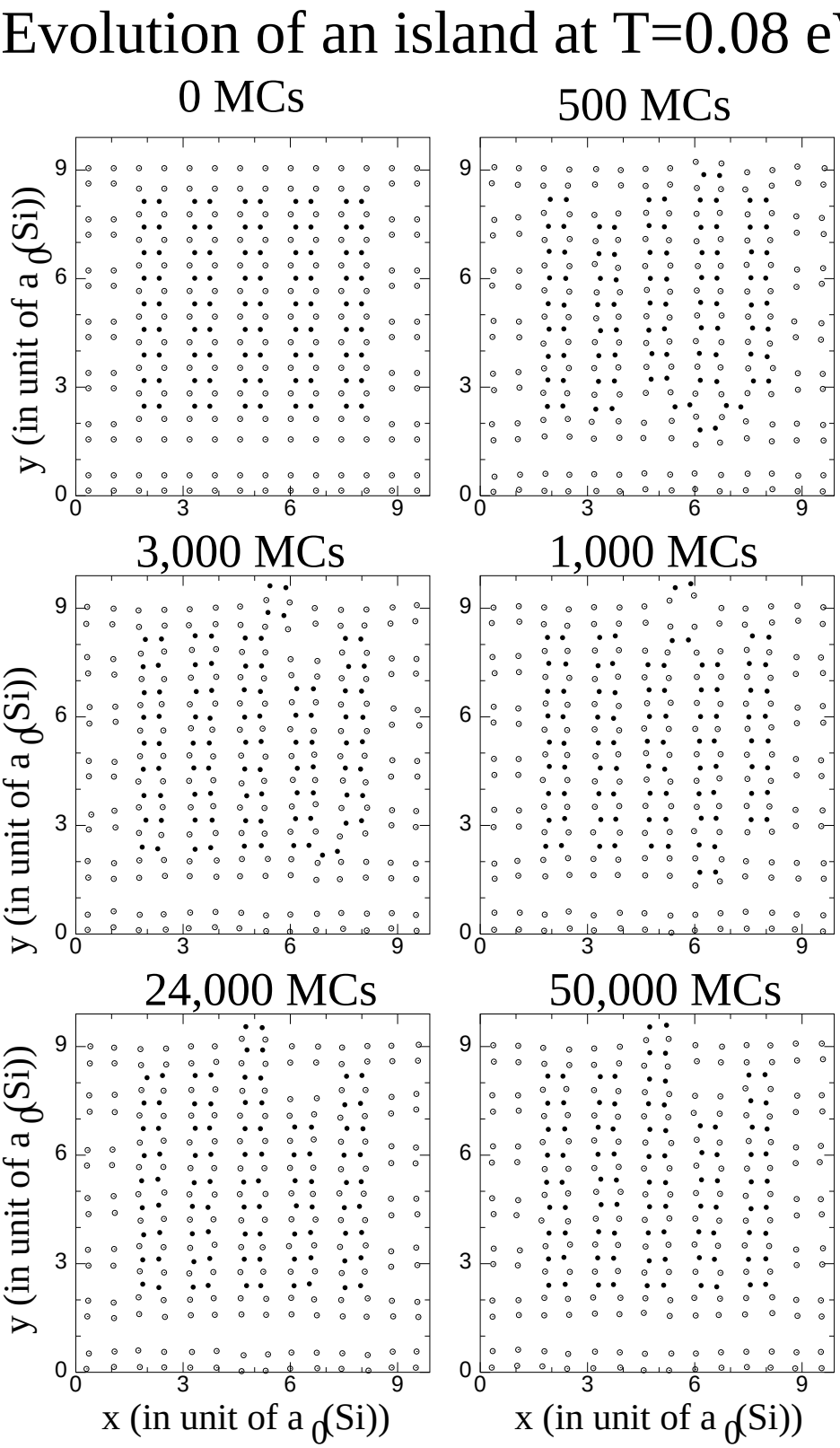

Figure 5.16: Configuration snapshots describing the evolution of a 10x9 island on a 14x14 surface at T=0.08 eV.

that much higher modification was seen at S_B steps than at S_A ones, in agreement with experimental results.

5.4.3 Final implementation

The addition of the local relaxation to the dimer jump introduces the "collective motion" effect that is needed to correctly describe the physics of the (001) surface. The only problem still to solve in designing the algorithm is its low efficiency, i.e. we must find a way to obtain higher acceptance for the collective move without increasing the computation time.

This goal is reached by substituting the MC *mini-loop* with a Molecular Dynamics (MD) one: now the new positions for the atoms during the *mini-loop* are determined from the integration of the equations of motion with the Velocity Verlet algorithm (Appendix B). The explicit form for the forces obtained from the SW potential is given in Appendix C. Initial velocities are assigned from the Maxwell velocity distribution at the simulation temperature. Later, constant temperature conditions are maintained using velocity rescaling. Test runs performed on different system sizes and under different initial conditions showed that, in most cases, a relaxation of 7 MD steps using a time step of 10^{-15} sec is enough for achieving good acceptance. On average, the acceptance obtained using this final implementation of the algorithm is about 8 times higher than using MC in the *mini-loop*.

Checking that detailed-balance is obeyed is much more difficult in this case than it is when dealing with "coupled-jumps". We could not find a way to explicitly calculate the probability for the exact reverse path, once that a dimer-jump is accepted. However, no biases of any kind are applied when choosing the direction of the jump and the only effect of the MD loop is to relax the neighborhood of both places where the dimer used to be and where it is as a result of the jump. On this basis we feel confident that no appreciable violation of detailed-balance comes from the use of this

collective move as long as the system is sufficiently relaxed before the dimer-jumps are started. For the same reason, it is important that not too many collective moves are accepted during each MC step, so that enough time is given to the system to relax in-between accepted dimer-jumps. That is the case in our simulations where, moreover, a value of at least 5 was always chosen for *N_skip_coupl* as a way to further insure relaxation between dimer-jumps. As independent test of the fact that MD does not impose some kind of bias in determining the configuration at the end of each dimer-jump, i.e. that the detailed-balance violation, if exists, has no appreciable consequences on the evaluation of the physical quantities, we compared results obtained using MD to those obtained using MC in the *mini-loop*. In all cases the results are qualitatively consistent with each other.

Chapter 6

Results for the Si(001) surface

In this chapter we present the most significant results obtained applying the combination of *single-atom* and collective moves described in Chapter 5 to the study of Si on Si(001). These findings are mostly qualitative, and are intended to prove the efficacy of the algorithm. As a consequence, only qualitative comparisons with experimental data discussed in Chapter 3 are discussed.

6.1 Coupled jumps and row shifts

As anticipated in Section 5.3, the introduction of *coupled jumps* and *row shifts* in simulations starting from undimerized surfaces lead to the formation of correctly reconstructed surfaces in reasonable computing times (on the order of 10^4 MCs) and at physical temperatures (T=580-800 K).

In Figure 6.1 snapshots of configurations obtained during one of these simulations are shown as an example. The initial configuration (a) consists of a reconstructed surface (open circles) on top of which we deposited an unreconstructed island (solid circles). In (b) a snapshot taken after 15,000 MCs is shown: most of the atoms on the surface have already formed dimers but a few defects, and consequent misalignment of the dimer rows, can still be seen. All the dimers formed by surface atoms under the island have already opened up. In (c) the final configuration is presented: all the dimers on the island are aligned in rows and no island atom is left undimerized. It must be noted, though, that considering an unreconstructed island as an initial

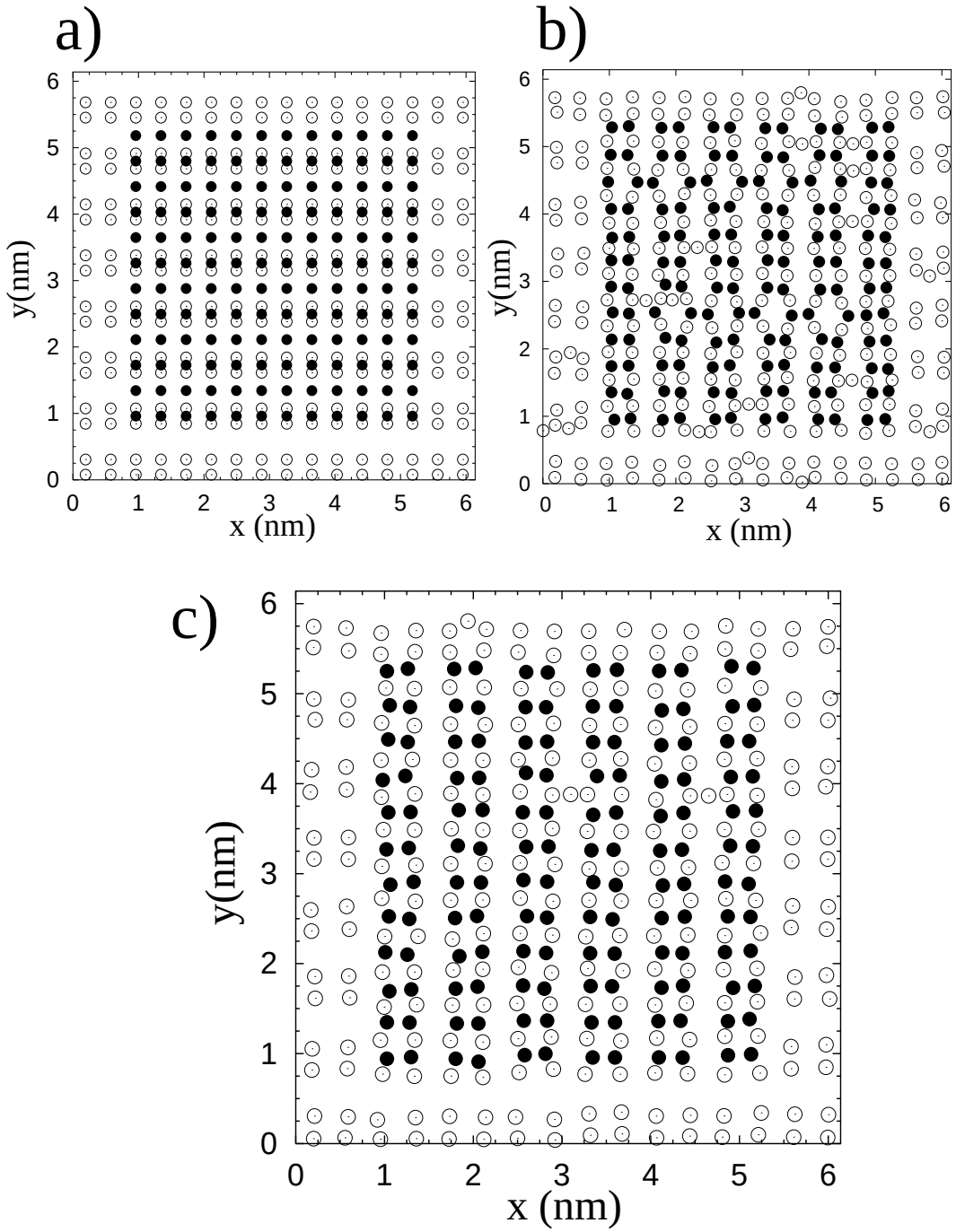

Figure 6.1: Snapshots taken after 0 MCs (a), 15,000 MCs (b) and 30,000 MCs (c) (T=580 K, 16x16 surface and 12x12 island). Solid circles are Ge atoms and open circles are Si atoms. Tersoff potential was used in this simulation.

configuration, instead of a surface, facilitates the alignment of the dimer rows. This is due to the presence of edges: because of them there is only one possible alignment that corresponds to a situation where all the atom in the column participate in a dimer. On a surface, however, this is not the case because of the 2D PBC, and obtaining an aligned, reconstructed configuration depends on the very small energy difference between the aligned and the misaligned case. As seen in Section 5.1.2, such an energy difference is much smaller than that between a dimer and two undimerized surface atoms. Consequences of this phenomenon are discussed in the next Section.

6.2 Tersoff potential vs Stillinger-Weber potential

Once that the collective algorithm was sufficiently efficient to be used, we were ready to start testing the interatomic potentials. This was accomplished by simulating surface reconstruction and island evolution with both Tersoff and SW potentials, and comparing results.

All the tests indicated that SW is a suitable potential for surface studies, while Tersoff isn't. Examples of final configurations obtained when trying to reproduce the (2x1) reconstruction using Tersoff potential are shown in Figure 6.2. Because of the use of *coupled jumps* no atom is left undimerized, but the introduction of *row shift* is not enough to prevent some phase-boundaries from forming. Our results show that this effect is temperature independent. As discussed in the previous Section, the energy difference between aligned and misaligned dimer rows is very small, and our findings suggest that the Tersoff potential doesn't reproduce this small energy difference correctly. The energy comparison between relaxed surfaces with and without phase-boundaries confirmed that, using Tersoff, the case with the presence of phase-boundaries is energetically more favorable. When performing the same kind of sim-

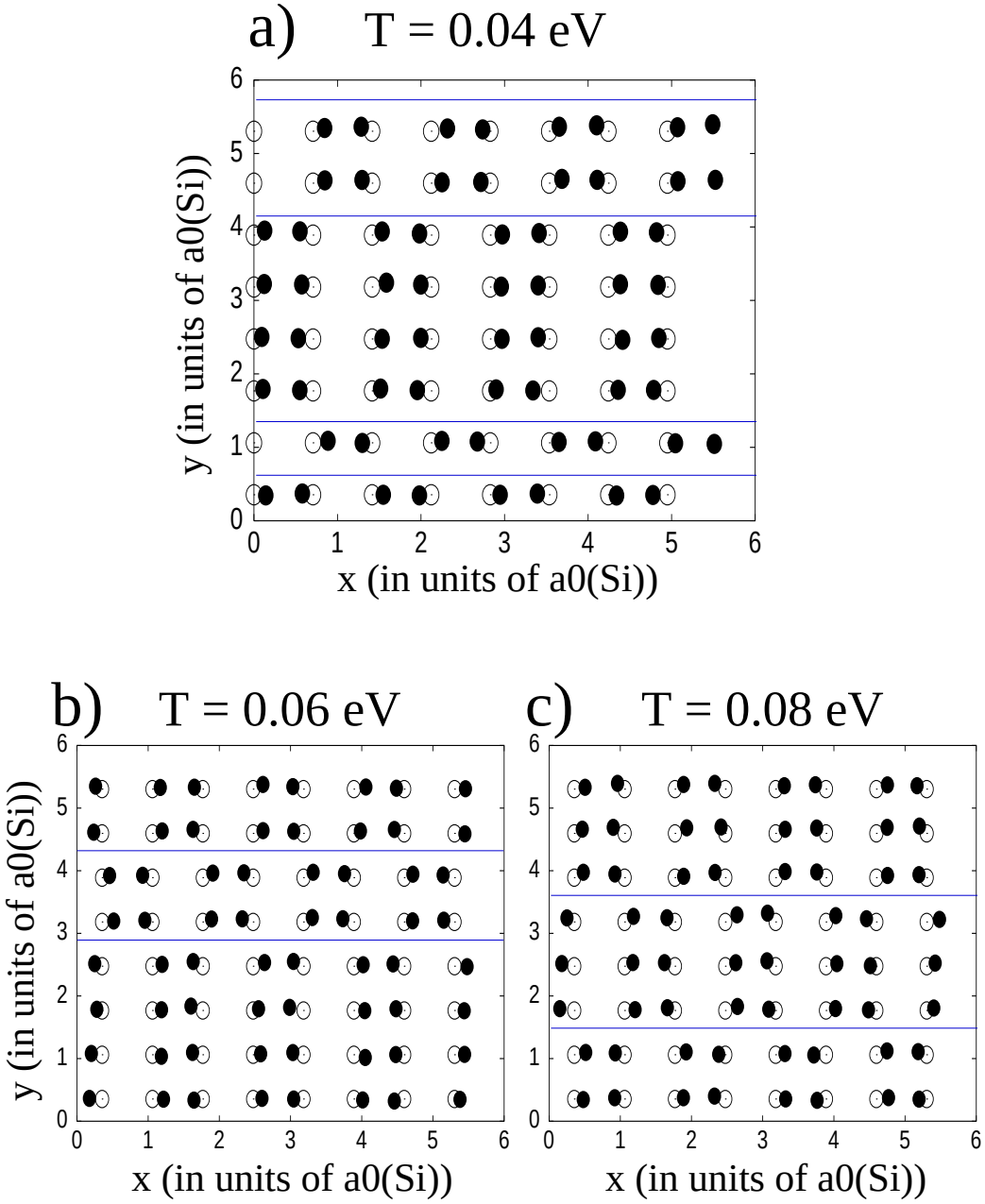

Figure 6.2: Snapshots of 8x8 surfaces of Si on Si(001) taken after 7.5 $\times 10^5$ MCs. The interatomic interactions are determined using the Tersoff potential. Open circles are initial positions (unreconstructed surface) and solid circles are the position at the end of the simulation.

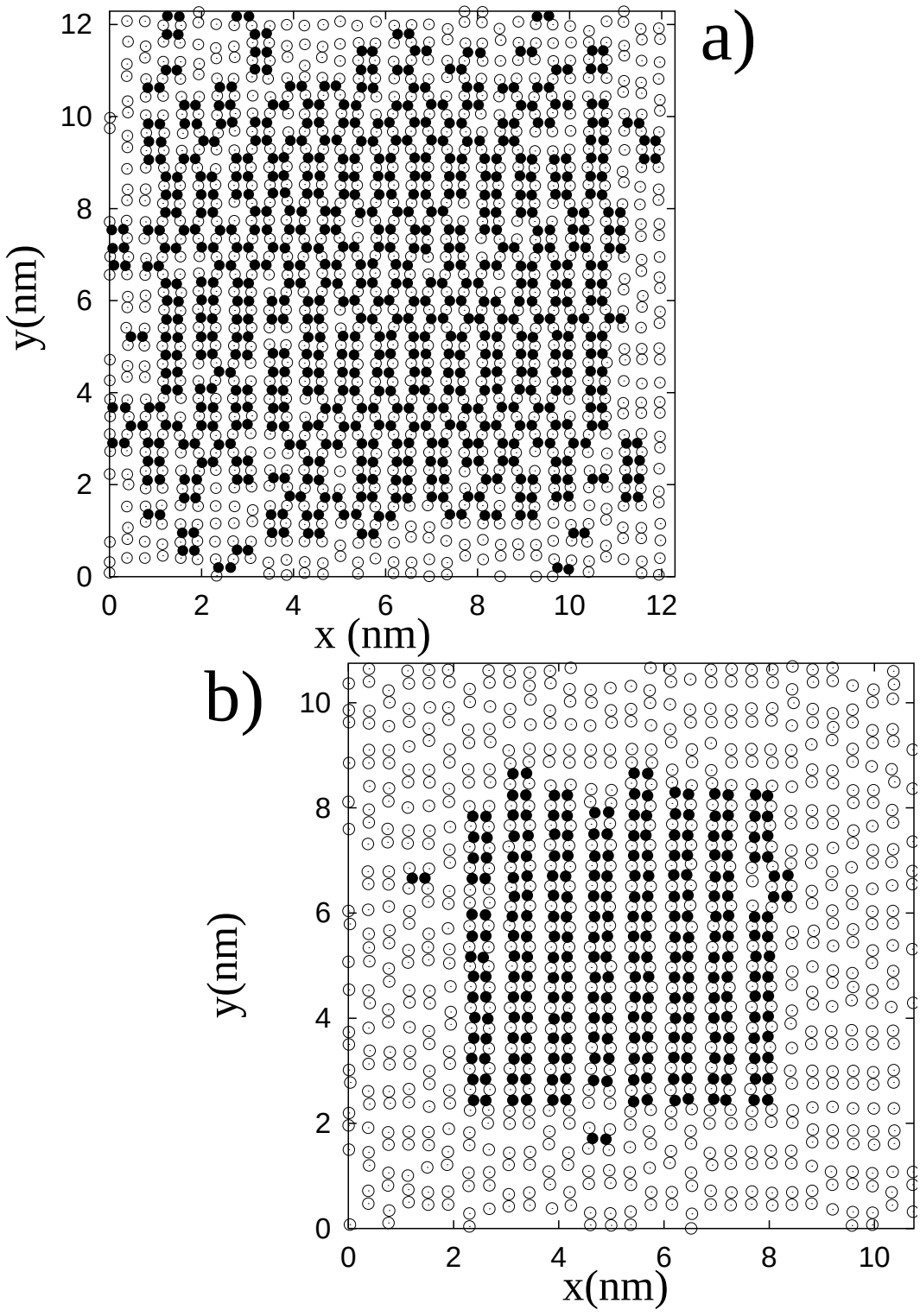

Figure 6.3: Configuration snapshots from simulations where the interatomic interactions are described using Tersoff potential (a) or SW (b). For (a): 32x32 surface, 26x26 island, snapshot after 35,000 MCs. For (b): 28x28 surface, 16x16 island, snapshot after 37,000 MCs. For both T=580 K.

ulations using SW potential, we always recovered the correct (2x1) reconstruction with complete alignment of the dimer rows.

As a second test, we studied the island evolution with both potentials. Again, results obtained using Tersoff were unsatisfactory while SW ones reproduced the correct physics. In Figure 6.3 a comparison between the two potentials is shown. The island simulated using SW is very stable and only shows some edge modification, as expected, but the one evolved using Tersoff is highly disorganized, having formed several anti-phase domains. The two simulations were run for a very similar number of MC steps at the same temperature. The differences found between the two islands are even more remarkable considering that the one simulated using Tersoff is larger that the other, therefore expected to be more stable.

6.3 **Island formation**

The first problem we decided to address as a test for our algorithm is the investigation of the early stages of formation of two-dimensional Si islands on Si(001). This study was performed considering as initial system for our simulations a slab of Si with (2x1)-reconstructed surfaces on top of which dimers are randomly deposited. Using the combination of single-atom and collective moves described in Section 5.4.3, and the possibility of changing of volume, the system is let to evolve at constant temperature. Temperatures typically used in simulations of this kind are around 900 K, because it corresponds to a rate of events fast enough to allow the observation of the physical phenomenon within a reasonable number of MC steps. As a matter-of-fact, all our simulations reached equilibrium within a couple hundred thousand MC steps at most.

In Figure 6.4 one example of results is shown: a snapshot of the (001) surface taken after 1.2×10^5 MCs at a simulation temperature of 930 K. Solid circles are

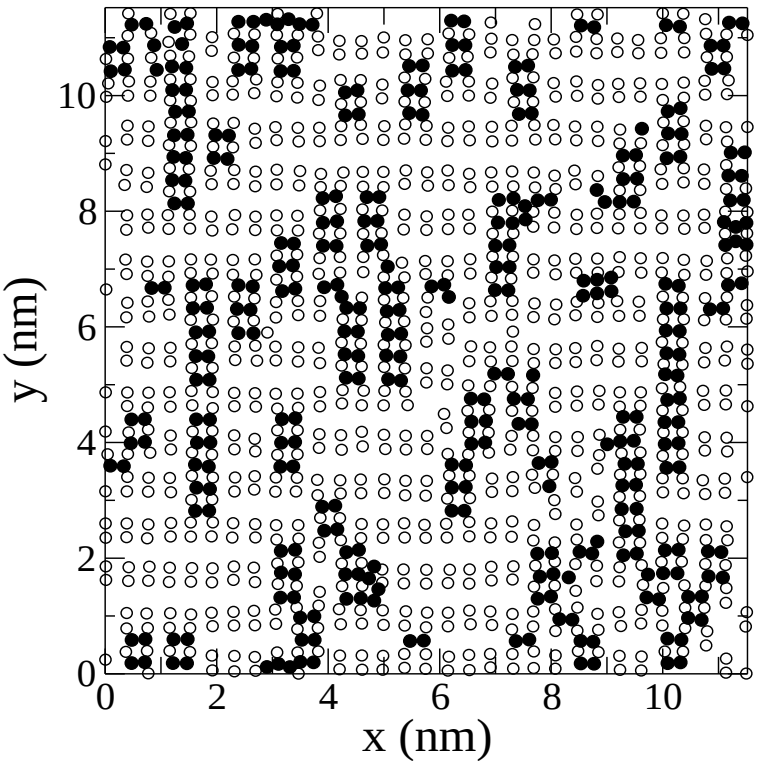

Figure 6.4: Snapshot of Si over Si(001) after 1.2×10^5 MCS, T=930K. Solid circles are adatoms, open circles are surface atoms. The surface contains 900 atoms (30x30, with pbc) and 170 dimers are deposited on top of it (the entire simulation slab contains 20480 atoms).

Si adatoms, while open circles represent atoms on the surface. The most noticeable feature is the fact that most of the ad-dimers have combined to form almost mono-dimensional islands. This is consistent with what was observed experimentally, as reported among others by Mo *et al.* [19] and Pearson *et al.* [45]. Note that everywhere adatoms have come together, the dimerization underneath has disappeared. A few transient configurations are still present; for example, the one where three dimers have united and aligned parallel to the dimerization direction on the surface. This is not an indication of unphysical behavior; it simply means that, at this time, the system has not yet reached complete equilibrium. Moreover, finding dimers in

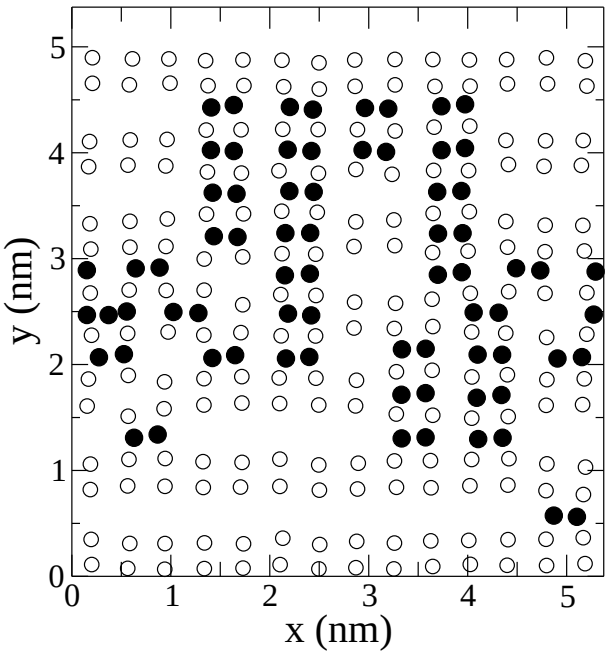

Figure 6.5: Snapshot after 3×10^4 MCS, T=700 K. Solid circles are adatoms, open circles are surface atoms. The surface contains 196 atoms (14x14, with pbc) and the initial square island was made of 72 atoms.

unexpected configurations emphasizes the fact that the dimer motion is not biased during the simulation: they are allowed to rotate, to separate into undimerized atoms (as shown the Figure 6.4 as well) and so on. All the results that we obtained studying the early phases of island formation are qualitatively identical to those presented here.

6.4 **Step-edge evolution**

A second, independent problem we used to evaluate the applicability of our method to real situations is the study of island stability and step evolution. When doing so, we always begin our simulations considering a square island of Si over each Si(001) surface, so that both S_A and S_B steps could be analyzed at one time. Simulations

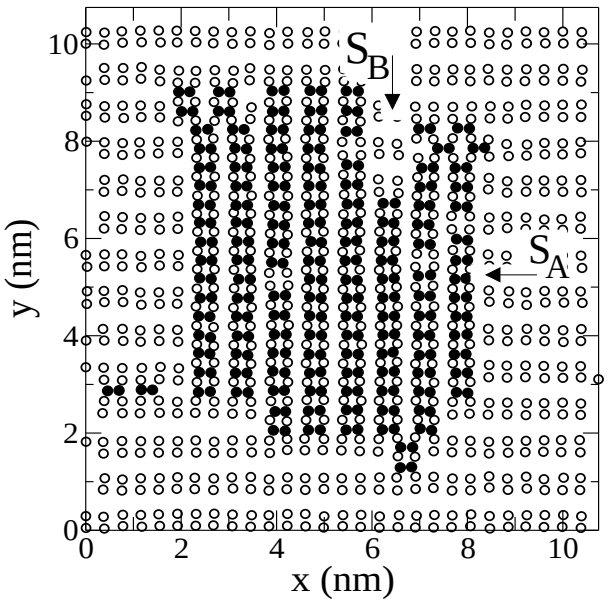

Figure 6.6: Snapshot after 7×10^4 MCS, T=700 K. Solid circles are adatoms, open circles are surface atoms. The surface contains 784 atoms (28x28, with pbc) and the initial square island was made of 272 atoms.

are performed at different temperatures and using different system sizes, so that both thermal and size stability are tested. The kind of results we achieve is well exemplified by the instantaneous configurations displayed in Figures 6.5, 6.6, and 6.7. Comparing Figures 6.5 and 6.6, it is easy to realize how well size stability is reproduced by our calculations: as experimentally observed [42,50,51] islands smaller than a critical size are not stable even at relatively low temperatures. It is not the aim of this dissertation to accurately estimate such a critical size, but from these results it appears that the algorithm developed here is suitable for such an inquiry. Moreover, in Section 6.5 preliminary quantitative findings on such a quantity are discussed.

From the observation of Figures 6.6 and 6.7, a dependence of the island stability on temperature can be easily inferred. In the two simulations the same system size

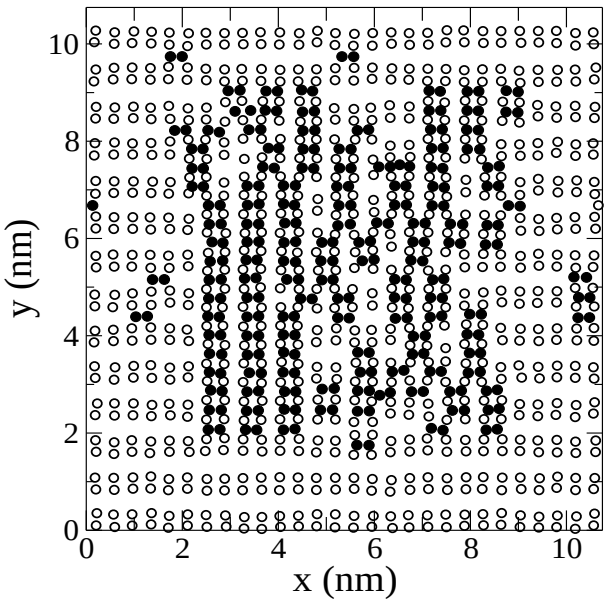

Figure 6.7: Snapshot after only 4,000 MC steps, T=928 K. Solid circles are adatoms, open circles are surface atoms. The surface contains 784 atoms (28x28, with pbc) and the initial square island was made of 272 atoms.

was used, the only difference being temperature. After only 4,000 MC steps the island that evolved at higher temperature (Figure 6.7) is almost completely disordered, while the other is still very stable after 7×10^4 MCS. This, too, agrees with previously reported experimental findings [29,38,51] Analyzing Figure 6.6 we note several other important features. Firstly the S_A and S_B steps have evolved in a very different way: both of the S_A steps are still pretty smooth, while the S_B steps have definitely become rough. The same behavior is consistently observed when STM images of terraces on the Si(001) are taken [28, 32, 34, 41] Secondly, the roughly square shape for the island has been preserved during the simulation, in good agreement with experimental observations of silicon islands on Si(001) before annealing [19, 29, 51]. Lastly, dimer vacancies have appeared in the island as the most widespread defect, and this, too, is a feature common to several experimental findings [19, 29, 51].

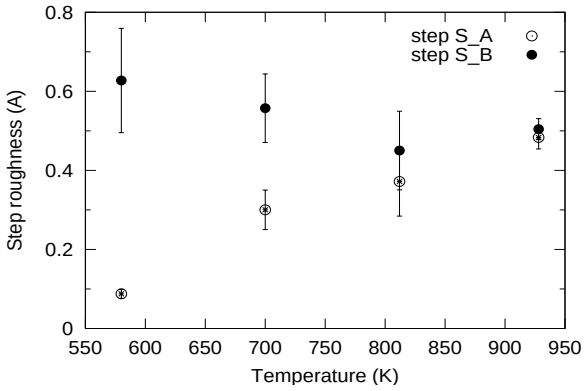

Figure 6.8: Step edge roughness vs. temperature for islands initially square and composed by 272 (16x17) atoms (surface size = 28x28 with pbc).

6.5 **Quantitative results**

Finally, in order to show that this algorithm can also be used for quantitative evaluations of physical quantities, in Figure 6.8 preliminary results on step edge roughness vs. temperature are presented for a particular island size (16x17). The details of the computations are outlined elsewhere [88]. Again, a strong temperature dependence and a definite difference in behavior between S_A and S_B steps can be noticed as long as the islands are stable, i.e. for temperature below 900 K.

Similarly, a preliminary determination of the critical island size at T=700 K (k_BT=0.06 eV) is shown in Figure 6.9 a). Islands initially containing less than the 80 dimers have reduced their size of more than 25% before reaching equilibrium, indicating that they are not stable at this temperature. On the contrary, islands larger than 130 are stable at T=700 K (their size at equilibrium is almost 90% of the initial one). In the case of islands initially made of 91 dimers we observed fast island decays in some runs and great stability in others (for runs of about 1.5 $\times 10^5$ MCs), which justifies the larger error bar. An error bar almost as large is found for

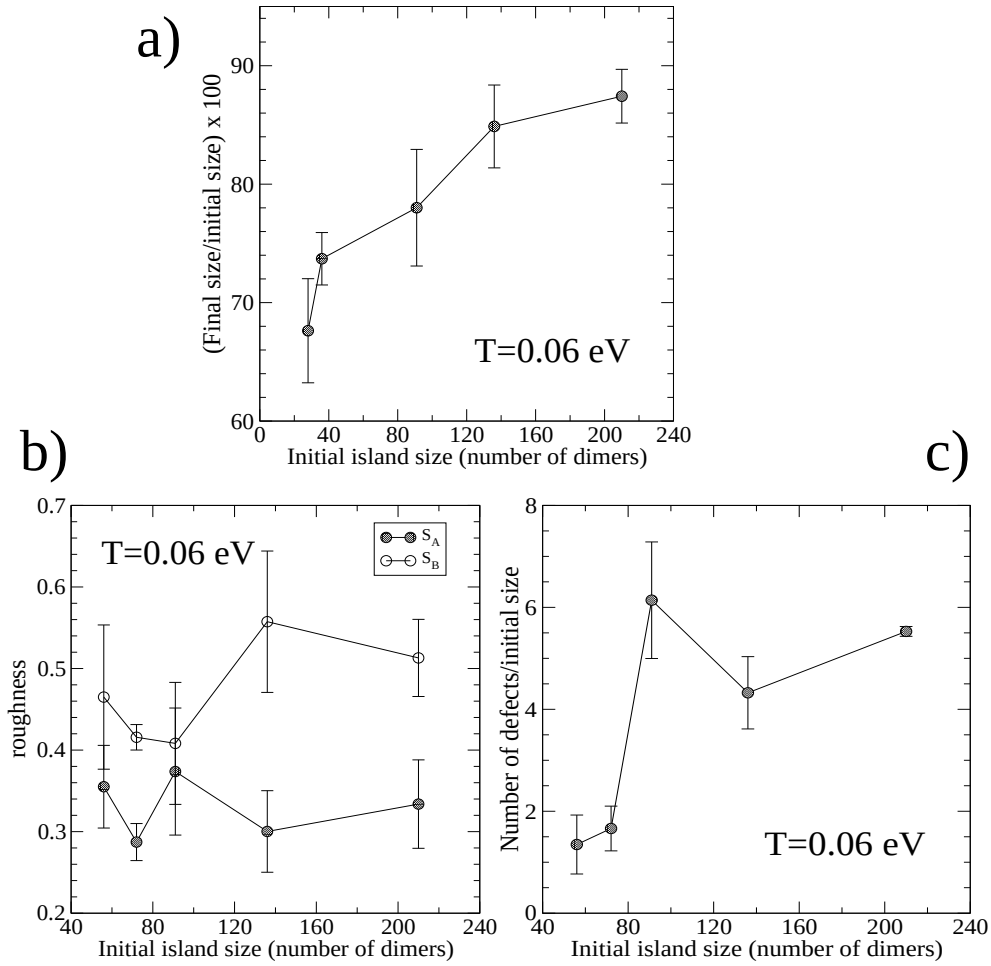

Figure 6.9: Critical island size (a), step edge roughness (b) and normalized number of missing dimers (c) vs. initial island size at T=700 K (k_BT=0.06 eV). All data are preliminary. In b) and c) data for islands below the critical size are taken before the disintegration starts.

an initial size of 52, and is due to the fact that in some runs the island disintegration was not completed within the time length of the simulation. Corresponding results for step roughness and number of missing dimers are displayed in Figure 6.9 b) and c). As seen in experiments, the step roughness does not depend on system size, and is higher for S_B steps than for S_A in case of stable islands. The measure of the number of missing dimers per island (normalized on the initial island size) clearly

shows a correlation between stability and presence of defects, being definitely higher for stable islands (initial size lerger than 130 dimers) than for unstable ones.

Chapter 7

Phase diagram for constant-volume $Si_{1-x}Ge_x$ alloy

In this Chapter we discuss results obtained using a bulk Si-Ge alloy model to study the compressible Ising model under constant volume conditions. Hysteresis results are presented first, then findings for the "ordered" phase and lastly the phase-diagram is determined in both the semi-grand-canonical and the canonical ensemble. The final part of the Chapter is dedicated to the discussion of the structural properties of the "ordered" phase.

7.1 Low temperature results

As discussed in Chapter 3, theoretical predictions suggest that the $Si_{1-x}Ge_x$ phase diagram under constant-volume conditions in the field-temperature plane ($\Delta\mu$,T) consists of two first order lines, one in the low and one in the high Ge-concentration (c_{Ge}) regime. To test such a prediction we looked for hysteresis in the Si and Ge equilibrium concentrations sweeping through the chemical potential difference $\Delta\mu = (\mu_{Ge} - \mu_{Si})$ at fixed temperature. In each case we started in the complete Si (or Ge) regime and first increased (or decreased) $\Delta\mu$, then swept it back to its initial value. During these runs each simulation started from the the final configuration of the previous one and was 10^5 MC steps long.

If too coarse a resolution is used in sampling $\Delta\mu$, the expected jumps in c_{Ge} are not visible, and results as in Figure 7.1b) are found, even if very large jumps were predicted theoretically (Chapter 3 and Figure 7.1a)). Data shown in Figure

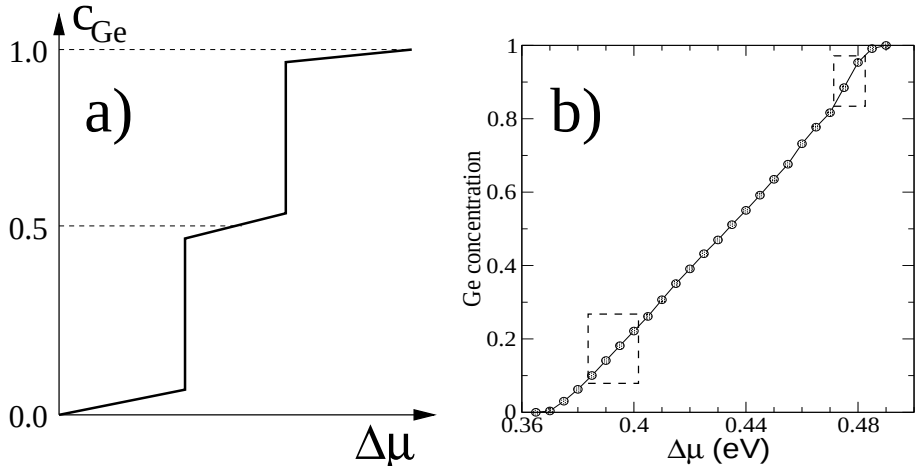

Figure 7.1: (a) Schematic diagram of c_{Ge} vs $\Delta\mu$ as expected from theoretical predictions (see Chapter 3). Note the size of the expected jumps in c_{Ge}. No marks are shown on the x-axis because no indications were given in the theoretical work on the actual values of $\Delta\mu$ corresponding to the jumps in c_{Ge}. (b) Ge concentration vs $\Delta\mu$ obtained when using a coarse resolution to sample $\Delta\mu$. The dashed squares indicate the locations where hysteresis is later found using a much finer resolution. Data are taken using a L=4 system, k_BT=0.0015 eV and 10^5 MCs per run. Each run started from the end of the previous one.

7.1b) are taken using a L=4 system, k_BT=0.0015 eV and 10^5 MCs per run. Each run started from the end of the previous one. When a much finer resolution is utilized, hysteresis is indeed found both for high and low c_{Ge}, as shown in Figure 7.2. Surprisingly, the difference in concentration between the branches (Δc) is in both cases much smaller than under constant-pressure conditions [65], indicating a much weaker first order phase transition. Comparing the two hysteresis loops we notice two main differences. Firstly, Δc is definitely smaller in the lower c_{Ge} regime than in the higher one. Secondly, the loop shape is different, being symmetric in one case and strongly asymmetric in the other. These differences indicate that the two regimes are somehow not equivalent, as partially expected from the asymmetry in

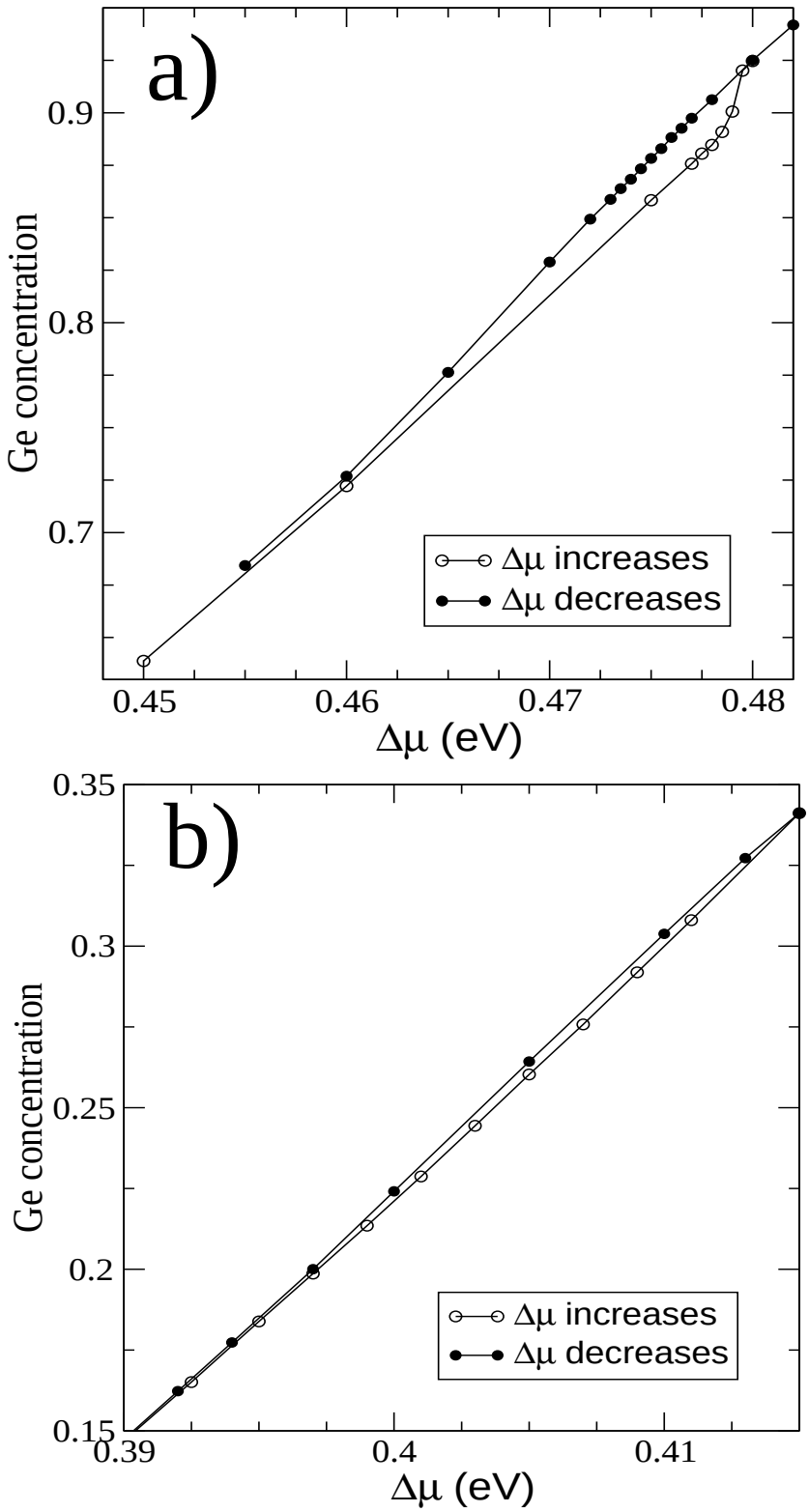

Figure 7.2: Hysteresis loops in the high and in the low Ge-concentration regimes ((a) and (b) respectively) for T=0.0026 eV.

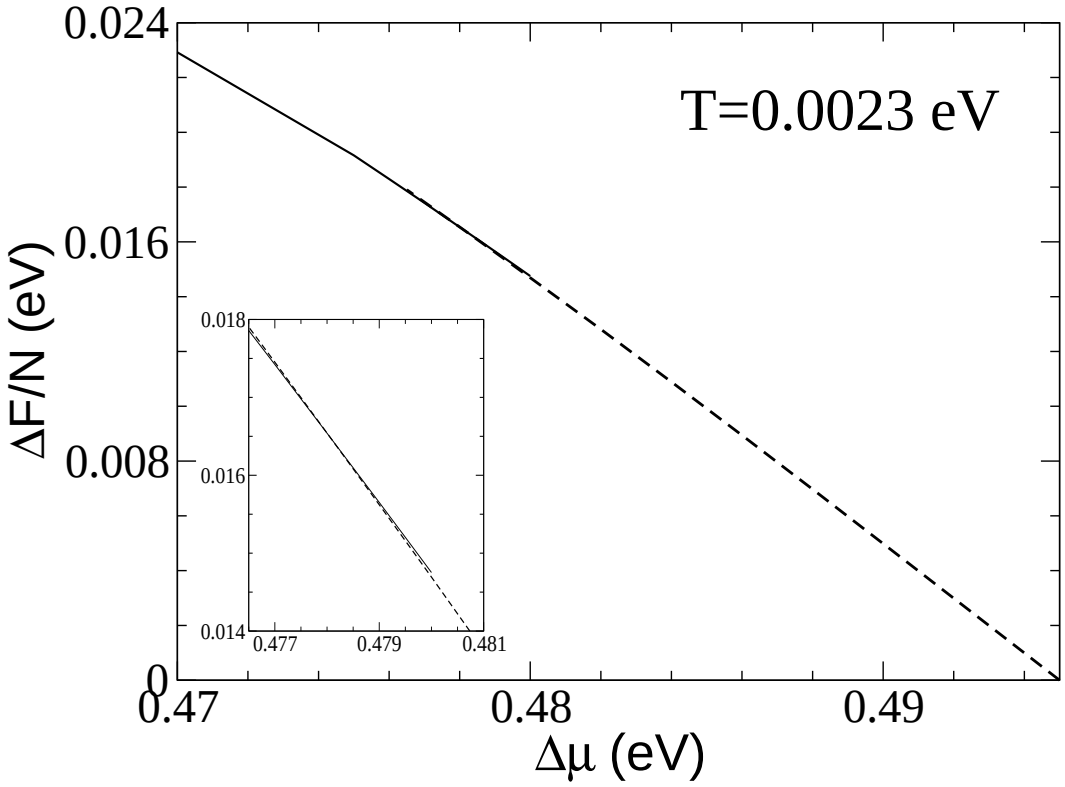

Figure 7.3: The branches of free energy obtained for T=0.0023 eV in the high c(Ge) regime. The inset shows the intersection on an expanded scale.

the potential and, even more, from having chosen a volume closer to that of pure Ge than to that of pure Si.

An important consequence of having such a weak transition is that the branches of the free energy are almost parallel, as shown in Figure 7.3. High precision is therefore necessary to evaluate such branches, i.e. relatively large systems (8000 atoms) have to be used even at temperatures below the transition. Relatively big error bars appear nevertheless in the final estimate of the phase diagram (Section 7.3). Moreover, hysteresis loops cannot be used to determine the phase diagram for temperature above k_BT=0.0030 eV because the difference in energy and/or concentration between branches becomes too small to be detected even using systems as large as

L=10. This behavior is qualitatively illustrated in Figure 7.4, where hysteresis loops obtained at different temperatures for low c_{Ge} are shown.

7.2 The "ordered" phase

In order to investigate the asymmetry seen in the hysteresis loops at high Ge concentration, structural properties of different configurations along the hysteresis paths were analyzed. As a result, the phase transition producing the hysteresis is interpreted as corresponding to a transition from a phase where equilibrium configurations are given by random mixture of the atomic species to one where the two phases segregates from each other ("ordered" phase).

When the phase separation occurs, the less favorable of the two atomic species (Si in this study, given the volume chosen) segregates surprisingly forming one or more planes in-between which the other species (Ge) is located. The number of such planes depends on the availability of Si: for high Ge concentration only one plane of Si is formed but, as the equilibrium concentration of Si increases, such a plane splits into more planes, instead of simply growing thicker. Another characteristic of these planes is that they try to grow perpendicular to each other as much as possible, i.e. we find two or more along the same direction only when more than three planes are formed. Examples of "ordered-phase" configurations are given in Figure 7.5, where snapshots of equilibrium configurations are shown at three different values of $\Delta\mu$ and the same T. In correspondence of the lowest c_{Si} ($\Delta\mu$=0.472 eV, c_{Ge}=0.83) only one plane of Si has formed (Figure 7.5a), while for c_{Ge}=0.55 there is already enough Si in the system to allow the formation of 3 planes (Figure 7.5b). It is easy to notice that these planes are perpendicular to each other. Figure 7.5c) correspond to a c_{Ge} so low (c_{Ge}=0.3) that several Si planes have formed. These findings explain the asymmetry found in the hysteresis loops: the formation of the Si planes is in fact a

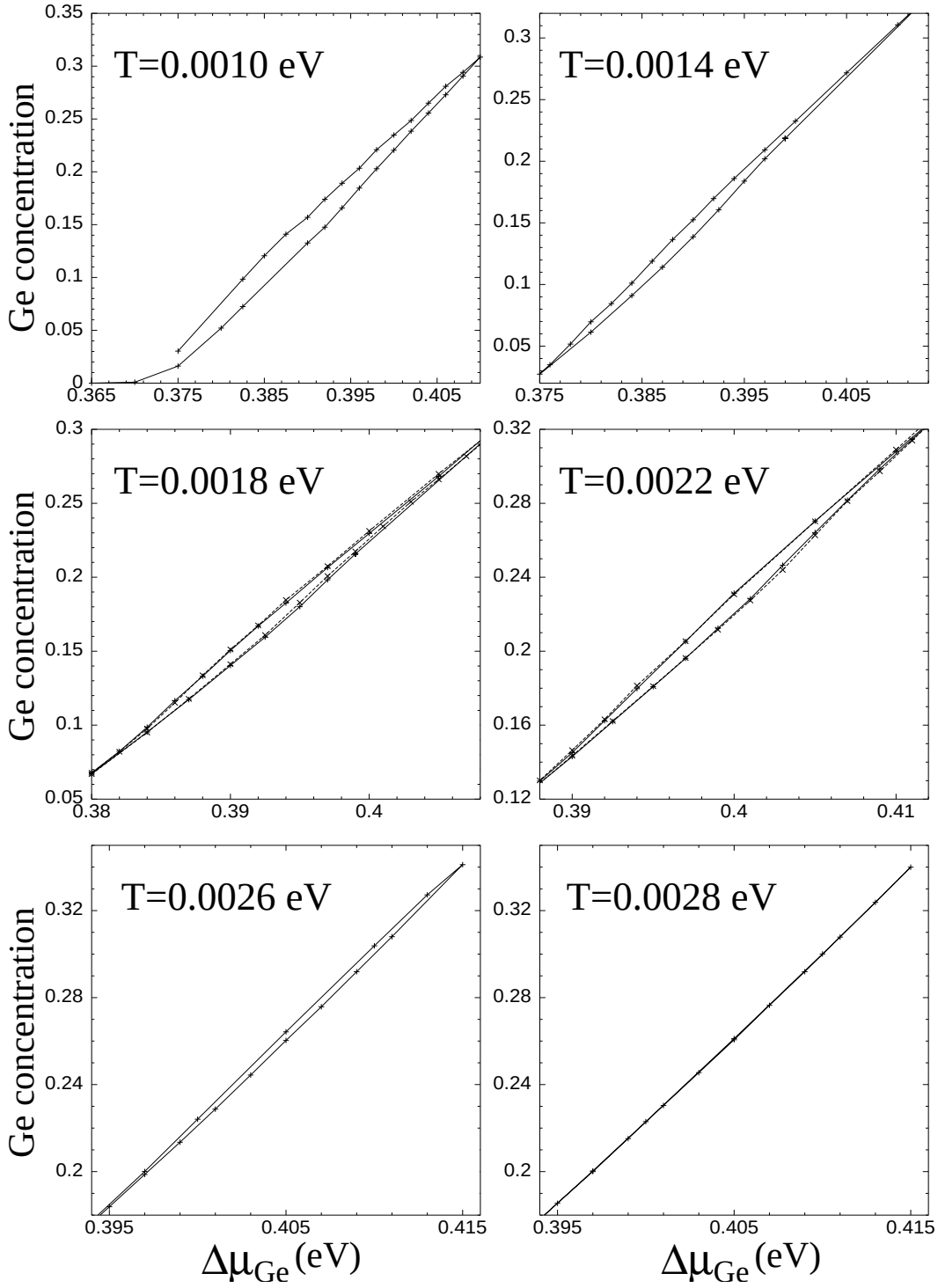

Figure 7.4: Hysteresis loops calculated using L=10 systems and different temperatures for low Ge concentrations.

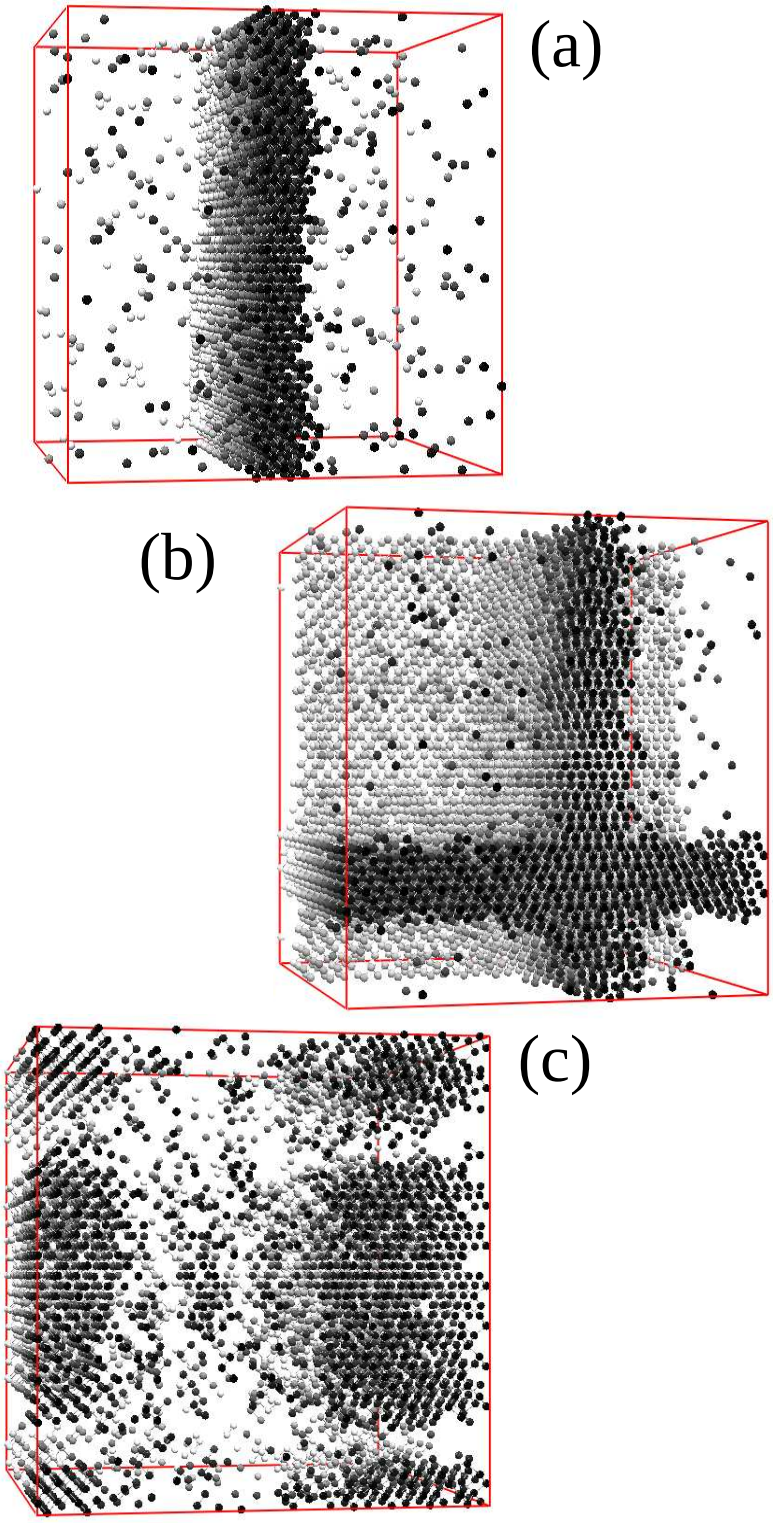

Figure 7.5: Snapshots of equilibrium configurations for $\Delta\mu$=0.472 eV (a), 0.440 eV (b) and 0.410 eV (c). The correspondent c(Ge) roughly is 0.83, 0.55 and 0.30, respectively; T=0.0029 eV in all cases. For clarity, in (a) and (b) only Si atoms are shown, in (c) only Ge. The gray scale is used to indicate depth: white atoms are the further from the reader, black atoms the closest. 3D PBC are used in all cases. Figure obtained using the grafic package AViz [92].

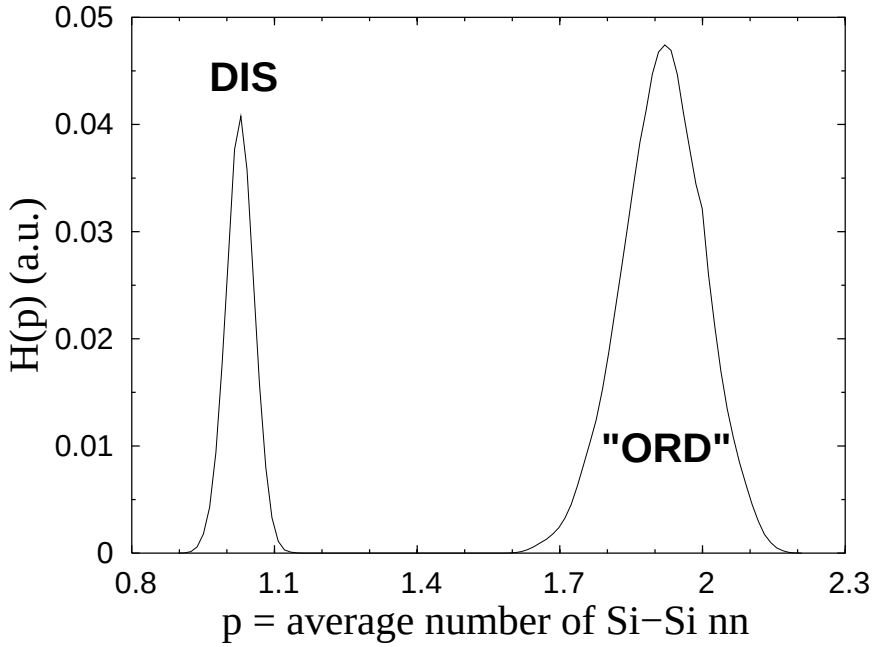

Figure 7.6: Histogram for $p = \langle nn \rangle_{Si-Si}$ at ($\Delta\mu$,T)=(0.472 eV, 0.003612 eV) for a L=10 system. The peak for the disordered phase is located around 1, while the expected value of p for a completely disordered system with the same Si concentration (c_{Si}=0.17) is 0.68.

much slower and smoother event than their destruction when a very limited amount of Si is available.

A more quantitative study of the ordering process is obtained from the analysis of the average number of Si-Si nn, p (p=$\langle nn \rangle_{Si-Si}$). This quantity is equal to four times the Si concentration (1-x) in a completely random mixture, while assumes higher values if order of some kind is present in the system. When computing it for configurations along the branches of hysteresis loops in both high and low c_{Ge} regimes, we discovered that short-range order is present even in the disordered phase (Figure 7.6). This is very reasonable given the inter-atomic potential used and the low temperatures involved in the calculations. More importantly, the significant numer-

ical difference between p in the "ordered" and in the disordered phase indicates that the range of ($\Delta\mu$,T) still is far from the prospective ending of the first order lines, even if both Δc and ΔE (energy difference between the two branches at fixed (μ,T)) appeared to be very small (Figure 7.6). This apparent contradiction is easily explained in terms of finite-size effects: appreciable differences in energy and concentration between branches would be found if large enough systems are used for the simulations.

7.3 High temperature results and phase diagram

To investigate the possible ending of the first order lines, simulations were run for values of $\Delta\mu$ between 0.41 and 0.473 eV. The study of this part of the phase diagram was particularly difficult mainly because of the extremely long times required to form the Si planes at temperatures near the transition: simulations of the order of 10^7 MCs are necessary just to see those planes appear. A usually efficient way to determine the exact location of a first order transition is to use histogram reweighting. Unfortunately, its straightforward application was unfeasible here because it was impossible to obtain good sampling of both phases in a single run. Such a sampling would in fact require forming and destroying the Si planes several times during each run.

Forming the planes was found to be a slower process than destroying them. The most efficient way to determine the phase diagram was, therefore, to start from "ordered" configurations and let them evolve at different temperatures until a temperature high enough to destroy the planes was identified. This procedure had to be repeated for each $\Delta\mu$ that we wanted to investigate. Runs at temperatures close to the transition were usually about $3\times\ 10^6$ MCs long and L=12 systems were used. In a few cases more involved calculations were performed, to allow for finite-size effects analysis.

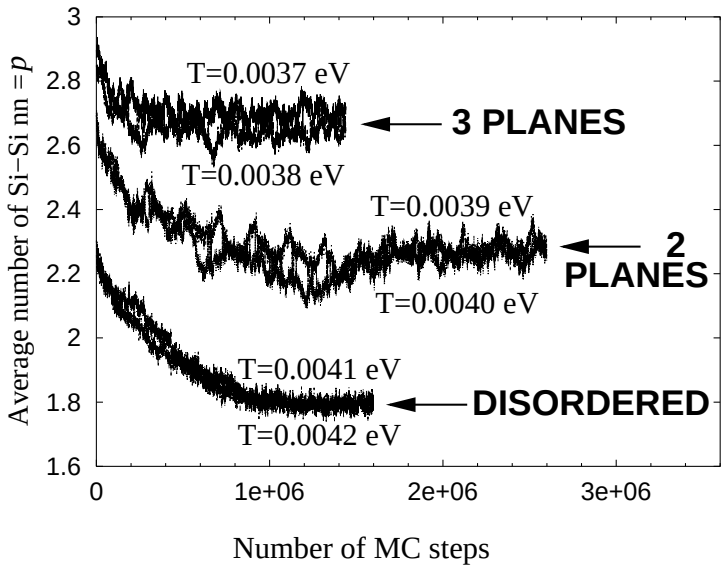

Figure 7.7: Instantaneous values of p at different temperatures and $\Delta\mu$=0.450 eV for a L=12 system (c_{Ge}=0.63). The number of Si planes present in the configuration is displayed next to each curve.

When disordering configurations with more than one Si plane, we observed that the planes disappeared one at a time as T was increased. As an example, instantaneous values of p are shown in Figure 7.7 for different temperatures at $\Delta\mu$=0.450 eV; the corresponding number of stable Si planes is indicated next to each curve. It is not clear at the moment if configurations with less than the maximum number of planes allowed by the amount of Si present correspond to the equilibrium states at that ($\Delta\mu$,T) or to very long lived metastable states. We determined the transition temperature averaging the highest T for which at least one Si plane is stable with the lowest one for which the configuration is disordered.

In Figure 7.8 the resulting phase diagram is shown in both ($\Delta\mu$,T) and (c_{Ge},T) space. As anticipated, a closed first order line is found, instead of two first order lines predicted by Dünweg [74]. The phase diagram is strongly asymmetric towards

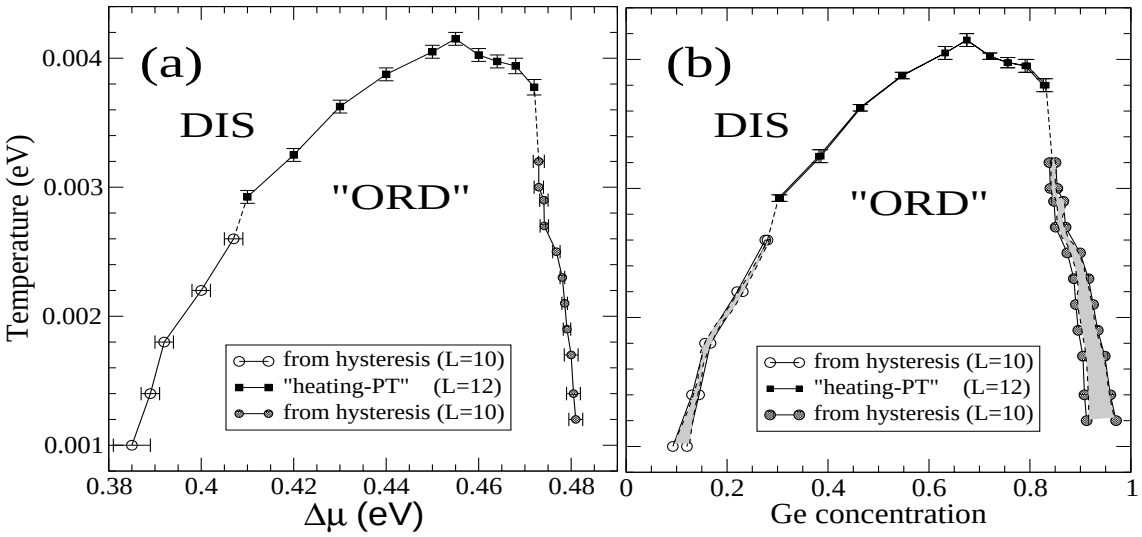

Figure 7.8: Phase diagram in the ($\Delta\mu$-T) (a) and in the (c_{Ge},T) (b) plane. The lines connecting the points are merely guides to the eye. The shaded areas correspond to coexistence regions. Coexistence is not seen at high T because of resolution problems.

the Ge-rich region, which is explained by the particular choice of the volume, as seen in Section 4.2.1. Such an interpretation is further confirmed by the fact that the maximum transition temperature is reached for c_{Ge} near 75%.

To perform finite size analyses, quantities like transition temperature or specific heat maximum need to be accurately determined for several lattice sizes. Combining reweighting (see Section 7.3) with parallel tempering, we were able to obtain good sampling of both phases across the transition line, so that precise evaluation of the maximum of the specific heat, of the susceptibility and of the complete fourth order cumulant were possible. In particular, we avoided the problems related to the use of reweighting discussed in Section 7.3 because PT made it possible to go from one phase to the other without having to wait the excessively long times necessary to form or destroy the Si planes. The only disadvantage of these calculations is their computational cost: fixed $\Delta\mu$, firstly a rough determination of T_t is necessary, done as

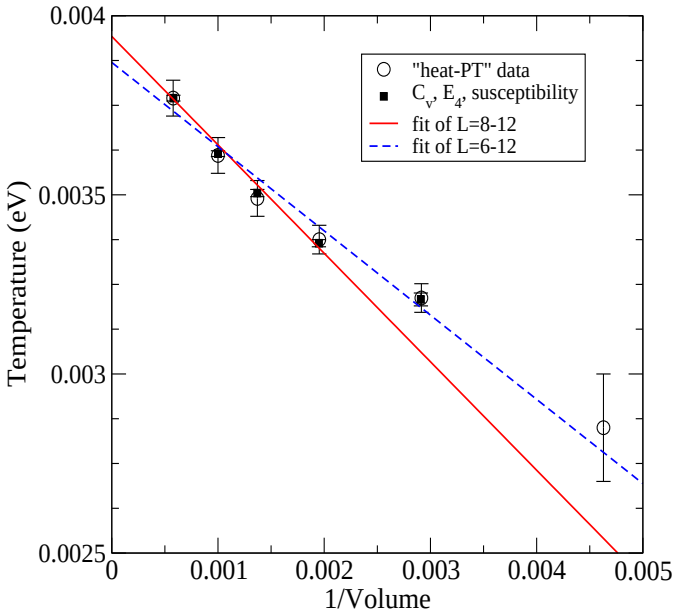

Figure 7.9: Evaluation of the transition temperature for infinite lattice at $\Delta\mu$=0.472 eV. The temperature are plotted versus "1/Volume", where Volume=$N_x N_y N_z$ ($N_{x(y,z)}$=Number of cells along x (y, z)).

described in Section 7.3, then PT calculations are run for several temperatures close to that value. The number of temperatures to investigate depends on the system size because the width of the histograms decreases as the system size increases. When good histograms were constructed, reweighting was performed and the desired quantities calculated.

Scaling results for T_c at $\Delta\mu$=0.472 eV are shown in Figure 7.9. As expected for a first order transition, asymptotically T_c(L) scales linearly with the inverse of the volume. The transition temperature for infinite lattice is therefore estimated to be 0.00394 eV $\pm$ 0.00005, 4.5% greater than the one obtained for a L=12 lattice. Similar results are found for other points in the phase diagram, allowing us to conclude that a good estimate of the infinite lattice phase diagram can be obtained from the one shown in Figure 7.8 increasing the evaluated T by 4.5% or 9.1%, depending on how

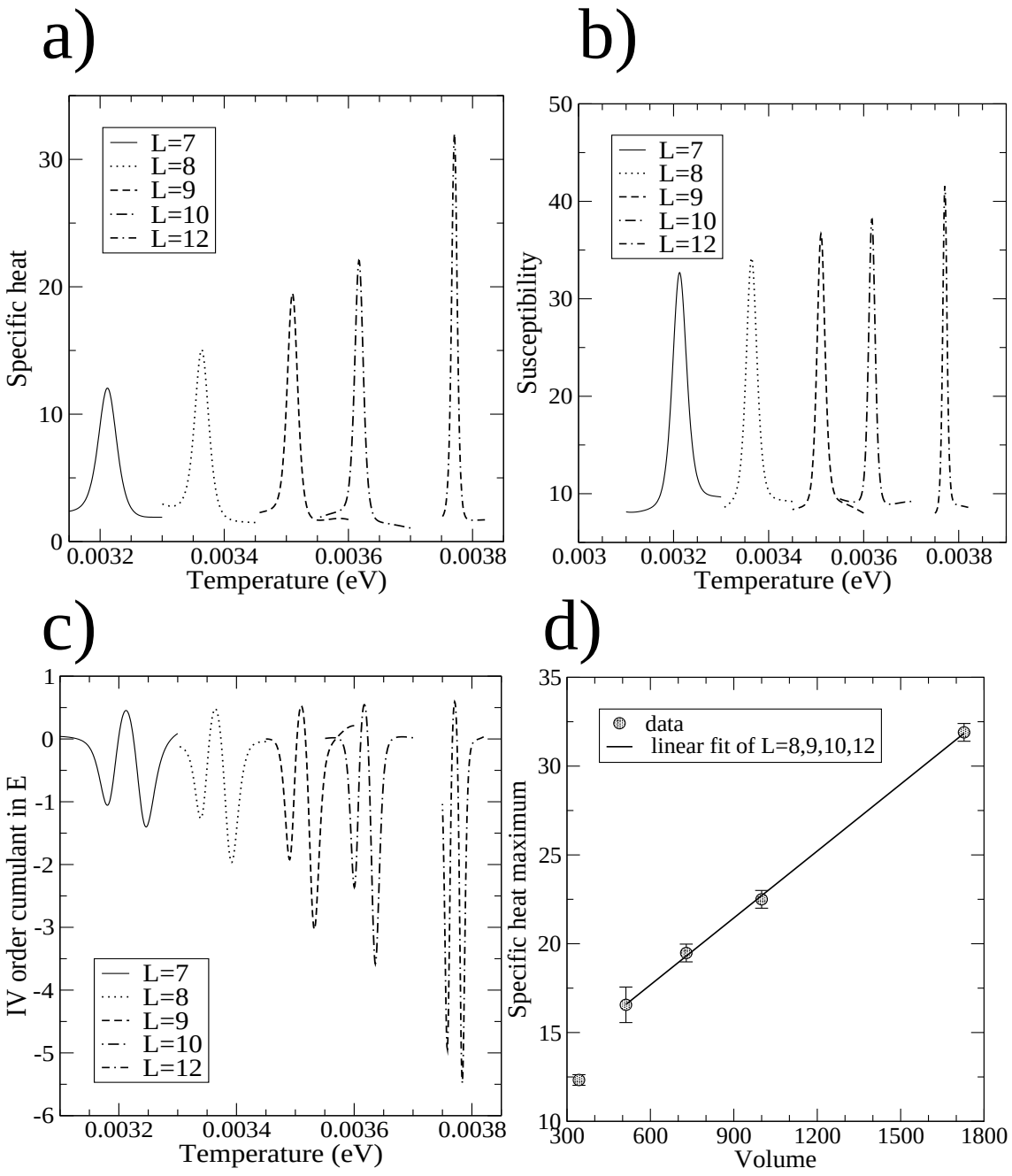

Figure 7.10: Specific heat (a), susceptibility (b) and IV order cumulant in energy (c) for different system sizes at $\Delta\mu$=0.472 eV. Lastly, scaling of the maximum of the specific heat with volume (d), where Volume=$N_x N_y N_z$ ($N_{x(y,z)}$=Number of cells along x (y, z)).

big a system was used to calculate them (L=12 or L=10, respectively). In Figure 7.10 the dependence of specific heat, susceptibility, fourth order cumulant in energy and specific heat maximum on the system sizes is presented. All the data are taken at $\Delta\mu$=0.472 eV. Again our findings are in excellent agreement with what is expected for a first order transition: the linear fit of the specific heat maximum versus volume produces a correlation coefficient r of 0.9997.

7.4 Structural properties

The last problem still to address in this study is the understanding of the formation of the Si planes. A structure where one atomic species forms several planes inside the other doesn't minimize the interface energy; it is therefore not immediately obvious why such a configuration constitutes the ground state (GS) for our system.

To check if the structure we find corresponds to the GS we ran several simulations starting from "phase-segregated" configurations that could be energetically more convenient. In some of those all the Si was contained in a sphere at the center of the cubic simulation cell, while in others (referred to as "SLAB" in the following) it formed one single plane even if at that point in the ($\Delta\mu$,T) space ((0.440 eV, 0.0029 eV)) we had observed the formation of three planes, each one perpendicular to the other two. During these simulations a long equilibration was performed at first, during which the possibility of changing the atomic species was eliminated in order to maintain the desired geometry. Later, such a possibility was reintroduced and the configuration was allowed to evolve freely. As a result, in both geometries the system disordered at first, then reordered forming three, perpendicular, Si planes.

To understand the advantages connected with the formation of the Si planes we compared structural properties computed for "ordered" (ORD), disordered (DIS) and SLAB trial configurations. Such a comparison was repeated for several values of

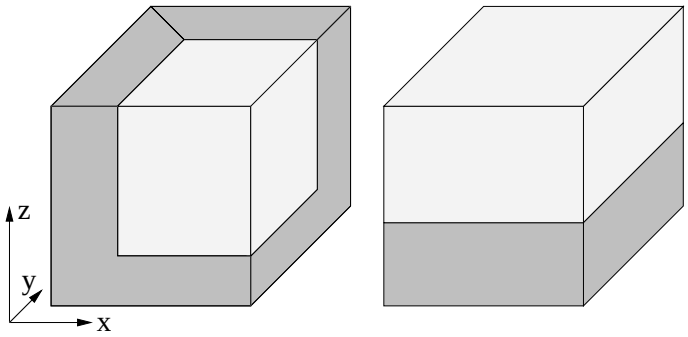

Figure 7.11: Schematic depiction of the "ordered" (a) and "SLAB" (b) configurations for $\Delta\mu$=0.440 eV. The gray areas contain mostly Si, the white ones mostly Ge

$\Delta\mu$, i.e. at different c_{Ge}. In most cases slightly different temperatures had to be used to generate the "ordered" and the disordered configurations because it was impossible to obtain sufficiently disordered states using the same ($\Delta\mu$,T) for which a clear phase-separation was seen. The comparison is nevertheless completely meaningful because structural properties mostly depend on the relative concentration of Si and Ge, which is dictated by $\Delta\mu$ much more than by T. When calculating structural quantities for the "ordered" phase we averaged the areas where the Si planes are (gray areas in Figure 7.11) separately from those that contain mostly Ge (white area in Figure 7.11). This is indicated in Figures 7.12 and 7.13 by the label "in" for quantities evaluated inside the Si planes, and "out" for those evaluated outside such planes.

Because in a random mixture the mean concentration of Si and Ge is uniform, the disordered phase corresponds to the minimal variation of the structural properties with respect to their values in the pure phases. This means that any congregation of atoms of the same species, which is, on the other hand, favored by the interatomic potential, corresponds to a further increase in such a variation. The balance between the energy cost of deviating from the ideal lattice structure and the energy cost of

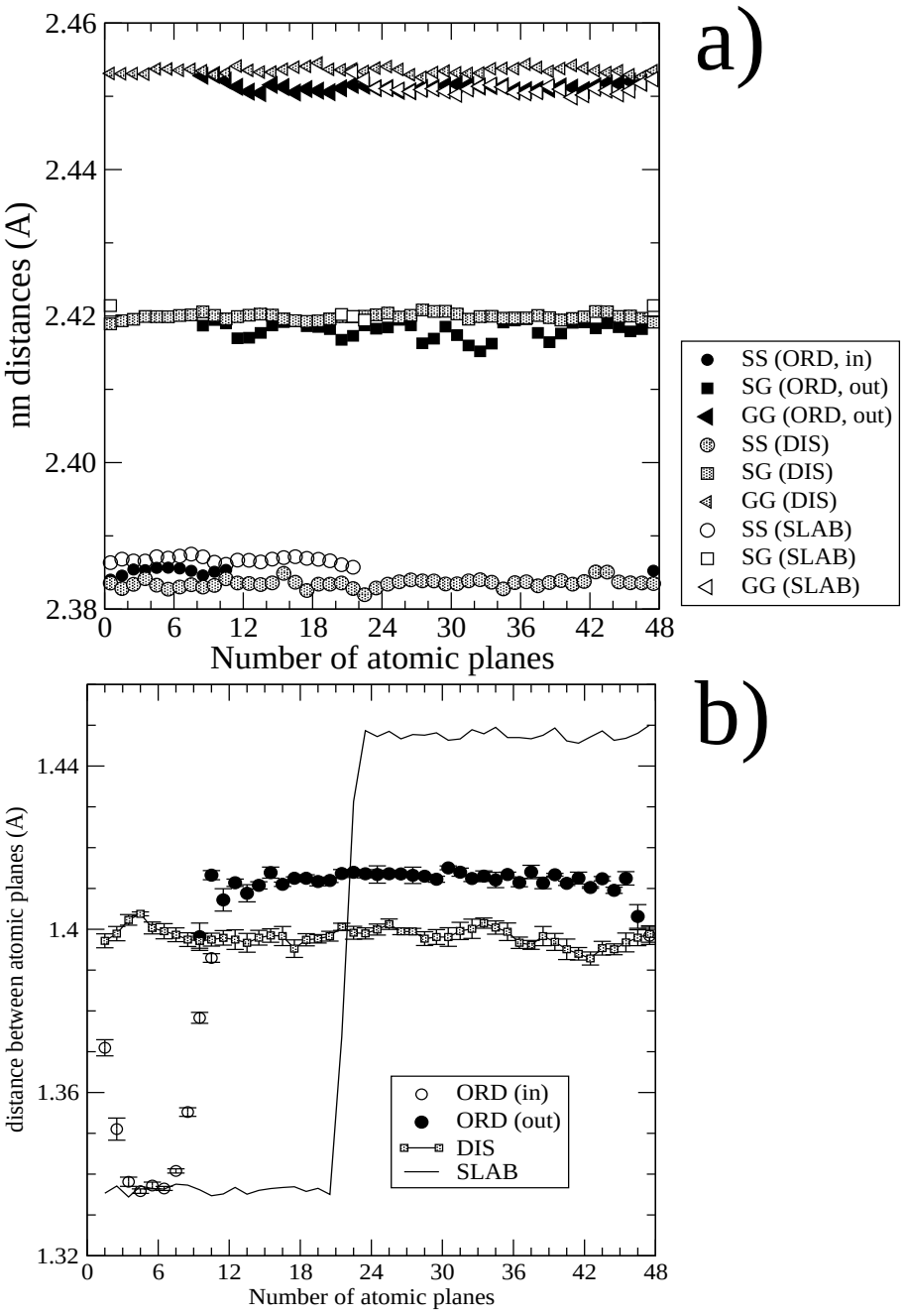

Figure 7.12: nn distances (a) and distance between atomic planes (b) for "ordered", disordered and SLAB configurations at $\Delta\mu$=0.440 eV, T_{ORD}=T_{SLAB}=0.0029 eV, and T_{DIS}=0.0036 eV. For SLAB the atomic planes versus which the structural functions are plotted are perpendicular to the Si slab (z direction in Figure 7.11).

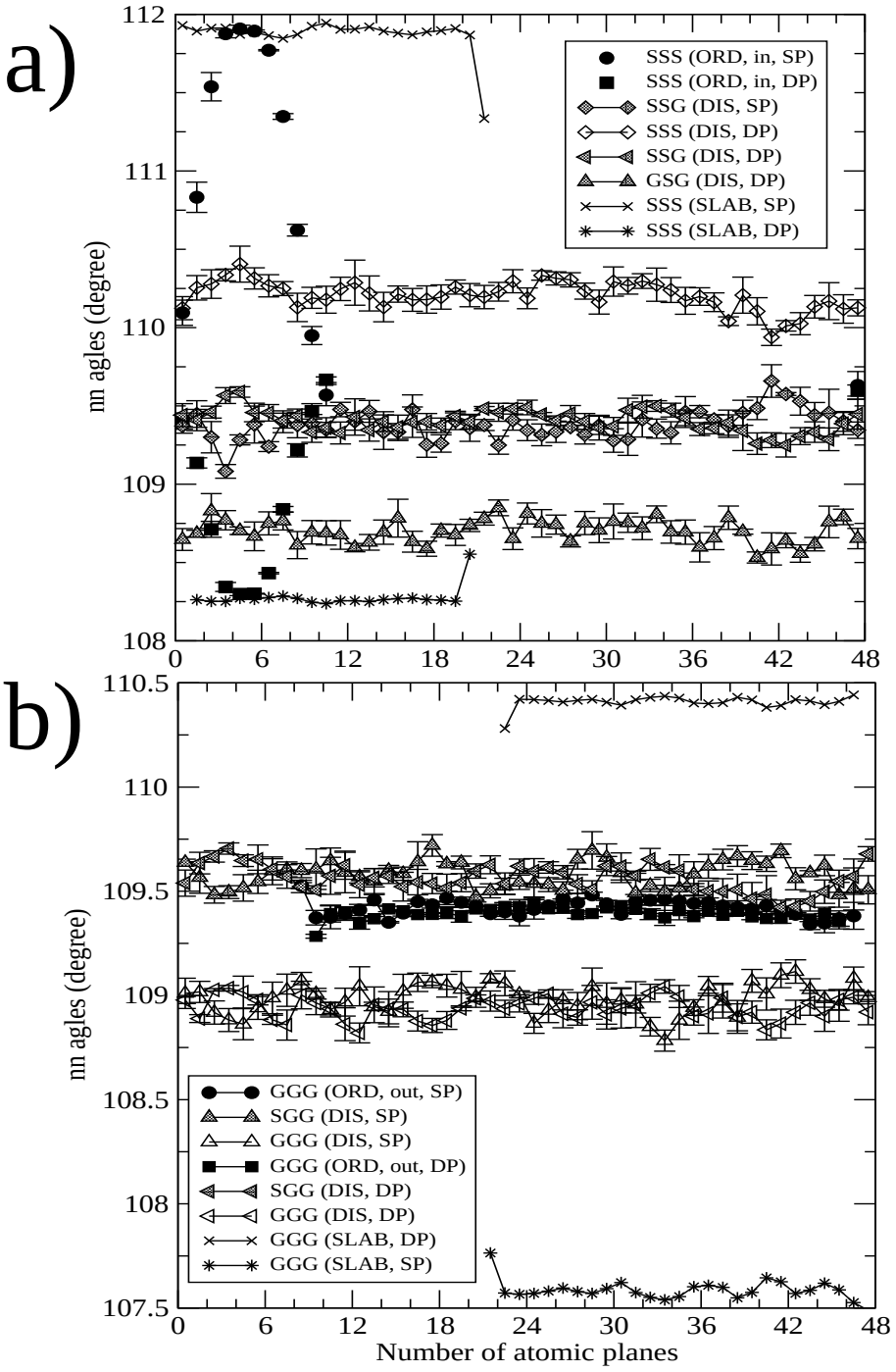

Figure 7.13: nn angles centered on Si (a) and on Ge (b) for "ordered", disordered and SLAB configurations at $\Delta\mu$=0.440 eV, T_{ORD}=T_{SLAB}=0.0029 eV, and T_{DIS}=0.0036 eV. For SLAB the atomic planes versus which the structural functions are plotted are perpendicular to the Si slab (z direction in Figure 7.11). Only angles appearing more than 100 times per plane are shown. SP(DP) indicates that the nn of the atom at the vertex of the angle lie on the same (on different) atomic plane(s).

having mixed (Si-Ge) interaction is the key to understand the formation of the Si planes.

For all the analyzed values of ($\Delta\mu$,T) the nn distances (Si-Si, Si-Ge and Ge-Ge) didn't significantly depend on the configuration structure, i.e. the values found for the "ordered", disordered and "slab" configurations were very similar (Figure 7.12a). On the contrary, the reason behind the formation of the Si planes is found when studying nn angles and inter- plane distances. As shown in Figure 7.12b), the energetically most convenient way to fill the given volume in the part of the system where only Si are present is to move the Si-filled atomic planes closer together by changing nn angles (open circles in Figure 7.12b)), instead of further stretching the Si-Si bonds. This way of avoiding excessive stretching of the Si-Si bonds is possible because in the diamond lattice each atom has two nn lying on one atomic plane and other two lying on a different one. To make this effect even clearer we plotted the nn angles distinguishing those where the nn of the vertex atom lie on the same atomic plane (label "SP") from those where the nn lie on different planes (label "DP"). Obviously, a diminished distance between atomic planes must corresponds to increased SP angles and decreased DP ones with respect to their values in a perfect tetrahedron (θ=109.47) if the bond length is left unchanged. This effect is clearly visible in Figure 7.13 a) (nn angles centered on Si atoms) for all the angles in the "ordered" (solid circles and squares) and in the SLAB (stars and crosses) phase. Moreover, in the "ordered" phase the angles at the center of the Si planes (atomic planes 4-7, Figure 7.13 a)) become very similar to the angles in the SLAB configuration. For obvious geometrical reasons the remaining planes in the system, which are mainly filled with Ge, must move away from each other to balance those that had come too close. In Figure 7.13 b) angles centered on Ge are shown, and it is easy to see how, in this case, angles in the "ordered" phase (solid circles and squares) assume values very close to the ideal one while those in the SLAB configuration (stars

and crosses) are significantly away from it. This difference in behavior justifies the formation of several Si planes for high enough Si concentration, instead of just a thick one. It indeed shows that the lattice distortion needed to balance the excessive compression present in the part of the system filled with Si becomes too large to be convenient when the thickness of the Si slab exceeds a threshold value (about 12 atomic planes in our system).

Chapter 8

Conclusions

In this dissertation we focused on two related problems at the interface between materials science and statistical mechanics: the study of the (001) surface of Si or Ge, and the study of the compressible Ising model with ferromagnetic interactions under constant volume conditions. These problems might appear to be significantly different from each other, but are united by the fact that, in both, elastic interactions play a dominant role in determining the evolution of the system. In our study the elastic interactions are described by classical potentials (Stillinger-Weber and Tersoff), and we performed substantial simulations using importance sampling Monte Carlo algorithms.

When studying the compressible Ising model we adopted the same binary alloy picture (bulk $Si_{1-x}Ge_x$) extensively utilized in the literature to investigate the same model under constant pressure. We did that in order to facilitate comparisons between the two cases. No previous results are available for comparisons in the the constant volume case, but theoretical predictions suggest that two first order lines should appear in the field-temperature plane, ending in critical points. Large jumps in the species concentrations are expected in the concentration-temperature plane, corresponding to the crossing of such first order lines. From our study very different and surprising results appeared. In the field-temperature plane the phase diagram contains a single, closed first order line, instead of the expected two lines, which divides a "phase-segregated" ("ordered") phase from a disordered one. In

the "ordered" phase the most unfavorable species (Si in our case, because of the volume chosen) congregates forming planes in-between which the other species is located. The number of these planes depends on the amount of Si available, while their maximum thickness is a constant. In the concentration-temperature plane we could identify coexistence regions in concentration only at low temperatures, and the corresponding jumps in Si or Ge concentration are much smaller than expected. The first order transition that we find is therefore very weak, much weaker than predicted and also much weaker than seen under constant pressure conditions. The formation or disintegration of the "ordered" phase was found to happen over a time scale of more than 10^6 Monte Carlo steps (MCs). This, together with the occurrence of very long lived metastable states, made the treatment of this system extremely difficult. As a consequence, significant error bars are given in our final estimate of some of the physical quantities, fact that, though, does not impede a complete qualitative characterization of the system behavior. Given how surprising these findings are, it comes natural to wonder how well theoretical predictions for anti-ferromagnetic interactions under constant volume will actually agree with simulational findings. Also, a natural development of this study is to determine what happens, for ferromagnetic interactions and constant volume, if a different choice of V is made. Will all the effects that we observed still remain qualitatively the same, or the two predicted first order lines make their apparence?

When investigating the evolution of Si(001) surface, we utilized standard MC simulations at first, but with highly disappointing results. An excessive number of defects (undimerized atoms) was found when trying to reproduce the (2x1) surface reconstruction, and very little diffusion was attained for adatoms on the surface. We, therefore, decided to develop a new Monte Carlo algorithm, based on the idea of adding the possibility of collective moves to the standard MC moves. We preferred developing a new algorithm instead of simply using Molecular Dynamics (MD),

Kinetic Monte Carlo or standard MC with a solid-on-solid model because we felt that each of these methods was simply ill-suited for the study we were interested in: MD only covers a short time span, while phenomena like step edge evolution and island disintegration occur on a time scale of a few seconds; Kinetic Monte Carlo requires the pre-knowledge of the possible diffusion mechanisms and simulation results are strongly dependent on how well a large number of parameters are fitted; the use of a solid-on-solid model forces discretization on the system, so that restrictions to the atomic motion are introduced. In contrast, the algorithm presented in this dissertation is off-lattice, utilize bulk-fitted potentials and covers a long-time scale. Because it has been implemented using MPI parallelization, it is also well suited for large-scale simulations. The particular version presented in this dissertation is targeted to the study of the Si(001) surface with Si or Ge adatoms, but the idea behind it is rather general and can be easily expanded to the study of other alloy surfaces. The basic idea of this algorithm is the addition of collective moves to the standard MC *single-atom* moves. With MC the evolution of the system is definitely faster than it would be using standard Molecular Dynamics; moreover, because of the collective moves, it is possible to overcome high potential barriers that otherwise would trap the system in metastable states. The identification of the collective moves to implement is the only point where some knowledge of the particular physical system under consideration is necessary. As an example, in the case of the Si(001) surface, the existence of a (2x1) reconstruction leads us to introduce the possibility of moving each dimer as a whole. We tested such an algorithm applying it to the study of dimerization, step edge evolution and island stability on the Si(001) surface. All the qualitative features attained as a result of our simulations are in good agreement with experimental results. Quantitative estimates of physical quantities can also also be obtained using this method, and a few such results are discussed as well. In these cases, too, a good agreement with experimental findings is attained. We conclude

that this method will be of great value for other simulational studies of surface behavior.

Bibliography

[1] F.H. Stillinger and T.A. Weber, Phys. Rev. B **31**, 5262 (1985).

[2] M. Lannoo and P. Friedell, *Atomic and electronic structure of surfaces* (Springer-Verlag, 1991).

[3] R.A. Wolkow, Phys. Rev. Lett. **74**, 4448 (1995).

[4] T. Yokoyama and K. Taskayanagi, Phys. Rev. B **61**, R5078 (2000).

[5] K. Hata, S. Yasuda and H. Shigekawa, Phys. Rev. B **60**, 8164 (1999).

[6] X.R. Qin and M.G. Lagally, Phys. Rev. B **59**, 7293 (1999).

[7] R. Gunnella, E.L. Bullock, L. Patthey, C.R. Natoli, T. Abukawa, S. Kono and L.S.O. Johansson, Phys. Rev. B **57**, 14739 (1998).

[8] H. Over, J. Wasserfall, W. Ranke, C. Ambiatello, R. Sawitzki, D. Wolf and W. Moritz, Phys. Rev. B **55**, 4731 (1997).

[9] H. Shigekawa, K. Hata, K. Miyake, M. Ishida and S. Ozawa, Phys. Rev. B **55**, 15448 (1997).

[10] S.C.A. Gay and G.P. Srivastava, Phys. Rev. B **60**, 1488 (1999).

[11] E. Kim, C. Chen, T. Pang and Y.H. Lee, Phys. Rev. B **60**, 8680 (1999).

[12] W. Stigler, P. Pavone and J. Fritsch, Phys. Rev. B **58**, 13686 (1998).

[13] P. Krüger and J. Pollmann, Phys. Rev. Lett. **74**, 1155 (1995).

[14] A. Ramstad, G. Brocks and P.J. Kelly, Phys. Rev. B **51**, 14504 (1995).

[15] J.E. Northup, Phys. Rev. B **47**, 10032 (1993).

[16] R.A. Wolkow, Phys. Rev. Lett. **68**, 2636 (1992).

[17] S. Katircioglu, S. Salman and S. Erkoc, Int. J. Mod. Phys. C **11**, 999 (2000).

[18] J.D. Chadi, Phys. Rev. Lett. **59**, 1691 (1987).

[19] Y.W. Mo, B.S. Swartzentruber, R. Kariotis, M.B. Webb and M.G. Lagally, Phys. Rev. Lett. **63**, 2393 (1989).

[20] T. Kawamura, T. Sakamoto and K. Ohta, Surf. Sci. **171**, L415 (1986).

[21] A. Rockett, Proc. SPIE Int. Soc. Opt. Eng. **944**, 63 (1988).

[22] J.Y. Tsao, E. Chason, U.K. Köhler and R.J. Hamers, Phys. Rev. B **40**, 11951 (1989).

[23] Y.W. Mo, J. Kleiner, M. Webb and M.G. Lagally, Surf. Sci. **268**, 275 (1992).

[24] Z. Zang, Y.-T. Lu and H. Metiu, Surf. Sci. Lett. **248**, L250 (1991).

[25] G. Brocks, P. Kelly and R. Car, Phys. Rev. Lett. **66**, 1729 (1991).

[26] D. Srivastsva and B. Garrison, J. Chem. Phys. **95**, 6885 (1991).

[27] T. Miyazaki, H. Hiramoto and M. Okazaki, Jpn. J. Appl. Phys. **29**, L1165 (1990).

[28] B. Voigtländer, T. Weber, P. Šmilauer and D.E. Wolf, Phys. Rev. Lett. **78**, 2164 (1997).

[29] C. Pearson, M. Kruger, R. Curtis, B. Borovsky, X. Shi, and E. Ganz, J. Vac. Sci. Technol. A **13**, 1506 (1995).

[30] F. Liu, F. Wu and M.G. Lagally, Chem. Rev. **97**, 1045 (1997).

[31] C.S. Chang, Y.M. Huang and T. T. Tsong, Phys. Rev. Lett. **77**, 2021 (1996).

[32] N.C. Bartelt and R.M. Tromp, Phys. Rev. B **54**, 11731 (1996).

[33] C. Pearson, B. Borovsky, M. Kruger, R. Curtis and E. Ganz, Phys. Rev. Lett. **74**, 2710 (1995).

[34] K. Kammler, M. Horn von Hoegen, N. Voss, M. Trigides, A. Menzel and E.H. Conrad, Phys. Rev. B **65**, 075312-1 (2002).

[35] N.C. Bartelt, J. L. Goldberg, T.L. Einstein, E.D. Williams, J.C. Heyraud and J.J. Metois, Phys. Rev. B **48**, 15453 (1993).

[36] B.S. Swartzentruber, Y.W. Mo, R. Kariotis, M.G. Lagally and M.B. Webb, Phys. Rev. Lett. **65**, 1913 (1990).

[37] H.P. Bonzel and W.W. Mullins, Surf. Sci. **350**, 285 (1996).

[38] B.S. Swartzentruber ans M. Schact, Surf. Sci. **322**, 83 (1995).

[39] N. Kitamura, B.S. Swartzentruber, M.G. Lagally and M.B. Webb, Phys. Rev. B **48**, 5704 (1993).

[40] B.S. Swartzentruber, N. Kitamura, R. Kariotis, M.G. Lagally and M.B. Webb, Phys. Rev. B **47**, 13432 (1993).

[41] N.C. Bartelt, R.M. Tromp, and E.D. Williams, Phys. Rev. Lett. **73**, 1656 (1994).

[42] N.C. Bartelt, W. Theis and R.M. Tromp, Phys. Rev. B **54**, 11741 (1996).

[43] H.J.W. Zandvliet, H.B. Elswijk, E.J. van Loenen, and D.Dijkkamp, Phys. Rev. B **45**, 5965 (1992).

[44] T.W. Poon, S. Yip, P.S. Ho, and F.F. Abraham, Phys. Rev. Lett. **65**, 2161 (1990).

[45] C. Pearson, M. Kruger and E. Ganz, , Phys. Rev. Lett. **76**, 2306 (1996).

[46] J.H. Owen, K. Miki, D.R. Bowler, C.M. Goringe, I. Goldfarb and G.A.D. Briggs, Surf. Sci. **394**, 79 (1997).

[47] H. Metiu, Y.-T. Lu and Z. Zang, Science **255**, 1088 (1992).

[48] A. Rockett, Surf. Sci. **312**, 201 (1994).

[49] J. Tersoff, A.W. Denier van der Gon, and R. M. Tromp, Phys. Rev. Lett. **72**, 266 (1994);

[50] W. Theis and R.M. Tromp, Phys. Rev. Lett. **76**,2770 (1996).

[51] A. Ichimiya, Y. Tanaka and K. Hayashi, Surf. Sci. **386**, 182 (1997).

[52] P.E. Flewitt, R.K. Wild, *Physical Methods for Materials Characterization*, Institute of Physics Publishing, 1994).

[53] R.J. Hamers, P. Avouris, and F. Bozso, *59*, 2071 (1987).

[54] *Scanning Tunneling Microscopy*, edited by J.A. Stroscio and W.J. Kaiser (Academic, New York, 1993).

[55] J.A. Kubby and J.J. Boland, Surf. Sci. Rep. **26**, 61 (1996).

[56] A.F.S. Moreira, W. Figueiredo and V.B. Henriques, Phys. Rev. B **66**, 224425 (2002).

[57] L. Radzihovsky, Phys. Rev. Lett. **87**, 236802, (2001).

[58] J.J. Arenzon, F. Ricci-Tersenghi and D.A. Stariolo, Phys. Rev. E **62**, 5978 (2000).

[59] L. Gu, B.Chakraborty, P.L. Garrido, M. Phani and L. Lebowitz, Phys. Rev. B **53**, 11985 (1996).

[60] G. Papantopoulos, G. Papavassiliou, F. Milia, V.H. Schmidt, J.E. Drumheller, N.J. Pinto, R. Blinc and B. Zalar, Phys. Rev. Lett. **73**, 276 (1994).

[61] A.F.S. Moreira and W. Figueiredo, Phys. Rev. B **46**, 2891 (1992).

[62] W. Schranz, H. Warhanek, R. Blinc and B. Žekš, Phys. Rev. B **40**, 7141 (1989).

[63] D.J. Bergman and B.I. Halperin, Phys. Rev. B **13**, 2145 (1976).

[64] B. Dünweg and D.P. Landau, Phys. Rev. B **48**, 14182, (1993).

[65] M. Laradji, D.P. Landau and B. Dünweg, Phys. Rev. B **51**, 4894, (1995).

[66] P.C. Kelires and J. Tersoff, Phys. Rev. Lett. **63**, 1164 (1989).

[67] P.C. Weakliem and E.A. Carter, Phys. Rev. B **45**, 13458 (1992).

[68] P.C. Kelires, Phys. Rev. Lett. **75**, 1114 (1995).

[69] C. Tzoumanekas and P.C. Kelires, Phys. Rev. B **66**, 195209 (2002).

[70] J. Tersoff, Phys. Rev. Lett. **56**, 632 (1986).

[71] P.N. Keating, Phys. Rev. **145**, 637 (1966).

[72] M.E. Fisher, Phys. Rev. **176**, 257 (1968).

[73] S. de Gironcoli, P. Giannozzi and S. Baroni, Phys. Rev. Lett. **66**, 2116 (1991).

[74] B. Dünweg, *Computersimulationen zu Phasenübergängen und kritischen Phänomenen*, Habilitationsschrift, Mainz, April 2000.

[75] J. Tersoff, Phys. Rev. B **39**, 5566 (1989).

[76] L. Nurminen, F. Tavazza, D.P. Landau, A. Kuronen and K. Kaski, Phys. Rev. B **67**, 35405 (2003).

[77] N. Metropolis, A.W. Rosenbluth, M.N. Rosenbluth, A.H. Teller, E. Teller, Chem. Phys. **21**, 1087 (1953).

[78] D.P. Landau and K. Binder, *A Guide to Monte Carlo Simulations in Statistical Physics* (Cambridge U. Press, Cambridge, 2000).

[79] A.M. Ferrenberg and R.H. Swendsen, Phys. Rev. Lett. **61**, 2635 (1988).

[80] A.M. Ferrenberg and R.H. Swendsen, Phys. Rev. Lett. **63**, 1195 (1989).

[81] E.P. Münger and M.A. Novotny, Phys. Rev. B **43**, 5773 (1991).

[82] A.M. Ferrenberg and D.P. Landau, Phys. Rev. B **44**, 5081 (1991).

[83] R.H. Swendsen and J.S. Wang, Phys. Rev. Lett. **57**, 2607 (1986).

[84] K. Hukushima and K. Nemoto, Journal Phys. Soc. of Japan **65**, 1604 (1996).

[85] A. Bunker and B. Dünweg, Phys. Rev. E **63**, 16701 (2000).

[86] Y. Iba, International Journal of Modern Physics C **12**, 623 (2001).

[87] L. Nurminen, F. Tavazza, D.P. Landau, A. Kuronen and K. Kaski, *submitted.*

[88] F. Tavazza, L. Nurminen, D.P. Landau, A. Kuronen and K. Kaski, *in preparation.*

[89] K.E. Khor and S. Das Sarma, Phys. Rev. B **39**, 1188 (1989).

[90] T.J. Lenosky, B. Sadigh, E. Alonso, V.V. Bulatov, T. Diaz de la Rubia, J. Kim, A. Voter and J.D. Kress, Modelling Simul. Mater. Sci. Eng. **8**, 825 (2000).

[91] P.J. Ungar, T. Halicioglu and W.A. Tiller, Phys. Rev. B **50**, 7344 (1994).

[92] J. Adler, A. Hashibon and G. Wagner, *Recent Developments in Computer Simulation Studies in Condensed Matter Physics, XIV*, edited by D. Landau, S. P. Lewis and B. Schuttler, Springer, p 160-5 (2002).

[93] D.W. Heermann, *Computer Simulation Methods in Theoretical Physics* (Springer-Verlag, Berlin, 1990).

Appendix A

Step fluctuations: theory

In the following a short review of step fluctuation theory will be presented [32]. This is aimed to help the understanding of experimental figures and results presented in Chapter 2

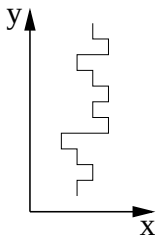

Let *x(y,t)* be the position of the step edge as a function of the distance y along the step edge and the time t. The Fourier component x_q of the step edge is then given by

$$x(y,t) = \sum_q x_q(t) exp(iqy) \tag{A.1}$$

The analysis of the fluctuations in the step edge is done by studying the correlation function G_q(t-t') for each Fourier component x_q:

$$G_q(t-t') =< |x_q(t) - x_q(t')|^2 > \tag{A.2}$$

For wavelengths larger than a few lattice constants, G_q is supposed to have the general form [35]

$$G_q(t) = A(q)[1 - exp(-|t|/\tau(q))] \tag{A.3}$$

For an isolated step, the amplitude A(q) of the fluctuation is a function of the step-edge stiffness β':

$$A(q) = \frac{2kT}{L\beta' q^2} \tag{A.4}$$

where L is the length of the step under analysis.

The step-edge stiffness is a measure of the free-energy cost of bending a step edge, which means that it is related to the energy required to create atomic kinks in the step. In cases where kink excitations can be considered uncorrelated along the step edge, as experimental measurements have shown to be for Si(001) [36], then:

$$\beta' = kTa/b^2 \tag{A.5}$$

where a is the lattice constant, b^2 is the mean-square size of each kink site

$$b^2(T) = \frac{\sum_n a^2 n^2 exp(-E(n)/kT)}{\sum_n exp(-E(n)/kT)} \tag{A.6}$$

and E(n) is the energy of a kink of length na. A commonly accepted way to evaluate E(n) was suggested by Swartzentruber *et al.* [36] in 1990 as a result of their STM measurements of the kink structure. In this model E(n) is related to the kink energy ϵ by the expression

$$E(n) = n\epsilon + C \tag{A.7}$$

and C is the corner energy. Both ϵ and C are obtained from experimental data. Swartzentruber *et al.* estimated C to be 80±20 meV and ϵ to be 90±10 meV for S_A steps and 28±2 meV for S_b steps. Pearson *et al.* [33] C=71 meV and ϵ=32 meV for S_A steps.

The time constant $\tau(q)$ of the step fluctuation (Eq. A.3) increases as the wavelength of the fluctuations increases because large fluctuations require more mass transport to occur. In the most general case, when all three processes are acting simultaneously, $\tau(q)$ can be shown to be [37]

$$\tau(q) = \frac{kT}{\Gamma\beta' q^2}\left(\frac{\Gamma + 2c_0 D^t \omega^2 q + \omega^{3/2} D^s q^2}{2c_0 D^t \omega^2 q + \omega^{3/2} D^s q^2}\right) \tag{A.8}$$

where Γ is the step mobility, D^t the diffusion coefficient for adatoms on terraces, c_0 the equilibrium adatom concentration on the terraces and D^s the diffusion coefficient

for atoms along the step edge. When D^s and D^t are sufficiently large, the attachment and detachment of atoms from the step edge is the rate-limiting process for step motion and Eq. A.8 simply becomes

$$\tau(q) = \frac{kT}{\Gamma \beta' q^2} \tag{A.9}$$

In the limit of Γ very large and D^s small, the rate- limiting process is the diffusion on the terraces and Eq. A.8 becomes

$$\tau(q) = \frac{kT}{2c_0 D^t \omega^2 q^3 \beta'} \tag{A.10}$$

Finally, when Γ is large and D^t small, step fluctuations are limited by diffusion along the step edge and $\tau(q)$ is given by

$$\tau(q) = \frac{kT}{\omega^{3/2} D^s q^4 \beta'} \tag{A.11}$$

Finally, it can be noted that in the particular case of attachment-detachment limited kinetics the step mobility Γ is given by (Eq. A.4 and Eq. A.9):

$$\Gamma = \frac{LA(q)}{2\tau(q)} \tag{A.12}$$

Appendix B

Velocity Verlet algorithm

In the following the Velocity Verlet algorithm is briefly presented. For a more detailed discussion of its merits and limitations we recommand Ref. [93].

(i) Specify the initial positions r_i^1;

(ii) Specify the initial velocities v_i^1;

(iii) Compute the positions at time step n+1 as

$$r_i^{n+1} = r_i^n + hv_i^n + h^2 F_i^n/(2m)$$

where h=time step, m=mass of particle i, and F_i^n= force acting on particle i at time step n;

(iv) Compute the velocities at time step n+1 as

$$v_i^{n+1} = v_i^n + h(F_i^n + F_i^{n+1})/(2m)$$

Appendix C

SW Forces

In the following the analytic expression of the forces derived from the SW potential is presented. The calculation of these forces was performed when using MD to increase the acceptance for the *dimer-jump* move (Section 5.4.3).

As discussed in Chapter 4, the SW potential can be written as the sum of a two-body and a three-body term (Equation 4.1). Because of this, the forces due to the two-body and to the three-body contributions can be derived separately. In the following we indicate the former as $\mathrm{F}^{(2)}$ and the latter as $\mathrm{F}^{(3)}$.

Defining g=$\mathrm{r}_{ij}/\sigma(S_i, S_j)$ and all the other quantities as in Equations 4.2 and 4.4, we have:

$$F^{(2)}_{x_i} = \frac{d\mathcal{H}_2}{dx_i} = \sum_{<i,j>} \varepsilon(S_i, S_j) \frac{dF_2(g)}{dx_i} \tag{C.1}$$

where

$$\begin{aligned} \frac{dF_2(g)}{dx_i} &= xx\ K^2\ h(g) \\ xx &= (x_i - x_j), \quad K = \sigma(S_i, S_j)^{-1} \\ h(g) &= -\frac{Ae^{\delta/(g-b)}}{g}\left(\frac{4B}{g^5} + \frac{(B/g^4 - 1)}{(g-K)^2}\right) \end{aligned}$$

Similarly,

$$\begin{aligned} \frac{dF_2(g)}{dy_i} &= yy\ K^2\ h(g) \\ \frac{dF_2(g)}{dz_i} &= zz\ K^2\ h(g) \\ yy &= (y_i - y_j), \quad zz = (z_i - z_j) \end{aligned}$$

In the case of the three body contribution we have:

$$F_{x_i}^{(3)} = \frac{d\mathcal{H}_3}{dx_i} = \sum_{<i,j,k>} C_{12} \frac{d}{dx_i} \left[F_3(g_1, g_2) * (cos\theta_{i,j,k} + 1/3)^2 \right] = \tag{C.2}$$
$$= \sum_{<i,j,k>} C_{12} \frac{dM(g_1, g_2)}{dx_i}$$

where index 1 refers to the ij atomic pair, index 2 to the ik atomic pair and

$$\begin{aligned}
C_{12} &= [\varepsilon(S_i, S_j) * \varepsilon(S_j, S_k)]^{1/2} * [\lambda(S_i)\lambda(S_j)^2\lambda(S_k)]^{1/4} \\
\frac{dM(g_1, g_2)}{dx_i} &= -\left(\frac{\gamma x x_1}{\sigma_1^2 g_1 (g_1 - b)^2} + \frac{\gamma x x_2}{\sigma_2^2 g_2 (g_2 - b)^2} \right) e^S \, (cos\theta + 1/3)^2 + \\
&\quad 2\, e^S (cos\theta + 1/3) \left[\frac{x x_1 + x x_2}{\sigma_1 \sigma_2 g_1 g_2} - cos\theta \, \left(\frac{x x_1}{\sigma_1^2 g_1^2} + \frac{x x_2}{\sigma_2^2 g_2^2} \right) \right] \\
S &= \frac{\gamma}{g_1 - b} + \frac{\gamma}{g_2 - b} \\
x x_1 &= (x_i - x_j), \quad x x_2 = (x_i - x_k)
\end{aligned}$$

Similar expressions are obtained for $\frac{dM(g_1,g_2)}{dy_i}$ and $\frac{dM(g_1,g_2)}{dz_i}$.